2008

Analysis of water seepage through earthen structures using particulate approach

Kalyani Jeyisanker
University of South Florida

Analysis of Water Seepage Through Earthen Structures Using the Particulate Approach

by

Kalyani Jeyisanker

A dissertation submitted in partial fulfillment
of the requirements for the degree of
Doctor of Philosophy
Department of Civil and Environmental Engineering
College of Engineering
University of South Florida

Major Professor: Manjriker Gunaratne, Ph.D.
Alaa Ashmawy, Ph.D.
Mark Luther, Ph.D.
Gray Mullins, Ph.D.
Muhammad Mustafizur Rahman, Ph.D.

Date of Approval:
November 03, 2008

Keywords: Navier Stokes Equations, Monte-Carlo Simulation, Volumetric Compatibility, Staggered Grid, Critical Localized Condition, Unsaturated, Soil Water Characteristic Curve

DEDICATION

This work is dedicated to my husband, Jeyisanker and my daughter, Harinie. Jeyisanker has been a tremendous support. He was always there in the hard days throughout the research. Without his support and encouragement, I would never achieve this.

ACKNOWLEDGMENTS

I would like to thank my advisor, Dr. Manjriker Gunaratne, for his guidance and support throughout the research. Dr. Gunaratne was always there to suggest ideas and to improve my writing skills, and to expand my academic knowledge in Geotechnical Engineering. Additionally, I would like to extend my thanks to the members of my examining committee Dr. Alaa Ashmawy, Dr. Gray Mullins, Dr. Mark Luther and Dr. Muhammad Mustafizur Rahman for all their support and courage given to me to complete my research. I would like to thank Dr. Nimal Seneviratne for his advice to complete my studies successfully.

My thanks go to my colleagues, Ms. S.Amarasiri, Mr. L.Fuentes, Mr. M.Rajapakse, Mr. J.Kosgolle and Ms. K.Kranthi for their help especially when I am out of office.

TABLE OF CONTENTS

LIST OF TABLES

LIST OF FIGURES

ANALYSIS OF WATER SEEPAGE THROUGH EARTHEN STRUCTURES USING THE PARTICULATE APPROACH

KALYANI JEYISANKER

ABSTRACT

A particulate model is developed to analyze the effects of steady state and transient seepage of water through a randomly-packed coarse-grained soil as an improvement to conventional seepage analysis based on continuum models. In the new model the soil skeleton and pore water are volumetrically coupled. In the first phase of the study, the concept of relative density has been used to define different compaction levels of the soil layers of a *completely saturated* pavement filter system and observe the seepage response to compaction. First, Monte-Carlo simulation is used to randomly pack discrete spherical particles from a specified Particle Size Distribution (PSD) to achieve a desired relative density based on the theoretical minimum and maximum void ratios. Then, a water pressure gradient is applied across one two-layer filter unit to trigger water seepage. The pore water motion is idealized using Navier Stokes (NS) equations which also incorporate drag forces acting between the water and soil particles. The NS equations are discretized using finite differences and applied to discrete elements in a staggered, structured grid. The model predicted hydraulic conductivities are validated using widely used equations. The critical water velocities, hydraulic gradients and flow within the

saturated soil layers are identified under both steady state and transient conditions. Significantly critical transient conditions seem to develop.

In the second phase of the study the model is extended to analyze the confined flow through a *partly saturated* pavement layer and *unconfined flow* from a retention pond into the surrounding saturated granular soil medium. In partly saturated soil, the water porosity changes resulting from water flow is updated using the Soil Water Characteristics Curve (SWCC) of the soil. The results show how complete saturation develops due to water flow following the water porosity Vs pressure trend defined by the SWCC. Finally, the model is used to predict the gradual reduction in the water level of a retention pond and the location of the free-surface. The free-surface is determined by differentiating the wet and dry zones based on the Heaviside step function modified NS equations.

CHAPTER ONE

INTRODUCTION

1.1 Background

Durability of earthen structures such as dams, levees, embankments and pavements is determined by one dominant factor; the nature of interaction of soil particles with water flow. Hence accurate analysis of water seepage through soils is essential to achieve more durable designs of such structures. The majority of currently available design criteria are formulated based on either the analysis of steady state laminar flow through saturated soil continua or empiricism. However, very often, field observations are also used to refine or calibrate the design criteria. In the conventional models, the dynamic flow of water through soil pores is commonly idealized using the Darcy's law. Experimental studies show that Darcy's law could be inaccurate for modeling transient conditions and high fluid velocities that develop under excessive hydraulic gradients [1]. It is also known that, under wind and tidal impacts as well as rainfall and rapid reservoir drawdown, it is the transient and non-laminar flow that plays a more crucial role in determining the stability of earthen and hydraulic infrastructure. In order to evaluate localized critical zones, one has to replace the conventional method of analysis based on a continuum to an alternative approach with a discrete soil skeleton which allows passage of water through its

interstices. Moreover, forensic investigations of failures often remind the civil engineering community of

1) The vital role of the discontinuous or particulate nature of soil
2) The importance of analyzing the flow through unsaturated soils, and
3) The importance of incorporating critical transient effects that generally precede the eventual steady state flow.

1.2 Literature Review

Modeling of seepage through particulate media considering soil-water interaction is relatively new to computational geomechanics. Due to its complexity, Fredlund [2] used Richard's equation (Eqn 1) and the continuum approach to obtain approximate solutions for slope stability problems.

$$k_x \frac{\partial^2 h}{\partial x^2} + k_y \frac{\partial^2 h}{\partial y^2} + \frac{\partial k_x}{\partial x}\frac{\partial h}{\partial x} + \frac{\partial k_y}{\partial y}\frac{\partial h}{\partial y} = m_w^2 \frac{\partial h}{\partial t} \quad (1)$$

Where, h is the total hydraulic head, k_x and k_y are the x and y directional hydraulic conductivities and m_w^2 is the water storage coefficient equal to the slope of Soil-Water Characteristic Curve.

As for non-steady state or transient flow problems, Fredlund [2] used Richard's equation (Eqn 1) and the continuum approach to obtain approximate solutions.

Where, h is the total hydraulic head, k_x and k_y are the x and y directional hydraulic conductivities and m_w^2 is the water storage coefficient equal to the slope of Soil-Water Characteristic Curve [2]. Ng and Shi [3] also used Eqn1 to numerically investigate the

stability of unsaturated soil slopes subjected to transient seepage. In Ng and Shi's [3] work, a finite element model was used to investigate the influence of various rainfall events and initial ground water conditions on transient seepage. However, slope stability was analyzed without considering the localized effects of high pressure build-up and high hydraulic gradients within the slope.

Modeling of seepage through particulate media considering soil-water interaction is relatively new to computational geomechanics. The discrete element method (DEM) provides an effective tool to model granular soils in particular based on micro mechanical idealizations. El Shamy et al. [4] presented a computational micro-mechanical model for coupled analysis of pore water flow and deformation of granular assemblies. El Shamy et al. [4] have used their model and investigated the validity of Darcy's law in terms of particle sizes and porosities. In addition, El Shamy and Zeghal [5] conducted simulations to investigate the three dimensional response of sandy deposits when subjected to critical and over-critical upward pore fluid flow using a coupled hydromechanical model. These simulations provide valuable information on a number of salient microscale mechanisms of granular media liquefaction under quicksand conditions. In addition, Shimizu's [6] particle-fluid coupling scheme with a mixed Lagrangian-Eulerian approach which enables simulation of coupling problems with large Reynolds numbers is implemented in PFC 2D and PFC 3D released by Itasca Consulting Group, Inc. [7]. The models used by El Shamy and Zeghal [5] and Shimizu [6] are both based on the work by Anderson and Jackson [8] and Tsuji et al. [9]. Anderson and Jackson [8] modeled pore fluid motion using averaged Navier Stokes equations. Tsuji et al. [9] simulated the process of particle

mixing of a two-dimensional gas-fluidized bed using averaged Navier Stokes equations for comparison with experiments. For all the above cited studies, granular assemblies are modeled using the discrete element model developed by Cundall and Strack [10] and the averaged Navier Stokes equations are discretized using a finite volume technique on a staggered grid [11].

The discrete nature of soil makes the required constitutive relationships to be exceedingly complex needing a large number of parameters to be evaluated in order to model the soil behavior accurately. However, the state-of-the-art high performance computer facilities would help the designer save time on the computations. Furthermore, nanoscale experimentation can be performed to establish model parameters such as the coefficients of normal and shear stiffness between the grains.

1.3 Objectives

1.3.1 Pavement Filter Design

Design of durable filters is essential for highway pavements since the filters largely determine the success and failure of the drainage system and the lasting separation of pavement layers. Inadequate compaction or segregation of filter layers during placement and excessive cyclic traffic loads can lead to undesired soil particle migration and eventual erosion causing the malfunction of the pavement. Figure 1 shows a typical pavement structure made of three layers; subgrade, subbase and base. The results presented in the paper are only for the subbase-base layer interface (Figure 2a). Similar results can be obtained for the subgrade- subbase layer interface as well (Figure 2b).

Currently, the conventional criteria (Eqn 2) proposed by U.S. Army Corps of Engineers [12] are used for filter design. In these criteria, the filter refers to coarser layer and the finer layer is defined as the soil.

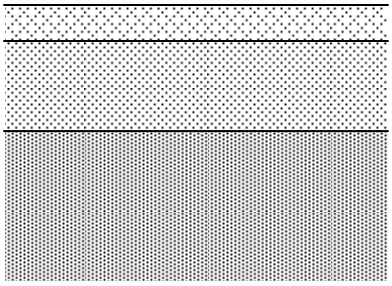

Figure 1: Typical Pavement Structure

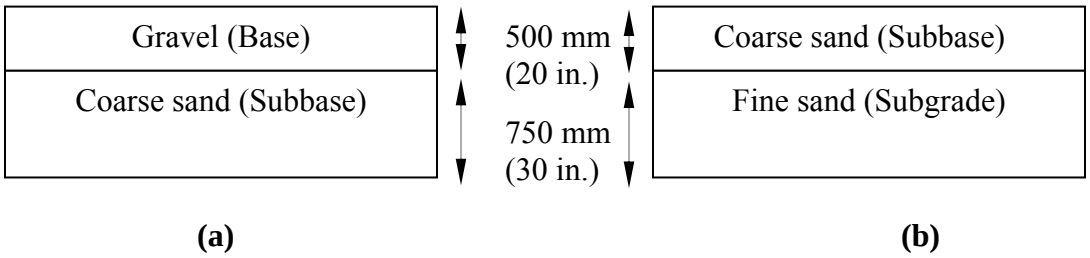

Figure 2: Pavement Layer Interfaces

Clogging criterion:

$$\frac{D_{15}^{filter}}{D_{85}^{soil}} \leq 5 \tag{2a}$$

Permeability criterion:

$$\frac{D_{15}^{filter}}{D_{15}^{soil}} \geq 5 \tag{2b}$$

Additional criterion:

$$\frac{D_{50}^{filter}}{D_{50}^{soil}} < 25 \tag{2c}$$

D_{15}, D_{50} and D_{85} are the diameters of a soil mixture which correspond to cumulative weight percentages of 15%, 50% and 85% respectively in a particle size distribution of the mixture as shown in Figure 8.

While the above criteria generally enable the designer to select the gradation of different structural layers, the flow characteristics and hydraulic gradients within the system are determined using the Darcy's law. An obvious inadequacy of the current drainage design is the use of flow parameters and hydraulic conditions that represent only the overall average and steady-state conditions of each layer. Therefore, the conventional drainage and filter design techniques are unable to incorporate, perhaps more critical, localized, random and transient effects. Hence, the model presented here would equip designers with an analytical tool to address the deficiencies of current design techniques.

1.3.2 Retention Pond Design

Retention ponds are man-made or natural depressions into which stormwater runoff is directed for temporary storage with the expectation of disposal by infiltration into a shallow groundwater aquifer. They are often created near areas of development and in many instances required with new development of buildings, parking lots, roads, etc by the permitting agencies. Retention ponds are developed primarily to serve two functions such as limit flooding and removal of pollutants.

These ponds generally comprise a sedimentation forebay and a larger basin sized to hold the water quality volume (WQV). They retain larger storm volumes for 24 to 48 hours, thus protecting the channels (streams, etc.) that receive the effluent. They also can be

designed to retain larger volumes generated by 10- to 100-year rain events. Water treatment is achieved naturally when particles settle along the flow path between inlet and outlet of the pond, and between storms when additional settling occurs. Nutrient removal occurs between storms via plant uptake. Rain events provide a fresh influx of stormwater runoff, which forces standing water out of the system. Maintenance requirements of retention ponds include the periodic removal of sediment and vegetation to restore storage capacity. Sediment removal is performed primarily in the forebay, which can be designed for easy equipment access.

The model presented in this dissertation first uses a self-developed packing algorithm to randomly pack a three dimensional discrete soil skeleton. Then the model is used to determine the water flow behavior of the particulate soil medium consisting of volumetrically coupled water continuum and the discrete soil skeleton. The flow of water through the particulate medium is modeled using the Navier Stokes (NS) equations which are discretized using the finite difference method (FDM) [13]. The new model is capable of predicting both transient and steady state flow effects. The model is applied to a pavement structure designed based on the U.S. Army Corps of Engineers' filter designed criteria [12] to analyze the localized transient and steady state seepage effects in terms of water velocities and hydraulic gradients at different degrees of compaction. Appropriate boundary conditions have been employed to simulate the conditions resulting from of a sudden surge of ground water just beneath the pavement subbase. It is assumed in the new model that reasonably accurate estimates of the above parameters can be obtained by volumetric coupling of water and the soil skeleton.

1.4 Numerical Modeling

Numerical modeling can be performed to solve geomechanics problems using two different approaches:

1) Solid continuum methods
2) Discrete element methods

1.4.1 Solid Continuum Methods

In the solid continuum approach, the entire soil body is first divided into a number of small elements and the governing equations are mathematically solved for each element. In this regard, the following three methods are widely used:

1) Finite Difference method
2) Finite Element method
3) Finite Volume method

1.4.2 Discrete Element Methods

Discrete element methods (DEM) comprise a suite of numerical techniques developed to model granular materials, rock, and other discontinua at the scale of grains. In most cases, the granular particles modeled as 3D spheres or 2D discs are individually packed in the structure. Then, appropriate inter-particle characteristics such as coefficients of normal and shear stiffness, friction between adjacent particles and friction between particles and other structures are introduced in the analysis. As in the case of continuum methods, the governing equations are solved numerically. Due to the nature of this analysis, DEM are also known as particle modeling methods. Particle Flow Code (PFC) [7] is one of the discrete element methods.

1.5 Assembling of Particles in the Particle Flow Code

Using the PFC program, individual soil particles can be packed to model a given geotechnical structure such as an earthen dam or a pavement layer by closely simulating the transient dynamics of that particulate medium involved with the construction of that structure. The following laws govern the packing (construction) mechanism to achieve the final force equilibrium.

1) Law of motion (Newton's second law)
2) Appropriate force displacement (constitutive) laws for normal and shear deformation

The computational cycle in *PFC-2D* is a time stepping algorithm that consists of the repeated application of the law of motion to each particle, a force-displacement law to each contact, and constant updating of boundaries. The force-displacement law based on the contact constitutive model is repeatedly applied to each contact to update the contact forces based on the relative motion between the two entities at the contact. Until the particles reach equilibrium, the above laws will be applied in a loop as shown in Figure 3.

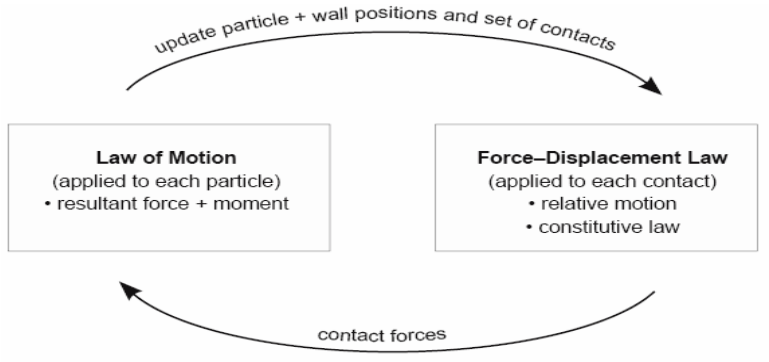

Figure 3: Computational Cycle in PFC

1.5.1 Theoretical Background of PFC

1.5.1.1 Particle Interactions

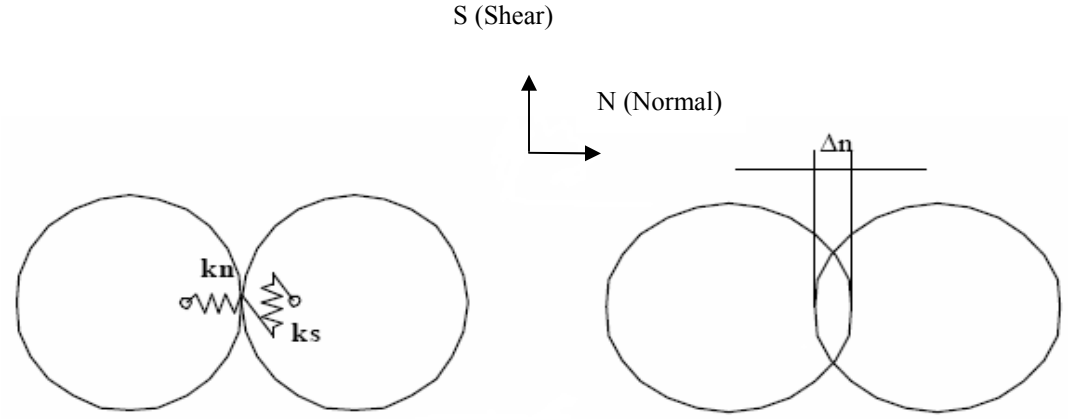

Figure 4: Illustration of Inter-Particle Forces

The above-mentioned rigid circular particles (or spherical in 3-D) interact by way of normal and shear contacts modeled by a simplified mass-spring system as shown in Figure 3. For each pair of particles, the interactive force can be written as

$$F_i = k_n \, \Delta N.N + k_s \, \Delta s.s \tag{3a}$$

Where, k_N - Coefficient of normal stiffness, k_s - Coefficient of shear stiffness, ΔN – Normal deformation and Δs – Shear deformation. Then, the total force acting on a particle given by,

$$F_{total} = \sum F_i \tag{3b}$$

1.6 Organization of Dissertation

Chapter 2 describes the methodology used to randomly pack the soil particles and the mathematical formulation for steady state flow through a particulate pavement system. Chapter 3 presents the modification made on the governing equations for analyzing the transient behavior of water through particulate pavement system using the volumetric compatibility of the two phase media, such as water and solid particles. Chapter 4 describes the mathematical formulation of flow through partly-saturated and saturated soils using Navier Stokes equations. Chapter 5 illustrates the application of the developed models for analyzing flow around retention ponds in order to determine the free-surface (Phreatic surface) using Navier Stokes equations. The different approaches are proposed to determine the free-surface for flow from retention pond. Results are included in each Chapter.

CHAPTER TWO

ANALYSIS OF STEADY STATE WATER SEEPAGE IN A PAVEMENT SYSTEM USING THE PARTICULATE APPROACH

2.1 Preliminary Studies Using Existing Software

The existing finite-element software (Seep/W) and discrete element software (PFC2D) were used at the time of preliminary studies in order to visualize the effects of continuum and discrete approaches on flow problems. A simple model shown in Figure 5 was used to identify the localized effects within a two-layer pavement system. Under same pressure gradient, the flow rates are compared using continuum and discrete methods. Flow rate obtained using discrete method (0.0025 m3/s/m width) is less than that of continuum method (q = 0.0027 m3/s/m width) due to additional drag forces in the particulate matrix.

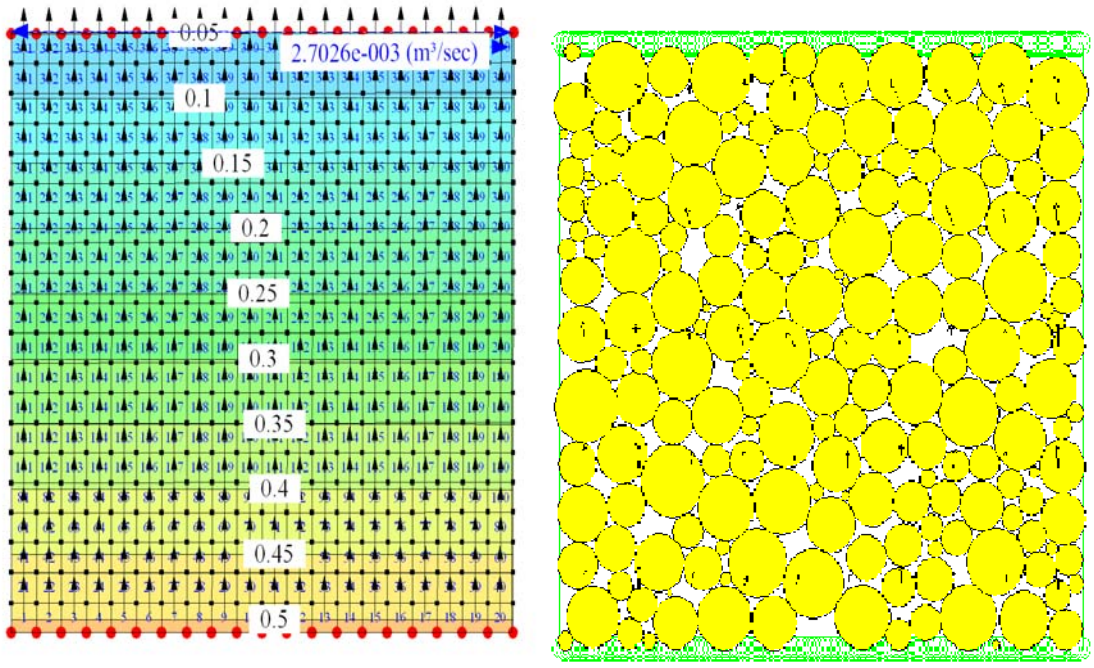

FEM (Seep/W)
(Contours for pressure head are shown)

DEM (PFC 2D)

Figure 5: Analysis of Flow Problem Using Existing Software

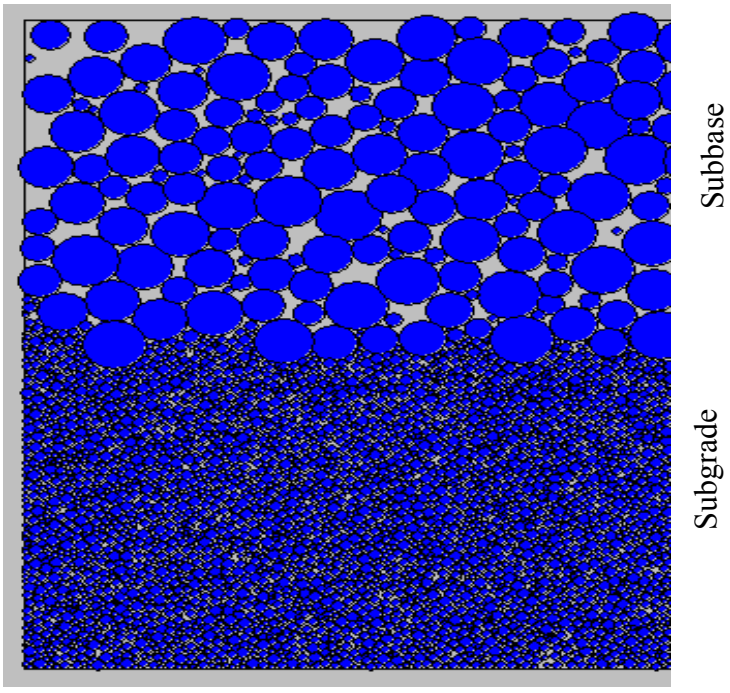

Figure 6a: Highway Pavement Layers

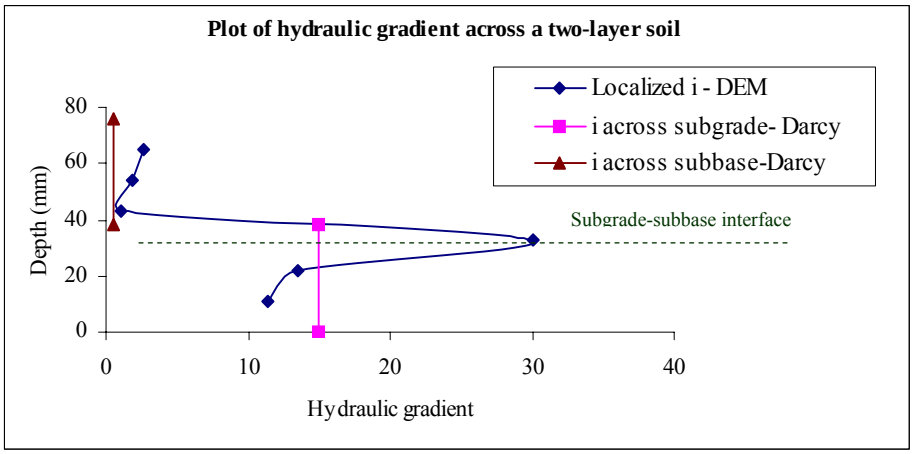

Figure 6b: Comparison of Hydraulic Gradients Obtained Using Continuum and Discrete Methods (Steady State)

The seepage through two-layer pavement shown in Figure 6a was modeled using the PFC2D. As illustrated in Figure 6b, there is a significant difference in hydraulic gradients using the continuum and discrete approaches. At the interface, i_{local} exceeds the $i_{Conventional\ analysis}$. However, since the three-dimensional porosities are realistic, the authors developed a three-dimensional packing algorithm. The results obtained from the preliminary studies motivated the authors for analyzing the seepage phenomena through particulate soil media.

2.2 Methodology Followed to Develop a Novel Algorithm

The comprehensive analytical procedure and the computer code developed for its implementation are illustrated in Figure 7. The analytical procedure consists of two primary tasks such as random assembly of the particulate medium (granular soil) and solution of the fluid flow governing equations using partial coupling between the two

media. The flow chart also includes the sections, equation numbers and figure numbers corresponding to each stage.

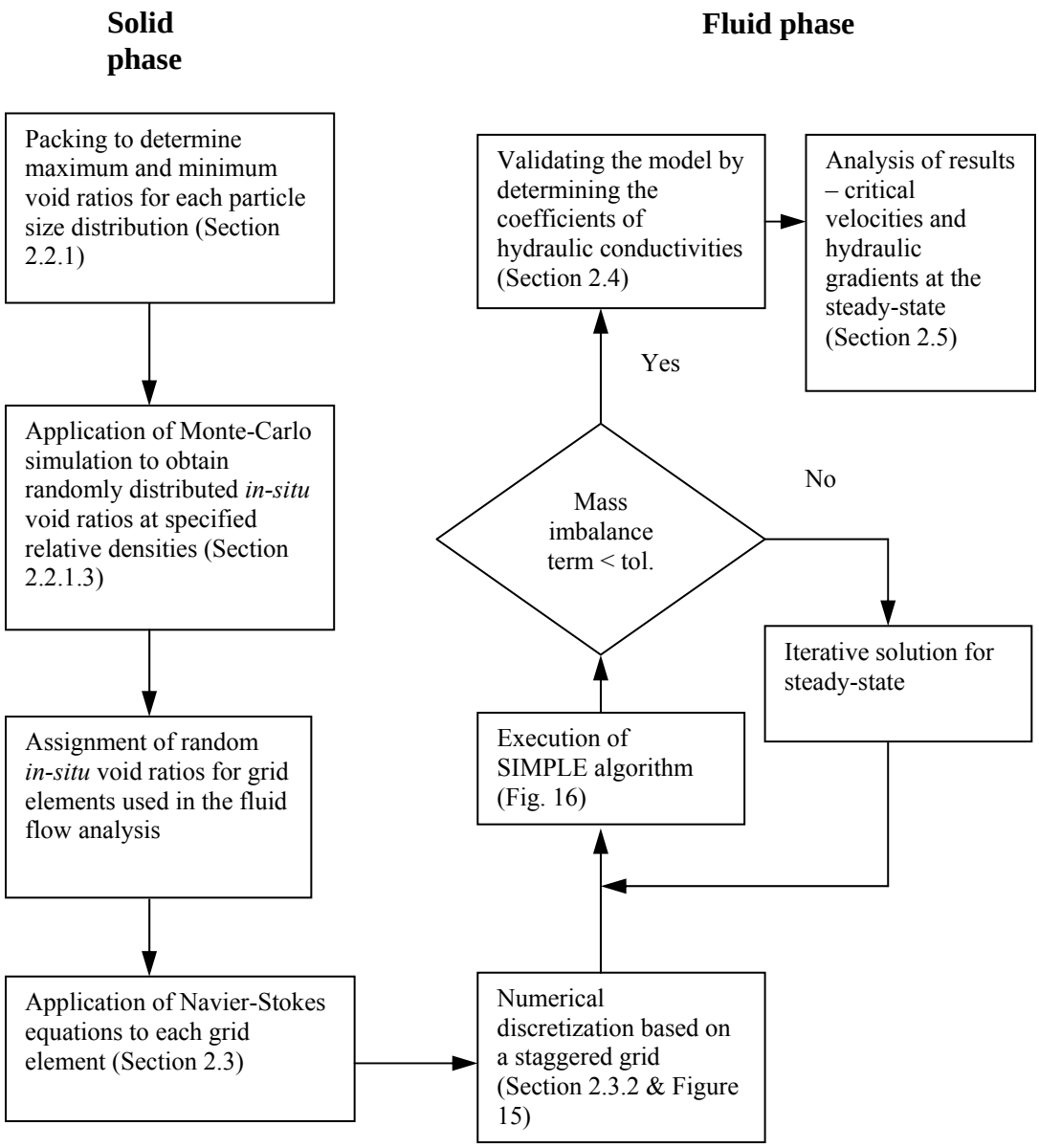

Figure 7: Flow Chart Illustrating the Analytical Model for Steady State Flow

2.2.1 Modeling of Soil Structure (3D Random Packing of Soil Particles)

The particle size distribution curves (PSDs) shown in Figure 8 were selected to satisfy the US. Army Corps of Engineers´ filter criteria (Eqn 2) for a typical pavement system made of a gravel base, a coarse sand subbase and a fine sand subgrade [12].

2.2.1.1 Simulation of Maximum and Minimum Void Ratios Using PSD

In this model the soil particles are assumed to be of spherical shape. To determine the maximum and minimum void ratios (e_{max} and e_{min}) corresponding to each soil type in Figure 8, a customized random packing algorithm was developed. In the case of gravel, 28 mm × 28 mm × 28 mm cubes were packed using the corresponding PSD in Figure 8. It can be noted that the PSDs in Figure 8 are cumulative probability distributions of particle size for each soil type. Therefore, by using an adequately large array of random numbers from a uniform distribution between 0 and 100 (the y axis range in Figure 8), one can select the corresponding array of particle diameters that conforms to a selected PSD, from the x axis. This technique, known as the Monte-Carlo simulation [14] is used to select the array of packing diameters for each cube. It is noted that the resulting maximum and minimum void ratio distributions change in each packing trial since the order of diameters used for packing is changed randomly. Similarly, 16 mm ×16 mm × 16 mm cubes and 3 mm ×3 mm × 3 mm cubes were used to obtain e_{max} and e_{min} in coarse sand packing and fine sand packing respectively (Figure 8). Smaller cubes are used to pack smaller particle sizes to reduce the computer running time assuming that an

adequate number of particles are within the cube to determine representative e_{max} and e_{min} for each type of soil.

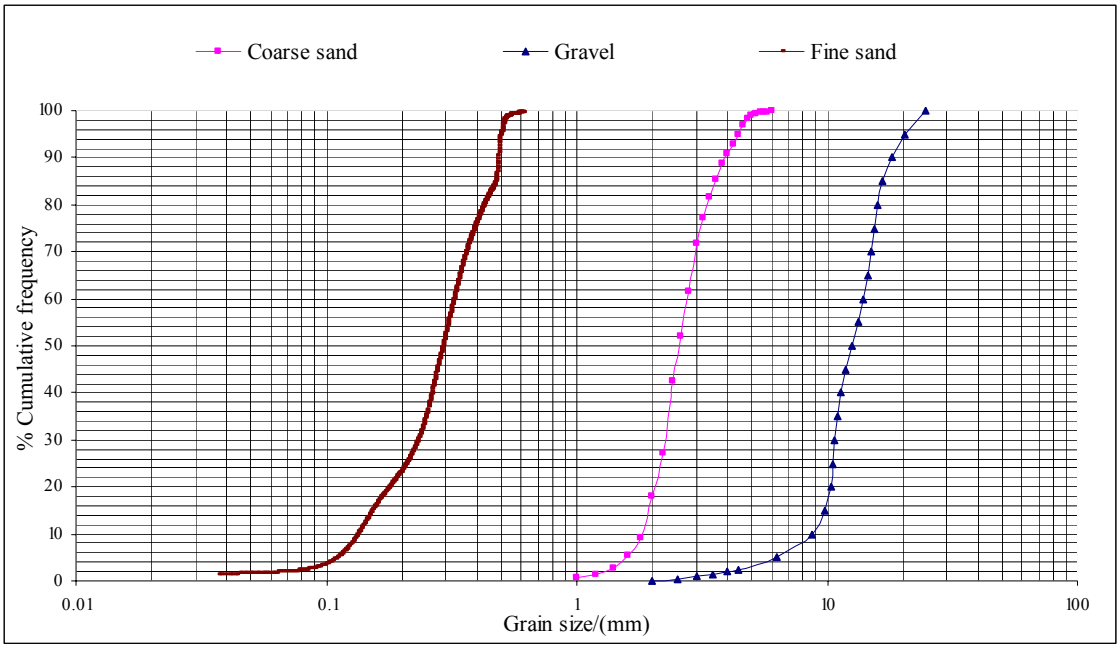

Figure 8: Particle Size Distributions for Gravel, Coarse Sand and Fine Sand

2.2.1.2 Implementation of the Packing Procedure

In order to obtain the loosest state of each type of soil (e_{max}) within the corresponding cubes described above, different sizes of soil particles inscribed in boxes are packed as indicated Figure 9a using a MATLAB code developed by the authors. The side length of each box is the same as the diameter of the inscribed soil particle. Based on the minimum particle diameter of the selected PSD, the side lengths of each cube is divided into a finite number of sub-divisions (Figure 9a). Then, the packing algorithm tracks the total number of sub-divisions occupied by each incoming box, i.e. each packed soil particle, as packing proceeds based on the Monte-Carlo simulation corresponding to a given PSD. Finally, the

automated algorithm fills the maximum possible number of sub-divisions until it finds that no space is available within the considered cube for further packing of soil particles from the given PSD.

On the other hand, in order to obtain the minimum void ratio (densest packing), the maximum number of spheres smaller than the inscribing sphere in each box is also packed into the unoccupied space at the corners of each box (Figure 9c and 9d) before that box is placed in the cube (Figure 9b). For each type of soil, 400 such cubes (trials) were packed randomly using the Monte-Carlo simulation. Since the maximum and minimum void ratios obtained in each trial would be different as explained above, they are considered as random variables. Thus, the probability distributions of e_{max} and e_{min} obtained from those 400 trials are shown in Figure 10. The ranges derived for e_{max} and e_{min} as shown in Table 1 agree with the typical values in [15].

Table 1: Size Characteristics of Pavement Layers

Soil type	**D_{15} (mm)**	**D_{50} (mm)**	**D_{85} (mm)**	**e_{min}**	**e_{max}**
Gravel	9.85	13	19	0.59 – 0.8	0.98 – 1.18
Coarse sand	1.85	2.5	3.5	0.73 – 0.93	0.91 – 1.10
Fine sand	0.16	0.29	0.49	0.54 – 0.79	0.91-1.26

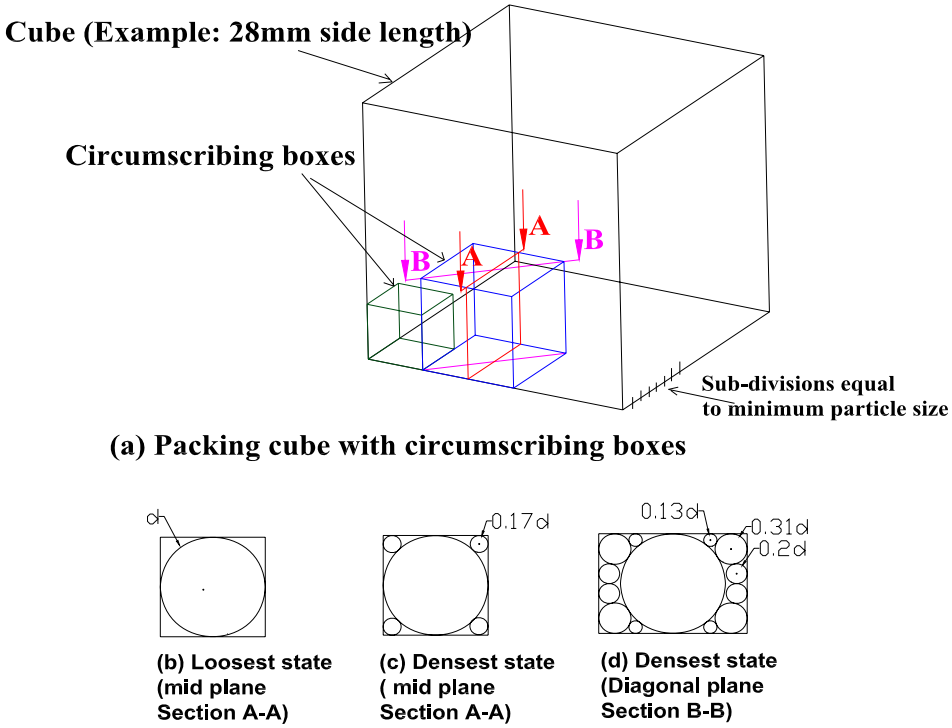

Figure 9: Random Packing of Soil Particles

2.2.1.3 Determination of the Natural Void Ratio Distribution

The concept of relative density is helpful in quantifying the level of compaction of coarse-grained soils. The relative density of a coarse-grained soil at a given compaction level expresses the ratio of the reduction in the voids at the given compaction level, to the maximum possible decrease in the voids (Eqn 3). The *in-situ* void ratio distribution (e) corresponding to a relative density (D_r) is obtained using the previously obtained e_{max} and e_{min} (Eqns 3 or 4).

$$D_r = \frac{e_{\max} - e}{e_{\max} - e_{\min}} \times 100\% \qquad (4)$$

or

$$e = \left(1 - \frac{D_r}{100}\right) e_{\max} + \frac{D_r}{100} e_{\min} \tag{5}$$

Where, e_{max} is the randomly distributed void ratio of gravel/sand in its loosest state. e_{min} is the randomly distributed void ratio of gravel/sand in its densest state. e is the randomly distributed void ratio of gravel/sand in its natura*l* state in the field.

Thus,

$$f_{en}(e) = F\left[f_{e\max}(e), f_{e\min}(e), D_r\right] \tag{6}$$

Where $f_{en}(e)$, $f_{e\max}(e)$ and $f_{e\min}(e)$ are Probability Density Functions (pdf) of *in-situ* natural void ratio, maximum void ratio and minimum void ratio respectively.

If e is a function of two random variables ($e_{max} = e_1$, $e_{min} = e_2$) and μ_1 and μ_2 are the mean values of these random variables, the expected mean value of "e" can be expressed using the second-order Taylor series approximation as

$$E(e) = e(\mu_1, \mu_2) + \frac{1}{2}\sum_{i=1}^{2}\sum_{i=1}^{2}\left(\frac{\partial^2 e}{\partial e_1 \partial e_2}\right) Cov[e_1, e_2] \tag{7}$$

Furthermore, the variance of "e" can be expressed as

$$V[e] = \sum_{i=1}^{2}\sum_{i=1}^{2}\left(\frac{\partial e}{\partial e_1}\right)_{\mu_1}\left(\frac{\partial e}{\partial e_2}\right)_{\mu_2} Cov[e_1, e_2] \tag{8}$$

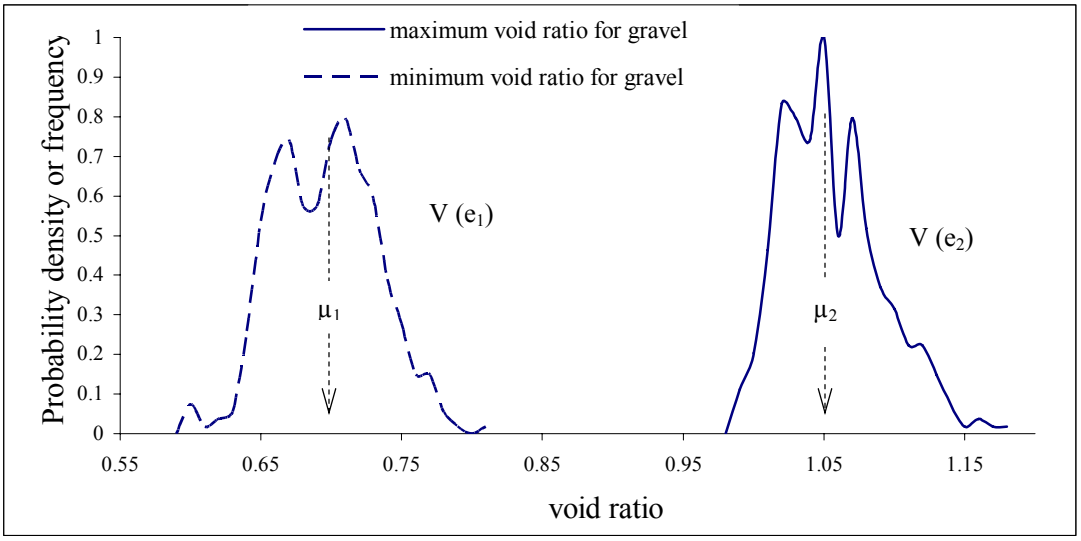

Figure 10: Probability Density Function (PDF) of Maximum and Minimum Void Ratios

Two alternative approaches can be followed to determine the probability distribution of the natural void ratio (e) from the probability distributions of the maximum and minimum void ratios (Eqn 5):

1) Assume an appropriate Probability Density Function (Example: Log-normal) with mean and variance calculated using Eqn 6 and Eqn 7 from the means (μ_1, μ_2) and variances (V (e_1), V (e_2)) of e_{max} and e_{min}.
2) Generating the probability distribution of natural void ratios (e) using Eqn 4 and the Monte-Carlo simulation technique.

In this model, the method (2) listed above is used. When the probability distributions of e_{max} and e_{min} are known for each soil type (Figure 10) the corresponding cumulative distributions of e_{max} and e_{min} can be derived (Figure 11). Then, once more the Monte-

Carlo simulation (Section 3.1) can be used to pick two arrays of e_{max} and e_{min} values for that soil type. Finally, with the e_{max} and e_{min} arrays, a corresponding array of natural void ratio (e) of any of the above soil types, for a given relative density (D_r) can be obtained from Eqn 4. The spatial distributions of natural void ratios (porosities) so obtained assumed to be representative of each soil layer will be used in the analysis of flow (Section 4).

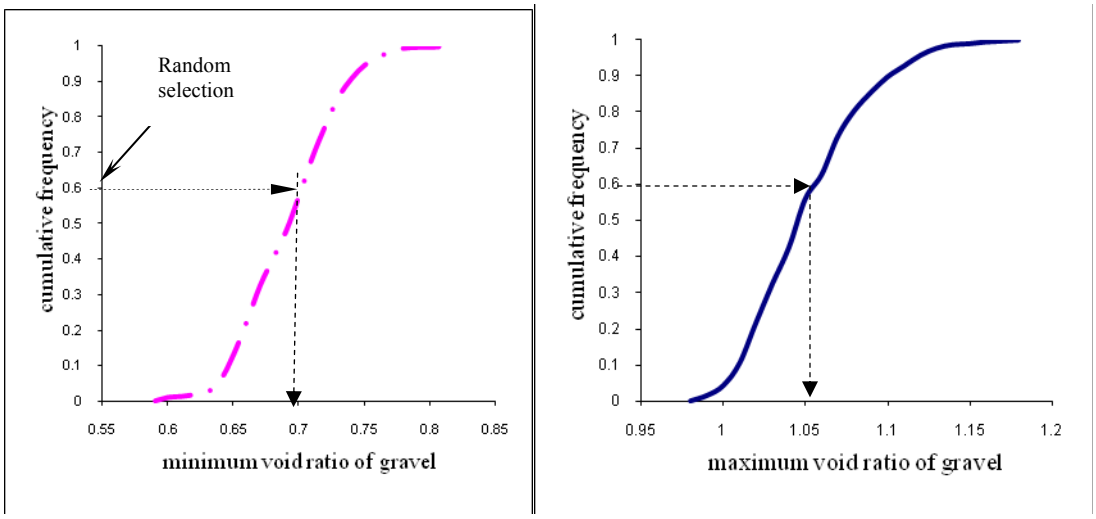

Figure 11: Cumulative Frequencies of Maximum and Minimum Void Ratios

2.3 Modeling of Steady State Flow

In modeling the pavement layers, the three dimensional porosities obtained from particle packing are coupled with two dimensional water flow. This is because flow is constrained in the third direction due to the two dimensional nature of the pavement. Due to the incompatibility of the sizes of the particles of the three layers and since the same grid element size is used for entire pavement structure, only two pavement layers are modeled at a time. Navier Stokes equations [13] are given by:

Mass Conservation (Continuity Equation):

$$\frac{\partial(nu)}{\partial x}+\frac{\partial(nv)}{\partial y} = 0 \tag{9}$$

Momentum Conservation (Momentum Equations):

X direction:

$$\frac{\partial(nu)}{\partial t}+\frac{\partial(nu^2)}{\partial x}+\frac{\partial(nuv)}{\partial y}=-\frac{n}{\rho}\frac{\partial p}{\partial x}+\frac{D_x}{\rho}+\frac{\mu}{\rho}\left(\frac{\partial^2 nu}{\partial x^2}+\frac{\partial^2 nu}{\partial y^2}\right) \tag{10}$$

Y direction:

$$\frac{\partial(nv)}{\partial t}+\frac{\partial(nuv)}{\partial x}+\frac{\partial(nv^2)}{\partial y}=-\frac{n}{\rho}\frac{\partial p}{\partial y}+\frac{D_y}{\rho}+\frac{\mu}{\rho}\left(\frac{\partial^2 nv}{\partial x^2}+\frac{\partial^2 nv}{\partial y^2}\right)+n\,g_y \tag{11}$$

Where, n – porosity at the location (x, y) at time t, u, v – fluid velocities in the x and y directions respectively, ρ – fluid density, p – fluid pressure, μ - fluid viscosity, g_y - gravitational force per unit mass in the y direction.

Averaged fluid-particle interactions (drag forces) are quantified using semi-empirical relationships provided in Eqn 9 [6].

$$D_x=-\left(150\,\frac{\mu(1-n)^2}{n^2\overline{d_p^2}}u+1.75\,\frac{(1-n)}{n^2\overline{d_p}}\rho u^2\right) \tag{12}$$

Where, $\overline{d_p}$ - averaged particle diameter; D_x – x directional average fluid-particle iteration force per unit volume. A similar expression for D_y is used for y directional averaged fluid-particle interactions.

2.3.1 Need for a Staggered Grid

The central difference form of Eqns 6 – 8 requires a staggered grid due to the two issues explained below:

$$\frac{u_{i+1,j} - u_{i-1,j}}{2\Delta x} + \frac{v_{i,j+1} - v_{i,j-1}}{2\Delta y} = 0 \qquad (13)$$

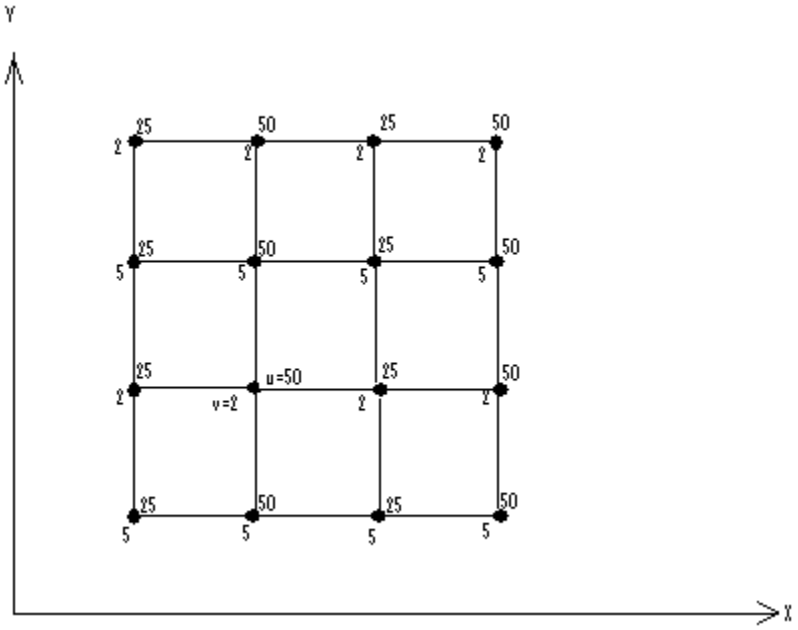

Figure 12: Discrete Checkerboard Velocity Distribution at Each Grid Point: At Each Node, the Top Number is u and the Bottom Number is v

Figure 12 illustrates an arbitrary zigzag type of distribution of both the x component and y components of velocity, u and v, respectively. When these arbitrary numbers are substituted in Eqn 12, the central difference form of the continuity equation for incompressible fluid flow is unconditionally satisfied. In other words, the checkerboard velocity distribution shown in Figure 12 produces a trivial solution inapplicable to a real physical flow field.

Considering a two-dimensional discrete, checkerboard pressure pattern as illustrated in Figure 13, the second order central difference formulation for the pressure gradients which appear in the momentum equations can be written as follows:

$$\frac{\partial P}{\partial x} = \frac{P_{i+1.j} - P_{i-1,j}}{2\Delta x} \tag{14}$$

$$\frac{\partial P}{\partial y} = \frac{P_{i,j+1} - P_{i,j-1}}{2\Delta y} \tag{15}$$

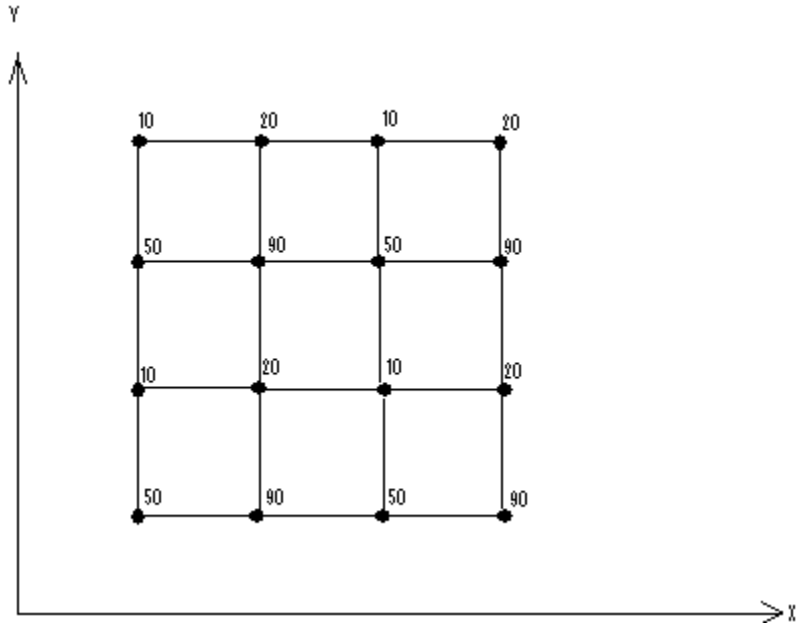

Figure 13: Discrete Checkerboard Pressure Distribution

The checkerboard pressure distribution (Figure 13) gives zero pressure gradients in the momentum equations in the x and y directions written in terms of the central difference scheme (Eqns 13 and 14 respectively). In other words, the pressure field would not be

incorporated in the discretized Navier Stokes equations and hence the numerical solution would effectively see only uniform pressure distributions in the x and y directions.

In order to address the above issue, an innovative remedy for the checkerboard distribution is to use a “staggered mesh” where discrete pressures and velocities are expressed only wherever required. A typical two-dimensional staggered mesh arrangement is shown in Figure 14. In the staggered grid, the velocity components are computed for the points that lie on the faces of the flow elements. Thus, the x-directional velocity, u, is computed on the planes or surfaces that are normal to the x-direction and similarly, the y-directional velocity, v, is computed on the planes or surfaces that are normal to the y-direction. On the other hand, the pressures are computed at the center of the flow elements.

By introducing a staggered grid, the mass flow rates across the flow element faces can be evaluated without any interpolation of the relevant velocity components. Moreover, for a typical flow element, it will be easy to see that the discretized continuity equation would contain the differences of adjacent velocity components thus preventing a wavy velocity field resulting from the continuity equation. When the staggered grid is used, only “realistic” velocity fields would have the possibility of being acceptable to the continuity equation. Consequently, pressure fields in the momentum equations would no longer be felt as uniform pressure fields.

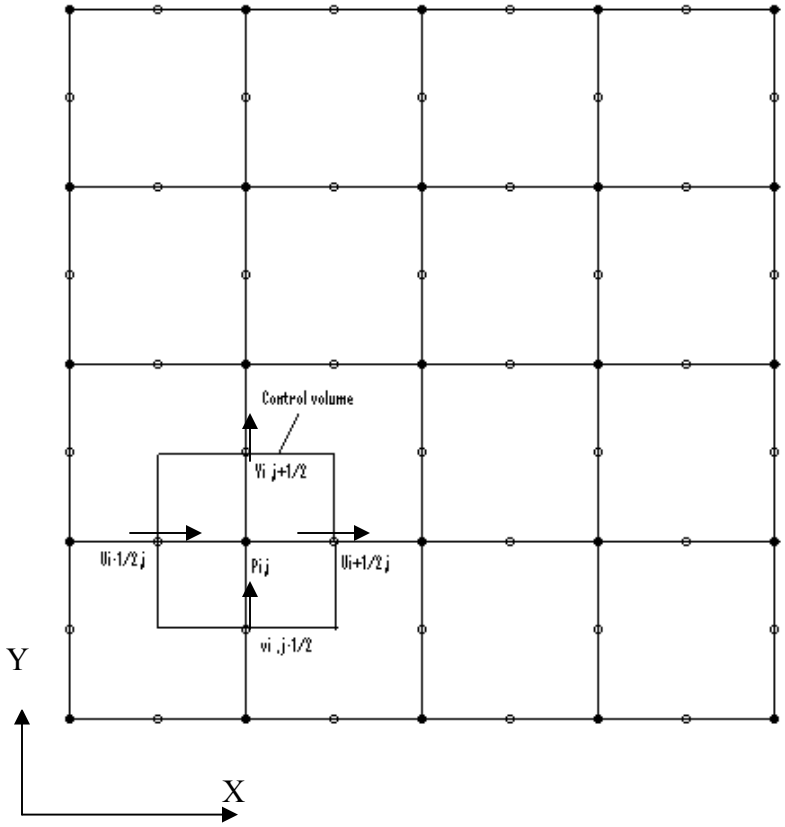

Figure 14: A Typical Staggered Grid Arrangement (Solid Circles Represent Pressure Nodes and Open Circles Represent Velocity Nodes)

2.3.2 Numerical Solution Technique

Based on the staggered grid arrangement introduced in Section 4.2, a finite-difference approach is used to discretize the Eqns 9, 10 and 11. The scheme is based on forward difference in time and central difference in space. The numerical form of the x directional momentum equation is written in Eqn 10, referring to the notation in Figure 15 for the sequential iteration steps of N and N+1.

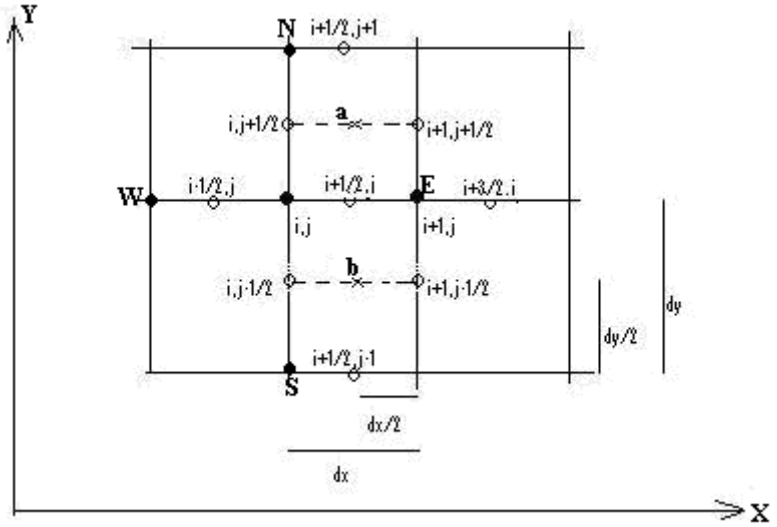

Figure 15: Computational Module for the X-Momentum Equation

$$\frac{n_{i,j}\,u_{i+1/2,j}^{N+1} - n_{i,j}\,u_{i+1/2,j}^{N}}{\Delta t} + \frac{n_{i+1,j}\,u_{i+3/2,j}^{2} - n_{i-1,j}\,u_{i-1/2,j}^{2}}{2\Delta x} + \frac{n_{i,j+1}\,u_{i+1/2,j+1}\,\overline{v}_{i+1/2,j+1/2} - n_{i,j-1}\,u_{i+1/2,j-1}\,\overline{\overline{v}}_{i+1/2,j-1/2}}{2\Delta y} =$$

$$-\frac{n_{i,j}}{\rho}\left(\frac{p_{i+1,j}-p_{i,j}}{\Delta x}\right) - \left(150\frac{\mu(1-n_{i,j})^2}{\rho\, n_{i,j}^2\,\overline{d_{p_{i,j}}^2}}\,u_{i-1/2,j} + 1.75\frac{(1-n_{i,j})}{n_{i,j}^2\,\overline{d_{p_{i,j}}}}\,u_{i-1/2,j}^2\right)$$

$$+\frac{\mu}{\rho}\left[\frac{n_{i+1,j}\,u_{i+3/2,j} + n_{i-1,j}\,u_{i-1/2,j} - 2n_{i,j}\,u_{i+1/2,j}}{(\Delta x)^2} + \frac{n_{i,j+1}u_{i+1/2,j+1} + n_{i,j-1}u_{i+1/2,j-1} - 2n_{i,j}\,u_{i+1/2,j}}{(\Delta y)^2}\right] \qquad (16a)$$

Where, At point a , $\overline{v}_{i+1/2,j+1/2} = \frac{1}{2}\left(v_{i,j+1/2} + v_{i+1,j+1/2}\right)$ (16b)

$$\text{At point b,}\quad \overline{\overline{v}}_{i+1/2,j-1/2} = \frac{1}{2}\left(v_{i,j-1/2} + v_{i+1,j-1/2} \right) \tag{16c}$$

Within the staggered grid some velocities need to be interpolated as shown in Eqns 16b and 16c. In a concise form, Eqn 16a can be written as

$$n_{i,j}\, u^{N+1}_{i+1/2,j} = n_{i,j}\, u^{N}_{i+1/2,j} + A(\Delta t) + \overline{A}\,(\Delta t)\left(\frac{p_{i+1,j} - p_{i,j}}{\Delta x} \right) + \overline{\overline{A}}\,(\Delta t) \tag{16d}$$

Where,

$$A = \frac{n_{i+1,j}\, u^2_{i+3/2,j} - n_{i-1,j}\, u^2_{i-1/2,j}}{2\Delta x} + \frac{n_{i,j+1}\, u_{i+1/2,j+1}\, \overline{v_{i+1/2,j+1/2}} - n_{i,j-1}\, u_{i+1/2,j-1}\, \overline{\overline{v_{i+1/2,j-1/2}}}}{2\Delta y} \tag{16e}$$

$$\overline{A} = -\frac{n_{i,j}}{\rho} \tag{16f}$$

and

$$\overline{\overline{A}} = -\left(150\frac{\mu(1-n_{i,j})^2}{\rho\, n^2_{i,j}\, \overline{d^2_{p_{i,j}}}}\, u_{i-1/2,j} + 1.75\frac{(1-n_{i,j})}{n^2_{i,j}\, \overline{d_{p_{i,j}}}}\, u^2_{i-1/2,j} \right) + \frac{\mu}{\rho}\left[\frac{n_{i+1,j}\, u_{i+3/2,j} + n_{i-1,j}\, u_{i-1/2,j} - 2\, n_{i,j}\, u_{i+1/2,j}}{(\Delta x)^2} + \frac{n_{i,j+1} u_{i+1/2,j+1} + n_{i,j-1} u_{i+1/2,j-1} - 2\, n_{i,j}\, u_{i+1/2,j}}{(\Delta y)^2} \right] \tag{16g}$$

The numerical form of the y directional momentum equation can be written similarly based on Eqn 11.

2.3.3 Semi-Implicit Method for Pressure-Linked Equations (SIMPLE) Algorithm

An iterative process called the pressure correction technique has found widespread application in the numerical solution of the incompressible, viscous Navier Stokes equations. This technique is a vehicle by which the velocity and pressure fields are directed towards a solution that satisfies both the discrete continuity and momentum equations. This technique is embodied in an algorithm called Semi-Implicit Method for Pressure-Linked Equations (SIMPLE) [11]. The primary idea behind SIMPLE is to create a discrete equation for pressure, in terms of the pressure correction, from the discrete continuity equation. Figure 16 shows the step-by-step procedure for the SIMPLE algorithm.

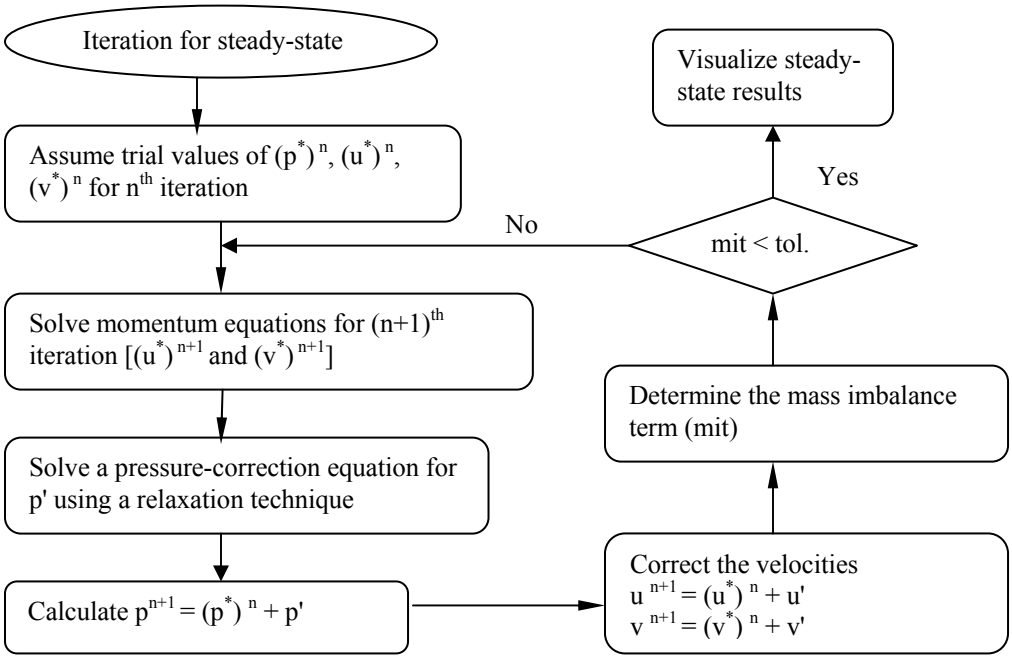

Figure 16: Flow Chart for SIMPLE Algorithm for Steady State Condition

2.3.3.1 Derivation of the Pressure Correction Formula

At the beginning of each new iteration, $p_{i,j}$ is set to $p^*_{i,j}$, where $p^*_{i,j}$ is the pressure from the previous iteration. Then, Eqn 16d will be transformed to Eqn 17.

$$n_{i,j}\, u^{*N+1}_{i+1/2,\,j} = n_{i,j}\, u^{*N}_{i+1/2,\,j} + A^*(\Delta t) + \bar{A}^*(\Delta t)\left(\frac{p^*_{i+1,j} - p^*_{i,j}}{\Delta x}\right) + \bar{\bar{A}}^*(\Delta t) \qquad (17)$$

Similarly re-arranged y directional equation would be Eqn 18.

$$n_{i,j}\, v^{*N+1}_{i,j+1/2} = n_{i,j}\, v^{*N}_{i,j+1/2} + B^*(\Delta t) + \bar{B}^*(\Delta t)\left(\frac{p^*_{i,j+1} - p^*_{i,j}}{\Delta y}\right) + \bar{\bar{B}}^*(\Delta t) + n_{i,j}\,\rho\, g_y \qquad (18)$$

Next, Eqns 17 and 18 are subtracted from Eqn 16d and its y directional counterpart to obtain Eqns 19 and 20 respectively.

$$n_{i,j}\, u'^{N+1}_{i+\frac{1}{2},j} = n_{i,j}\, u'^{N}_{i+\frac{1}{2},j} + \overline{A}'(\Delta t)\left(\frac{p'_{i+1,j} - p'_{i,j}}{\Delta x}\right) \tag{19}$$

$$n_{i,j}\, v'^{N+1}_{i,j+\frac{1}{2}} = n_{i,j}\, v'^{N}_{i,j+\frac{1}{2}} + \overline{B}'(\Delta t)\left(\frac{p'_{i,j+1} - p'_{i,j}}{\Delta y}\right) \tag{20}$$

Where, the pressure correction $p'_{i,j} = p_{i,j} - p^*_{i,j}$, $A' = A - A^*$, $\overline{\overline{A'}} = \overline{\overline{A}} - \overline{\overline{A^*}}$

and $\overline{A'} = \overline{A} = \overline{A^*} = -\frac{n_{i.j}}{\rho}$.

B' , $\overline{B'}$ and $\overline{\overline{B'}}$ can be defined similarly from the y directional coefficients.

Eqn 9 can be re-written in the discretized form as in Eqn 21 using the central difference scheme with the staggered grids,

$$\frac{n_{i+1,j}\, u_{i+\frac{1}{2},j} - n_{i,j} u_{i-\frac{1}{2},j}}{\Delta x} + \frac{n_{i,j+1}\, v_{i,j+\frac{1}{2}} - n_{i,j} v_{i,j-\frac{1}{2}}}{\Delta y} = 0 \tag{21}$$

The semi-implicit terminology refers to arbitrary setting of A', $\overline{\overline{A'}}$ and the corresponding y directional coefficients equal to zero, thus allowing the ultimate pressure correction formula, (Eqn 21), to have p′ appearing only at four neighborhood grid points illustrated in Figure 17. Omission of $u'^{N}_{i+\frac{1}{2},j}$, $v'^{N}_{i,j+\frac{1}{2}}$, A', $\overline{\overline{A'}}$ and the corresponding y directional coefficients in the pressure correction derivation does not affect the final solution because

the pressure correction and velocity corrections would in fact be zero for a converged solution. Arbitrarily setting $u'^{N}_{i+\frac{1}{2},j}$ and $v'^{N}_{i,j+\frac{1}{2}}$ equal to zero in Eqns 19 and 20 produce,

$$n_{i,j}\, u'^{N+1}_{i+\frac{1}{2},j} = n_{i,j}\, u^{N+1}_{i+\frac{1}{2},j} - n_{i,j}\, u^{*N+1}_{i+\frac{1}{2},j} = \overline{A}'(\Delta t)\left(\frac{p'_{i+1,j} - p'_{i,j}}{\Delta x}\right) \tag{22}$$

$$n_{i,j}\, v'^{N+1}_{i,j+\frac{1}{2}} = n_{i,j}\, v^{N+1}_{i,j+\frac{1}{2}} - n_{i,j}\, v^{*N+1}_{i,j+\frac{1}{2}} = \overline{B}'(\Delta t)\left(\frac{p'_{i,j+1} - p'_{i,j}}{\Delta y}\right) \tag{23}$$

Using Eqns 22 and 23, the discretized continuity equation (Eqn 21) can be expressed as a pressure correction formula in terms of $p'_{i,j}$ values of only the neighboring four grid points as illustrated in Figure 17 (Eqn 21).

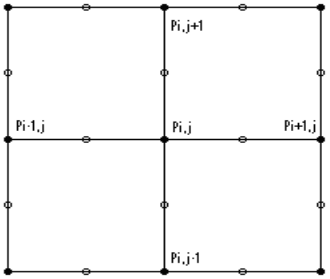

Figure 17: Designation of Nodal Points on a Grid Used in SIMPLE Algorithm

$$a_{i,j}\, p'_{i,j} + b_{i,j}\, p'_{i+1,j} + c_{i,j} p'_{i-1,j} + d_{i,j}\, p'_{i,j+1} + e_{i,j}\, p'_{i,j-1} + f_{i,j} = 0 \tag{24a}$$

Where,

$$a_{i,j} = 2\, n_{i,j}\left(\frac{\Delta t}{\rho(\Delta x)^2} + \frac{\Delta t}{\rho(\Delta y)^2}\right) \tag{24b}$$

$$b_{i,j} = -\, n_{i,j}\frac{\Delta t}{\rho(\Delta x)^2} \tag{24c}$$

$$c_{i,j} = -n_{i,j}\,\frac{\Delta t}{\rho(\Delta x)^2} \tag{24d}$$

$$d_{i,j} = -n_{i,j}\,\frac{\Delta t}{\rho(\Delta y)^2} \tag{24e}$$

$$e_{i,j} = -n_{i,j}\,\frac{\Delta t}{\rho(\Delta y)^2} \tag{24f}$$

and

$$f_{i,j} = \frac{\left(n_{i.j}\times u_{i,j+1}^{N+1} - n_{i.j}\times u_{i,j-1}^{N+1}\right)}{\Delta x} + \frac{\left(n_{i.j}\times v_{i+1,j}^{N+1} - n_{i.j}\times v_{i-1,j}^{N+1}\right)}{\Delta y} \tag{24g}$$

After determining the pressure correction, $p'_{i,j}$ from Eqn 24, the pressure and velocity components at every node are updated as follows:

$$p_{i,j} = p^{*}_{i,j} + p'_{i,j} \tag{25}$$

$$u_{i,j} = u^{*}_{i,j} + u'_{i,j} \tag{26}$$

$$v_{i,j} = v^{*}_{i,j} + v'_{i,j} \tag{27}$$

Where, $$u'_{i+\frac{1}{2},j} = \frac{\overline{A}'(\Delta t)}{n_{i,j}}\left(\frac{p'_{i+1,j} - p'_{i,j}}{\Delta x}\right) \tag{28}$$

and

$$v'_{i,j+\frac{1}{2}} = \frac{\overline{B}'(\Delta t)}{n_{i,j}}\left(\frac{p'_{i,j+1} - p'_{i,j}}{\Delta y}\right) \tag{29}$$

The pressure correction Equation (Eqn 24), which is of Poisson format in terms of p′, can be solved by employing a numerical relaxation technique. The term $f_{i,j}$ (Eqn 24g) is called the “mass imbalance term” which must vanish theoretically in the last iteration

where the velocity field converges to a field that satisfies the continuity equation (Eqn 9). In the numerical algorithm developed in this work, the mass imbalance term is used as a stopping criterion to assure that the solution converges to the correct velocity field. The function of the pressure correction formula is to set the iterative process in such a direction that, when the velocity distribution is determined from the momentum equations, it will eventually converge to the correct distribution which satisfies the continuity equation. Because the pressure correction method is designed to solve for the steady flow condition via an iterative process, the superscripts N and N+1 used in the equations are the sequential iteration steps, with no significance to any real transient variation. Under the steady state conditions, the term of Δt can be treated as a parameter which has some effect on the speed at which the convergence is achieved.

2.3.3.2 Boundary Conditions for Pavement System

The boundary conditions appropriate for the actual water flow through the pavement system are specified in the computer code as indicated in Figure 18.

1) At the inflow boundary, the pressure and velocities are specified. Hence, the pressure correction, p', is zero at the inflow boundary.
2) At the outflow boundary, the pressure is specified and velocity components are allowed to float. Hence, p' is zero at the outflow boundary as well.
3) At the vertical walls, the slip conditions are maintained. Thus, the velocity component, u, normal to the walls is set to zero.

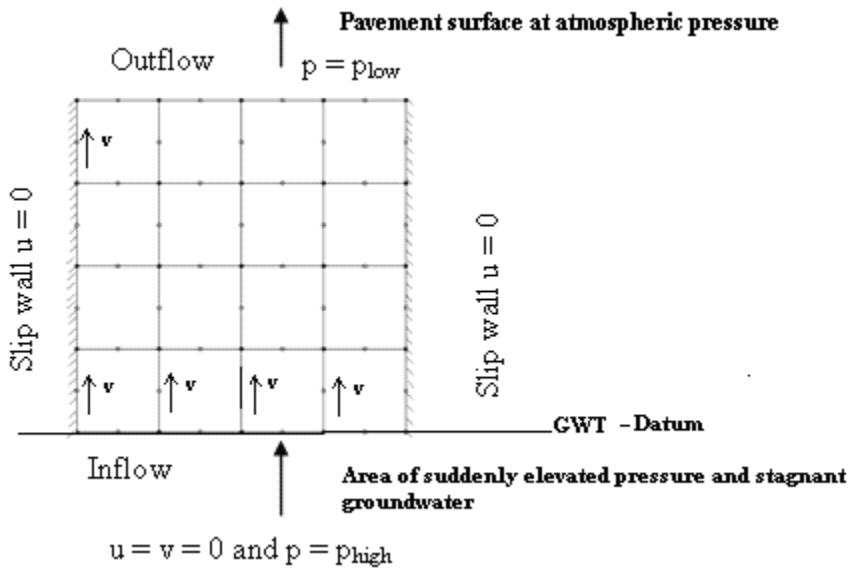

Figure 18: Boundary Conditions Incorporated in the Flow through the Pavement System

2.4 Validation of the Numerical Model

In order to validate the flow model described in Section 4, the coefficients of hydraulic conductivity of several uniformly graded soil types *which are not used in the current illustration* are determined from the numerical model and compared with widely used empirical relationships proposed by Hazen (Eqn 30) and Chapius (Eqn 31) [16]. The results of this comparison are summarized in Table 2.

$$k\ (cm/s) \quad = \quad c\,D_{10}^{2} \tag{30}$$

$$k(cm/s) = 2.4622\left[D_{10}^{2}\,\frac{e^{3}}{(1+e)}\right]^{0.7825} \tag{31}$$

Where, c - a constant that varies from 1.0 to 1.5 and D_{10} - the effective size in mm.

Table 2: Comparison of 3-D Coefficients of Hydraulic Conductivity Derived from SIMPLE Algorithm

Soil type (1)	Effective size (D_{10}) mm (2)	K_{model} (cm/s) (3)	K_{Hazen} (cm/s) (4)	$K_{Chapius}$ (cm/s) (5)
a	0.5	0.979871	0.375	0.497428
b	1	3.108229	1.5	1.47206
c	2	6.811264	6	4.532172
d	3	9.374428	9	8.247057
e	4	12.34681	16	12.94549

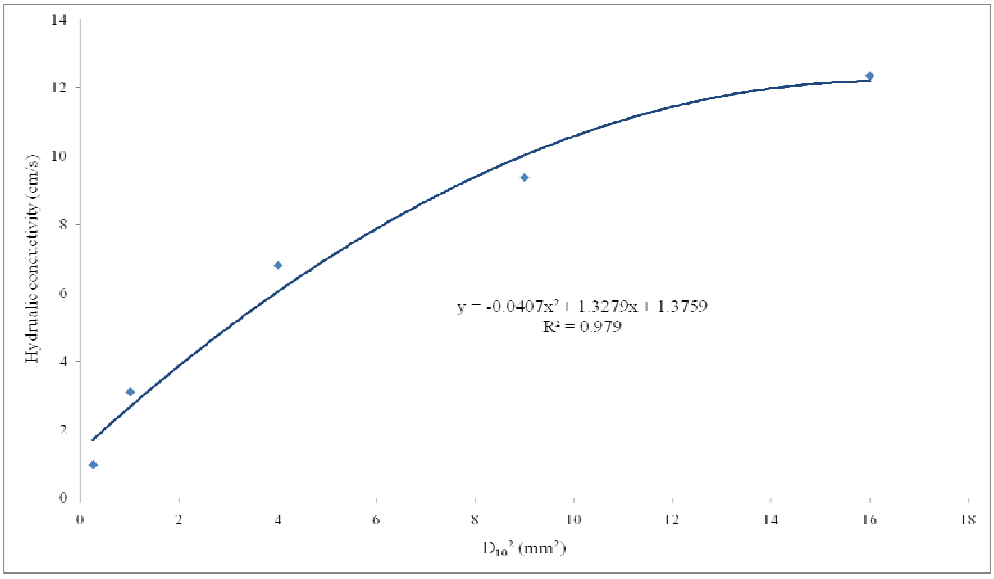

Figure 19: Relationship between Hydraulic Conductivity Vs Diameter for Uniformly Distributed Soils

It can be concluded from Table 2 that the coefficients of hydraulic conductivities determined from the model agree fairly well with those computed from common empirical relationships. Furthermore, it was determined that the coefficients of hydraulic conductivity for gravel, coarse sand and fine sand used in the Numerical Illustration

(Section 7) are 0.097 m/s ,0.043 m/s and 0.00024 m/s respectively. These values are within the ranges of typical hydraulic conductivities presented in the literature [16] for the corresponding PSDs shown in Figure 8. According to the developed model, the relationship between hydraulic conductivity Vs square of the tenth percentile diameter for uniformly distributed soils is shown in Figure 19. Therefore, the empirical equation (Eqn 45) does not seem to be accurate.

2.5 Numerical Illustration

The numerical model was applied to the pavement layer interfaces shown in Figure 2. The material properties and other model parameters shown in Table 1 and 3 were used for this purpose.

Table 3: Model Parameters

Particles	
Number of gravel particles considered for determining the porosity distribution	137668
Number of coarse sand particles considered for determining the porosity distribution	205332
Number of fine sand particles considered for determining the porosity distribution	855450
Gravel particle size	2 mm- 24 mm
Coarse sand particle size	1 mm- 5mm
Fine sand particle size	0.04 mm – 0.62 mm
Average density of saturated soil	1900 kg/m^3
Average compression index for granular soils	0.37 [18]
Specific gravity of soil	2.65
Average void ratio of gravel packing (D_r = 50%)	0.86
Average void ratio of coarse sand packing (D_r = 50%)	0.90
Average critical hydraulic gradient	0.88
Water	
Density	1000 Kg/m^3
Dynamic viscosity	10^{-3} Pa.s
Flow calculations	
Gravitational acceleration	9.81 m/s^2
Number of grid elements	50 by 50

2.5.1 Results of Numerical Illustration

Figure 20 and Figure 21 illustrate the progression of flow rate with iterations through different soil layers for different levels of compaction. They clearly reveal the reduction in flow rate due to densification and the impact of the hydraulic conductivity.

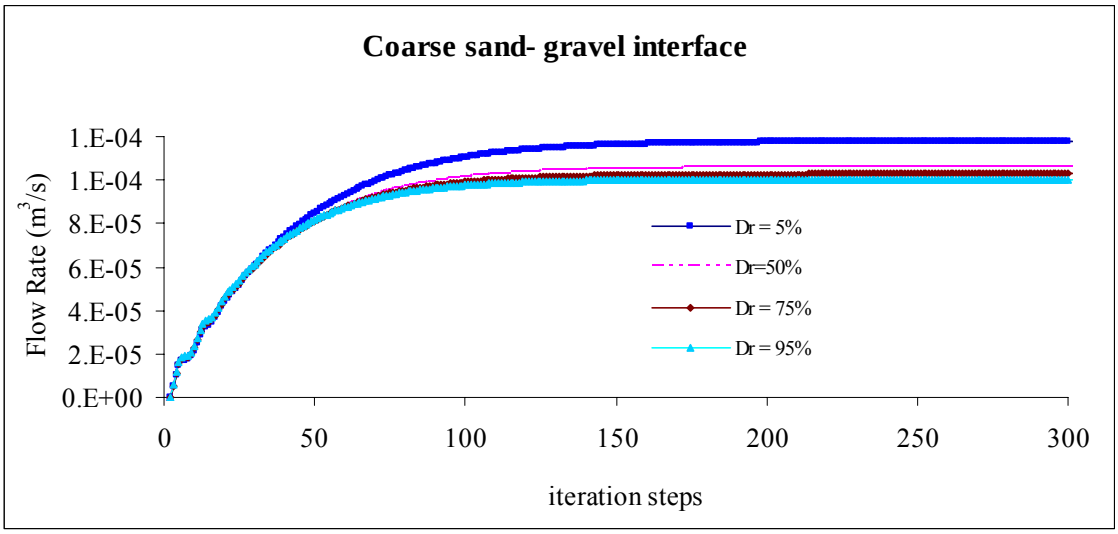

Figure 20: Plot of Flow Rate through Coarse Sand-Gravel Interface Vs Iteration Steps with Different Levels of Compaction (For Pressure Differential of 23 kPa)

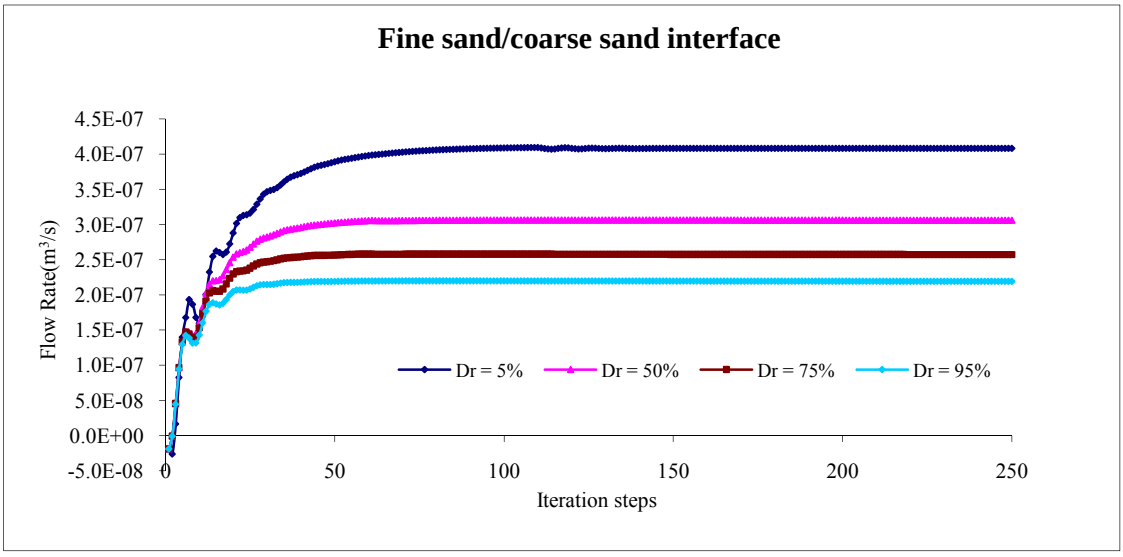

Figure 21: Plot of Flow Rate through Fine Sand-Coarse Sand Interface Vs Iteration Steps with Different Levels of Compaction (For Pressure Differential of 23 kPa)

Figure 22 shows that at the steady state the local hydraulic gradients at the interface are larger than that at other locations. They also clearly exceed the values predicted by conventional analysis (Darcy's law).

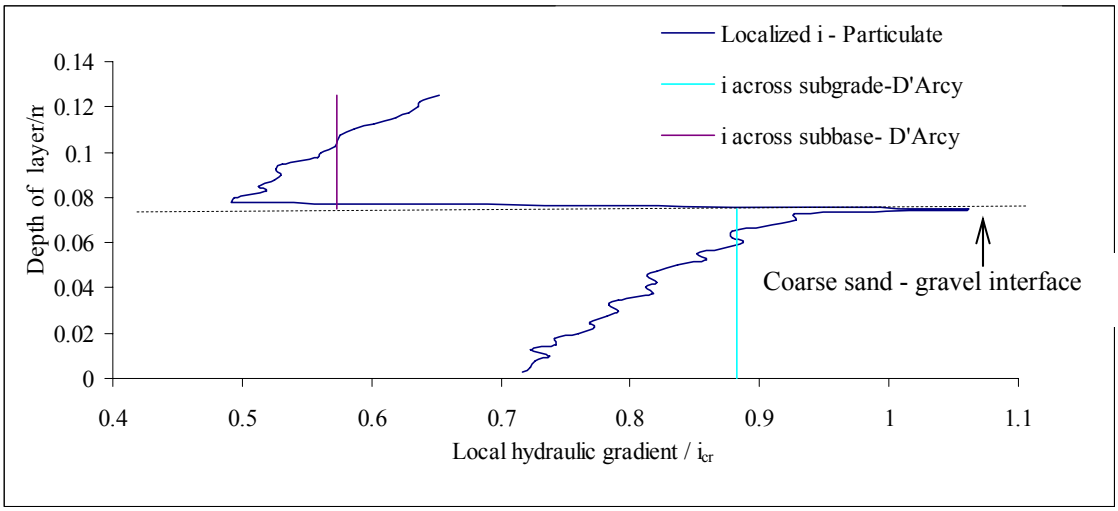

Figure 22: Comparison of Hydraulic Gradients Obtained Using Continuum and Particulate Approaches (Using SIMPLE Algorithm Steady State)

It is seen from Figure 23 that when the hydraulic gradient is 1.7 times the critical hydraulic gradient, the water flow never reaches a steady state.

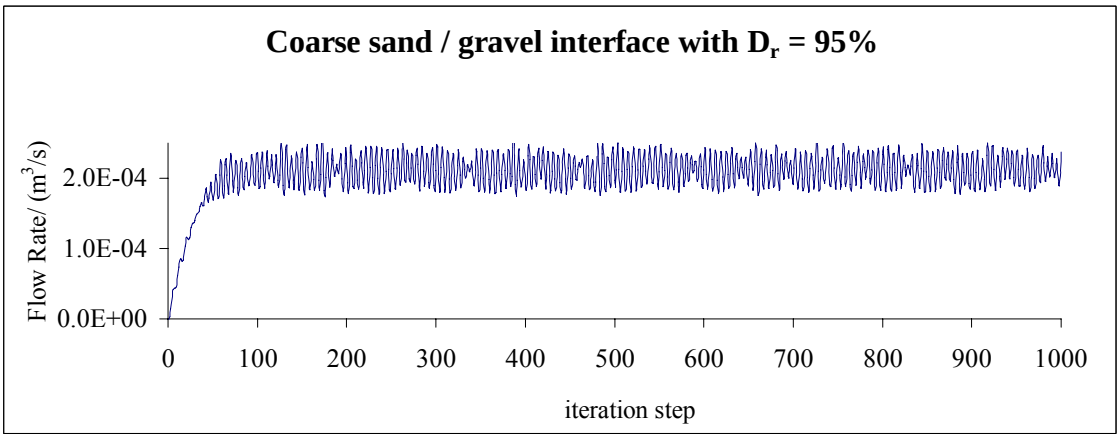

Figure 23: Plot of Flow Rate Vs Iteration Step for High Hydraulic Gradient (i = 1.7 i_{cr})

2.6 Conclusions

The current practice of designing pavement filter systems does not consider

1) The interaction between pore water and the individual soil particles.
2) The localized effects.

In order to determine the realistic limiting hydraulic gradients that can be applied within pavement layers, a design methodology based on a particulate approach that incorporates particle-soil interaction needs to be used. In this Chapter, the steady state water seepage in two saturated filter interfaces with varying levels of compaction was analyzed using a soil particulate model. The particulate effects of soil with different levels of compaction were incorporated conveniently in the model using a random packing technique, while the flow of water within the particulate assembly was modeled by the Navier Stokes flow equations. Two separate filter interfaces, i.e. coarse sand-gravel and fine sand-coarse sand were assembled using particle size distributions that satisfied the conventional filter design criteria. Then, a pressure differential that corresponded to the critical hydraulic gradient was applied across the layer interface. In order to verify the model, the coefficients of hydraulic conductivity predicted from the model are compared with those computed from the empirical relationships widely used in drainage design. The steady state flow algorithm is modified in the next Chapter to analyze the transient behavior of seepage through two-layer particulate pavement system which predicts the critical conditions for erosion, piping and clogging.

CHAPTER THREE

ANALYSIS OF TRANSIENT WATER SEEPAGE IN A PAVEMENT SYSTEM USING THE PARTICULATE APPROACH

3.1 Modeling of Transient Flow

The comprehensive analytical procedure and the computer code developed for its implementation are illustrated in Figure 24. The analytical procedure consists of two primary tasks such as the random assembly of the particulate medium (granular soil) and the solution of the fluid flow governing equations using partial coupling between the two media. The flow chart also includes the sections, equation numbers and figure numbers corresponding to each stage.

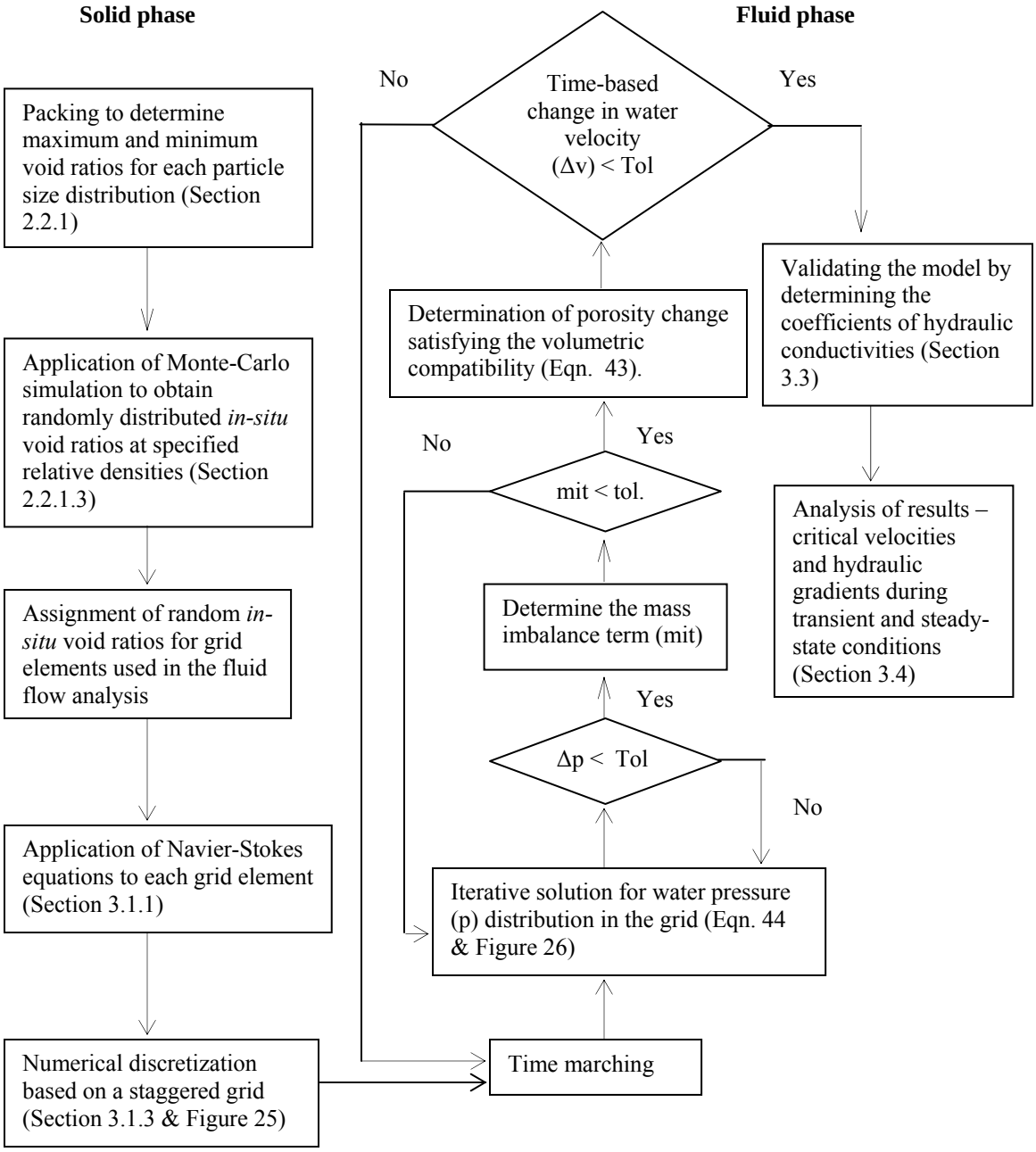

Figure 24: Flow Chart Illustrating the Analytical Model for Transient and Steady State Flow

3.1.1 Transient Navier Stokes Equations

In modeling the pavement layers, the three dimensional porosities obtained from particle packing are coupled with two dimensional water flow. This is because flow is constrained in the third direction due to the two dimensional nature of the pavement. Navier Stokes equations [13] are given by:

Mass Conservation (Continuity Equation):

$$\frac{\partial n}{\partial t} + \frac{\partial (nu)}{\partial x} + \frac{\partial (nv)}{\partial y} = 0 \tag{32}$$

Momentum Conservation (Momentum Equations):

X direction:

$$\frac{\partial (nu)}{\partial t} + \frac{\partial (nu^2)}{\partial x} + \frac{\partial (nuv)}{\partial y} = -\frac{n}{\rho}\frac{\partial p}{\partial x} + \frac{D_x}{\rho} + \frac{\mu}{\rho}\left(\frac{\partial^2 nu}{\partial x^2} + \frac{\partial^2 nu}{\partial y^2}\right) \tag{33}$$

Y direction:

$$\frac{\partial (nv)}{\partial t} + \frac{\partial (nuv)}{\partial x} + \frac{\partial (nv^2)}{\partial y} = -\frac{n}{\rho}\frac{\partial p}{\partial y} + \frac{D_y}{\rho} + \frac{\mu}{\rho}\left(\frac{\partial^2 nv}{\partial x^2} + \frac{\partial^2 nv}{\partial y^2}\right) + n\, g_y \tag{34}$$

Where, n – porosity at the location (x, y) at time t, u, v – fluid velocities in the x and y directions respectively, ρ – fluid density, p – fluid pressure, μ - fluid viscosity, g_y - gravitational force per unit mass in the y direction.

Averaged fluid-particle interactions (drag forces) are quantified using semi-empirical relationships provided in Eqn 35 [6].

$$D_x = -\left(150\,\frac{\mu (1-n)^2}{n^2 \overline{d_p^2}}u + 1.75\,\frac{(1-n)}{n^2 \overline{d_p}}\rho u^2\right) \tag{35}$$

Where, $\overline{d_p}$ - averaged particle diameter; D_x – x directional average fluid-particle iteration force per unit volume. A similar expression for D_y is used for y directional averaged fluid-particle interactions.

3.1.2 Volumetric Compatibility of Solid and Fluid Phases

The effective stress in the soil phase can be expressed using Eqn 36 [16].

$$\sigma' = \sigma - u \tag{36}$$

Where, σ' - effective vertical stress, σ - total vertical stress and u - pore water pressure

After each time step, when the effective stress changes due to the change in pore water pressure, the void ratio must change according to the compressibility characteristics of the soil. The typical log-linear void ratio versus effective stress relation [16] that characterizes saturated fine-grained soil (clay, silt) is assumed for coarse-grained soil (gravel, sand) as well (Eqn 37).

$$e = e_o - C_c \log(\sigma') \tag{37a}$$

$$de = -\frac{(0.4343)C_c}{\sigma'} d\sigma' \tag{37b}$$

Where, C_c is the equivalent compression index of the soil. The corresponding void ratio change can be obtained using Equations (38a) and (38b).

$$n = \frac{e}{1+e} \tag{38a}$$

$$dn = de(1-n)^2 \tag{38b}$$

3.1.3 Numerical Solution Technique

A finite-difference approach [12] is used to discretize the Eqns 32, 33 and 34. The scheme is based on forward difference in time and porosity, and central difference in space. A typical two-dimensional staggered mesh arrangement [11, 13] was used to discretize the Eqns 32, 33 and 34. On the other hand, Patankar's original formulation [11] is based on the "pressure correction method" involving a finite-volume approach.

The pavement layers were divided into a 50 × 50 grid for the finite difference analysis. One fluid cell, known herein as a grid element, was selected to be 25 mm × 25 mm × 1m (2-D flow) to be compatible with the cube sizes (28 mm × 28 mm × 28 mm or 16 mm × 16 mm × 16 mm) used for packing (Section 3.1). 1 m has been selected in the third direction assuming two dimensional water flow. Since the Navier Stokes equations are written in terms of porosities, the spatial probability distribution of natural void ratios are first converted to porosities (Eqn 41a). First, natural porosities (void ratios) were assigned to each grid element based on the spatial probability distribution of natural void ratios determined from packing (Section 3.3). Within each grid element, the fluid-particle interaction is quantified considering the averaged particle diameter which is defined as the arithmetic mean of the diameters of all the particles in each grid. The authors´ modified numerical scheme is described as follows:

Eqn 39a expresses the x directional momentum equation in the numerical form for the sequential time steps of N and N+1 referring to the notation in Figure 25.

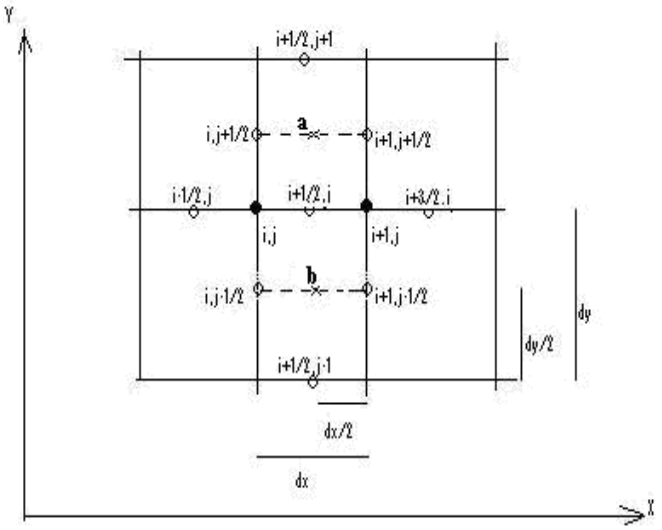

Figure 25: Computational Grid for the X-Momentum Equation

$$\frac{n_{i+1/2,j}\,u^{N+1}_{i+1/2,j} - n_{i+1/2,j}\,u^{N}_{i+1/2,j}}{\Delta t} + \frac{n_{i+3/2,j}\,u^{2}_{i+3/2,j} - n_{i-1/2,j}\,u^{2}_{i-1/2,j}}{2\Delta x} + \frac{n_{i,j+1}\,u_{i+1/2,j+1}\,\overline{v_{i+1/2,j+1/2}} - n_{i,j-1}\,u_{i+1/2,j-1}\,\overline{\overline{v_{i+1/2,j-1/2}}}}{2\Delta y} =$$

$$-\frac{n_{i,j}}{\rho}\left(\frac{p_{i+1,j}-p_{i,j}}{\Delta x}\right) - \left(150\frac{\mu(1-n_{i,j})^2}{\rho\, n_{i,j}^2\,\overline{\overline{d^2_{p_{i,j}}}}}u_{i-1/2,j} + 1.75\frac{(1-n_{i,j})}{n_{i,j}^2\,\overline{\overline{d_{p_{i,j}}}}}u^2_{i-1/2,j}\right)$$

$$+\frac{\mu}{\rho}\left[\begin{array}{l}\dfrac{n_{i+1,j}\,u_{i+3/2,j} + n_{i-1,j}\,u_{i-1/2,j} - 2n_{i,j}\,u_{i+1/2,j}}{(\Delta x)^2} + \\ \dfrac{n_{i,j+1}u_{i+1/2,j+1} + n_{i,j-1}u_{i+1/2,j-1} - 2n_{i,j}\,u_{i+1/2,j}}{(\Delta y)^2}\end{array}\right] \qquad (39a)$$

Where,

At point **a**, $\overline{v_{i+1/2,\,j+1/2}} = 1/2\left(v_{i,j+1/2} + v_{i+1,j+1/2}\right)$ (39b)

At point **b**, $$\overline{\overline{v_{i+1/2,\,j-1/2}}} = 1/2\left(v_{i,\,j-1/2} + v_{i+1,\,j-1/2} \right) \tag{39c}$$

Similarly, the y directional momentum equation can be written numerically.

Equations (37b) and (38b) can be used to express the change in porosity within the time interval Δt using the volumetric compatibility between solid and fluid phases. Then, Eqn 32 can also be discretized as follows:

$$\left[\frac{n_{i+1/2,j}\, u^{N+1}_{i+1/2,j} - n_{i-1/2,j}\, u^{N+1}_{i-1/2,j}}{\Delta x} + \frac{n_{i,j+1/2}\, v^{N+1}_{i,j+1/2} - n_{i,j-1/2}\, v^{N+1}_{i,j-1/2}}{\Delta y} \right] = -\frac{\Delta n}{\Delta t}$$

$$= \left[\frac{0.4343\, C_c \left(1 - n_{i,j}\right)^2 \left[p^{N}_{i,j} - p^{N-1}_{i,j} \right]}{\sigma^{N}_{i,j} - p^{N}_{i,j}} \right] \frac{1}{\Delta t} \tag{40}$$

To compute the change in porosity in the transient continuity equation in an explicit manner, the water pressure difference between the time steps (N-1) and N has been used in Eqn 40. By substituting velocities of the new time step by those of the previous time step, Eqn 40 is reduced to Eqn 41, which is a Poisson equation in terms of water pressure (p).

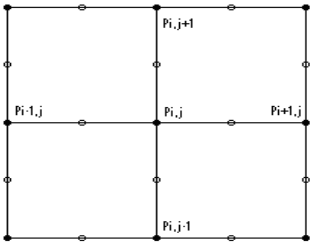

Figure 26: Designation of Nodal Points on a Grid Used in the Iterative Procedure

$$a_{i,j}\, p_{i,j} + b_{i,j}\, p_{i+1,j} + c_{i,j} p_{i-1,j} + d_{i,j}\, p_{i,j+1} + e_{i,j}\, p_{i,j-1} + S_{i,j} = 0 \tag{41a}$$

Where,

$$a_{i,j} = \left[\left(\frac{n_{i+1/2,j} + n_{i-1/2,j}}{\Delta x^2}\right) + \left(\frac{n_{i,j+1/2} + n_{i,j-1/2}}{\Delta y^2}\right)\right]\frac{\Delta t^2}{\rho} - 0.4343 C_c \frac{\left(1 - n_{i,j}\right)^2}{\sigma_{i,j} - p_{i.j}^N} \tag{41b}$$

$$b_{i,j} = -\left(\frac{n_{i+1/2,j}}{\Delta x^2}\right)\frac{\Delta t^2}{\rho} \tag{41c}$$

$$c_{i,j} = -\left(\frac{n_{i-1/2,j}}{\Delta x^2}\right)\frac{\Delta t^2}{\rho} \tag{41d}$$

$$d_{i,j} = -\left(\frac{n_{i,j+1/2}}{\Delta y^2}\right)\frac{\Delta t^2}{\rho} \tag{41e}$$

$$e_{i,j} = -\left(\frac{n_{i,j-1/2}}{\Delta y^2}\right)\frac{\Delta t^2}{\rho} \tag{41f}$$

and

$$S_{i,j} = \left(A_{i+1/2,j}^N - A_{i-1/2,j}^N\right)\frac{\Delta t^2}{\Delta x} + \left(\bar{\bar{A}}_{i+1/2,j}^N - \bar{\bar{A}}_{i-1/2,j}^N\right)\frac{\Delta t^2}{\Delta x} + \left(B_{i,j+1/2}^N - B_{i,j-1/2}^N\right)\frac{\Delta t^2}{\Delta y}$$
$$+\left(\bar{\bar{B}}_{i,j+1/2}^N - \bar{\bar{B}}_{i,j-1/2}^N\right)\frac{\Delta t^2}{\Delta y} + \frac{\left(n_{i+1/2.j} \times u_{i+1/2,j}^N - n_{i-1/2.j} \times u_{i-1/2,j}^N\right)}{\Delta x}\Delta t +$$
$$\frac{\left(n_{i.j+1/2} \times v_{i,j+1/2}^N - n_{i.j-1/2} \times v_{i,j-1/2}^N\right)}{\Delta y}\Delta t + \frac{0.4343 C_c \left(1 - n_{i,j}\right)^2}{\sigma_{i,j} - p_{i,j}^N} p_{i,j}^{N-1}$$
$$+\left(n_{i,j+1/2} - n_{i,j-1/2}\right) g_y \frac{\Delta t^2}{\Delta y} \tag{41g}$$

Where, A, $\bar{\bar{A}}$, B and $\bar{\bar{B}}$ is a collection of velocity derivatives from the discretized momentum equations in both x and y directions.

Similar to the pressure correction method introduced by Patankar [11], the authors´ modified algorithm solves the Poisson equation (Eqn 41) iteratively in terms of water pressures (p) at the neighboring nodes shown in Figure 26. Within each time step, when the water pressure difference at any node computed in each iteration becomes negligible, the algorithm checks the volumetric compatibility of solid and fluid phases throughout the entire pavement system (Eqn 40). Until the velocities become constant at each node, the time marching is continued while solving for water pressures iteratively at each time step (Figure 24).

3.1.4 Boundary Conditions

The boundary conditions appropriate for the actual water flow through the pavement system are specified in the computer code as indicated in Figure 27.

1) At the inflow boundary, the pressure and velocities are specified.
2) At the outflow boundary, the pressure is specified and velocity components are allowed to float.
3) At the vertical walls, the slip conditions are maintained. Thus, the velocity component, u, normal to the walls is set to zero.

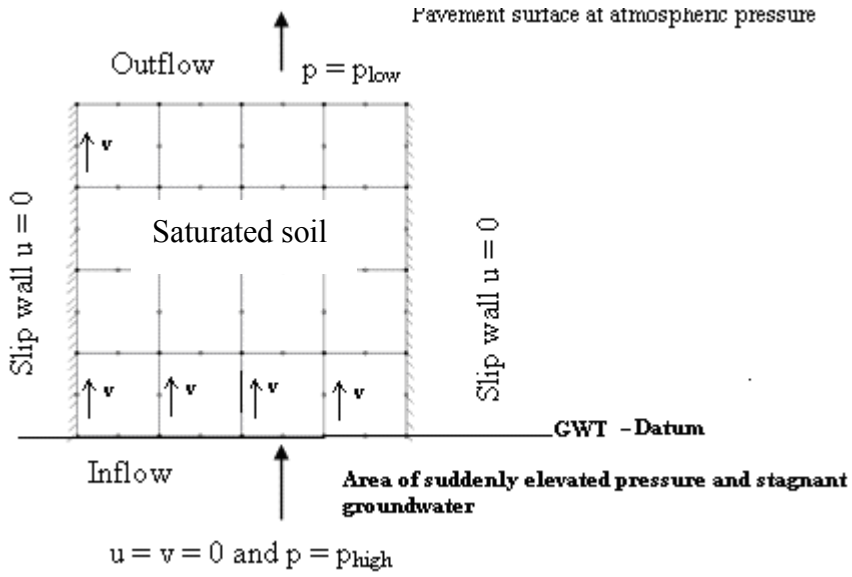

Figure 27: Boundary Conditions Incorporated in the Flow through the Pavement System (Saturated Soil)

3.2 Interface Effect in FDM

Since the hydraulic properties are different in different layers, Eqn 44 must be solved separately within each layer excluding the interface grid points. On the other hand, at the interface, Eqn 44h is used to satisfy the continuity of flow from one layer to the other.

$$\left(n_{i,j-1/2}+n_{i,j+1/2}\right)p_{i,j}^{\text{interface}} = n_{i,j-1/2}\,p_{i,j-1} + n_{i,j+1/2}\,p_{i,j+1} + k_{i,j-1/2}v_{i,j-1/2} + k'_{i,j-1/2}v^2_{i,j-1/2} - k_{i,j+1/2}v_{i,j+1/2} - k'_{i,j+1/2}v^2_{i,j+1/2} \quad (41h)$$

Where, $k_{i,j-1/2} = \dfrac{-150\,\mu\left(1-n_{i,j-1/2}\right)^2}{\rho\, n_{i,j-1/2}^2\,\overline{d^2_{p_{i,j-1/2}}}}\Delta y$ and $k'_{i,j-1/2} = \dfrac{-1.75\left(1-n_{i,j-1/2}\right)^2}{n^2_{i,j-1/2}\,\overline{d_{p_{i,j-1/2}}}}\Delta y$

3.3 Validation of the Numerical Models

In order to validate the flow model described in Section 3.2, the coefficients of hydraulic conductivity of several uniformly graded soil types *which are not used in the current illustration* are determined from the numerical model and compared with widely used empirical relationships proposed by Hazen (Eqn 42) and Chapius (Eqn 43) [16]. The results of this comparison are summarized in Table 4.

$$k\ (cm/s) \quad = \quad c\,D_{10}^{2} \tag{42}$$

$$k(cm/s) = 2.4622\left[D_{10}^{2}\,\frac{e^{3}}{(1+e)} \right]^{0.7825} \tag{43}$$

Where, c – a constant that varies from 1.0 to 1.5 and D_{10} - the effective size in mm.

Table 4: Comparison of 3-D Coefficients of Hydraulic Conductivity Derived from the Numerical Methodology

Soil type	Effective size (D_{10}) mm	K from steady flow model using SIMPLE algorithm (Chapter 2) (cm/s)	$K_{from\ current\ model}$ (cm/s)	K_{Hazen} (cm/s)	$K_{Chapius}$ (cm/s)
a	0.5	0.979871	1.01984	0.375	0.497428
b	1	3.108229	3.230112	1.5	1.47206
c	2	6.811264	6.766702	6	4.532172
d	3	9.374428	9.603897	9	8.247057
e	4	12.34681	11.62177	16	12.94549

In order to solve the transient continuity equation and Navier Stokes equations, the authors have developed the model presented in this study considering the volumetric compatibility between solid and fluid phases. As opposed to Patankar's work [11], there is no pressure correction method involved in the authors' modification. Instead, an elliptic equation in terms of the water pressure is iteratively solved until the volumetric imbalance in any grid element becomes negligible. The coefficients of hydraulic conductivity determined using the current model are labeled as "K from current model" in Table 4.

As an alternative, the authors have also analyzed flow through the same pavement system solving time-independent (steady state) continuity equation and Navier Stokes equations using a finite-difference approach similar to the pressure correction method in the SIMPLE (Semi Implicit Method for Pressure-Linked Equations) algorithm [11]. For the purpose of comparing the solutions obtained from the current model for the special case of steady state flow, the "K" value was also computed from steady state flow analysis in Chapter 2. In Table 4, these values are labeled as "K from steady flow model using SIMPLE algorithm".

It can be concluded from Table 4 that the coefficients of hydraulic conductivities determined from the current model agree fairly well with those computed from common empirical relationships. It also agrees with the "K" values predicted from a separate numerical model which the authors have developed based on the SIMPLE algorithm in Chapter 2 to solve just the steady fluid flow problems. Furthermore, it was determined that the coefficients of hydraulic conductivity for gravel and coarse sand used in the

Numerical Illustration (Section 3.4) are 0.097 m/s and 0.043 m/s respectively. These values are within the ranges of typical hydraulic conductivities presented in the literature [16] for the corresponding PSDs shown in Figure 8.

3.4 Numerical Illustration

The numerical model was applied to the pavement layer interface shown in Figure (2a). The material properties and other model parameters shown in Table 1 and 3 were used for this purpose.

3.5 Selection of Time Step

Eqn 41a can be re-written in the matrix form as

$$[A]\{p\} = \{S\} \tag{44}$$

Where $[A]$ will be a banded matrix with elements that are formed from $a_{i,j}$, $b_{i,j}$, $c_{i,j}$, $d_{i,j}$ and $e_{i,j}$ evaluated at nodes where ($p_{i,j}$) are unknown nodal pressures. $\{p\}$ is the vector of unknown pressures. Meanwhile, the $\{S\}$ vector contains $S_{i,j}$ terms evaluated at all the nodes and the known (fixed) nodal pressures ($p_{i,j}$) at boundaries. Extremely small time steps can make the coefficient matrix [A] become ill-conditioned which could result in numerical instability in the solution procedure. On the other hand, if the time step is too large the numerical methods would not provide precise solutions due to truncation errors associated with the difference expression for the time derivative [13]. Hence, an optimum time step of $1e^{-4}$ seconds is used in this paper.

3.6 Results of Numerical Illustration

Figures 28 and 29 respectively illustrate how the pore water pressures and water velocities are developed within the layers in real time upon a sudden pressure build-up at the bottom of the coarse sand-gravel layer system. The transient effects are clearly seen from the isochrones shown in Figures 28 and 29. It is also seen that it takes 2.5e-2 seconds for the steady state flow to establish.

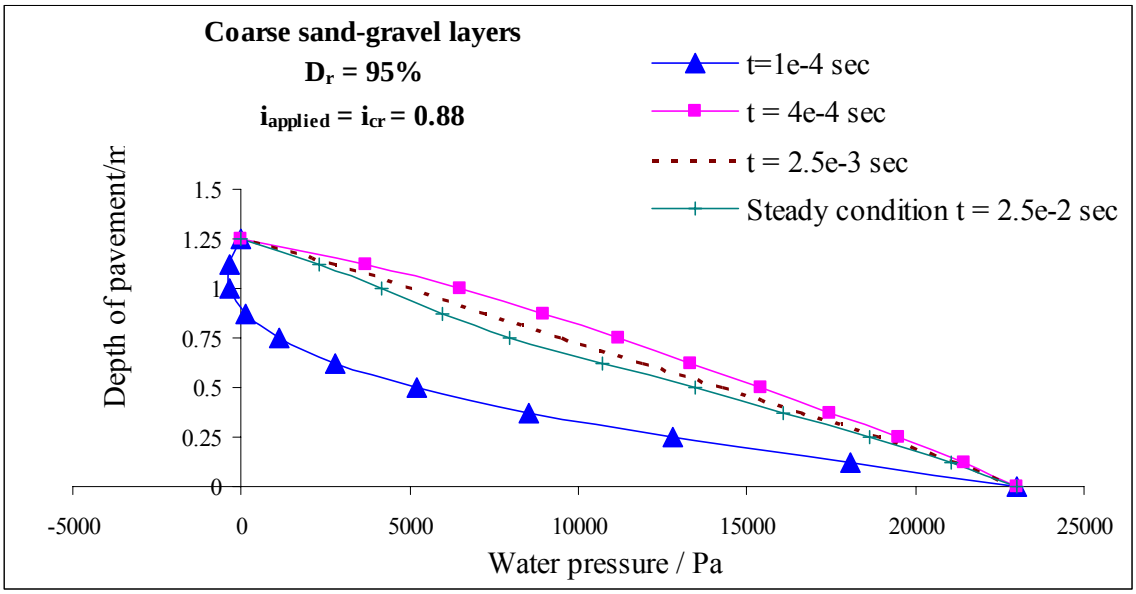

Figure 28: Development of Water Pressure within the Coarse Sand-Gravel Layers with Time (For Pressure Differential of 23 kPa)

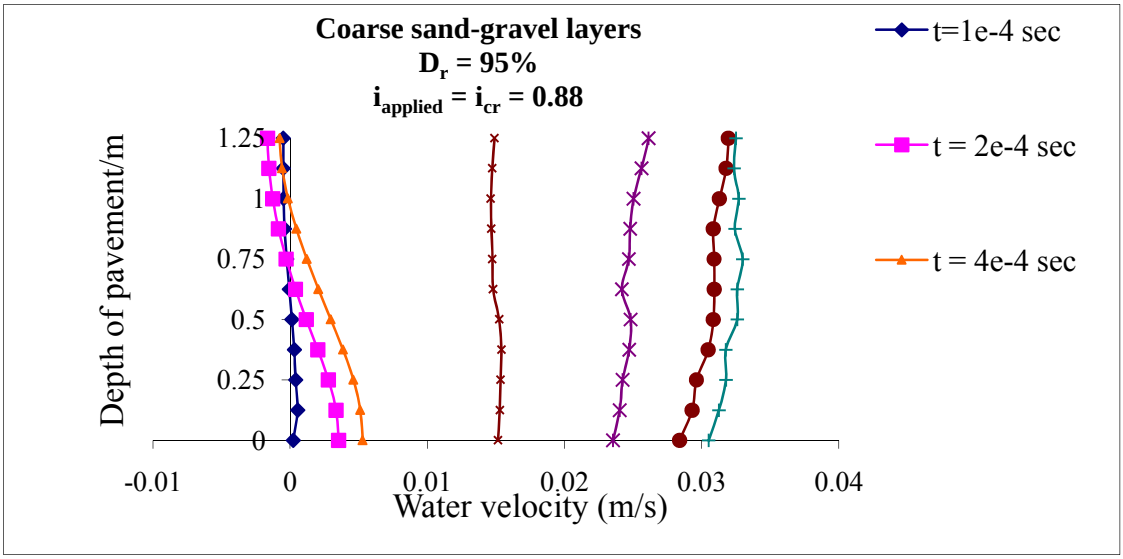

Figure 29: Development of Water Velocity within the Coarse Sand-Gravel Layers with Time (For Pressure Differential of 23 kPa)

Figure 30 illustrates the progression of flow rate with time for different levels of compaction. They clearly reveal the reduction in flow rate due to densification and the impact of compaction on the hydraulic conductivity.

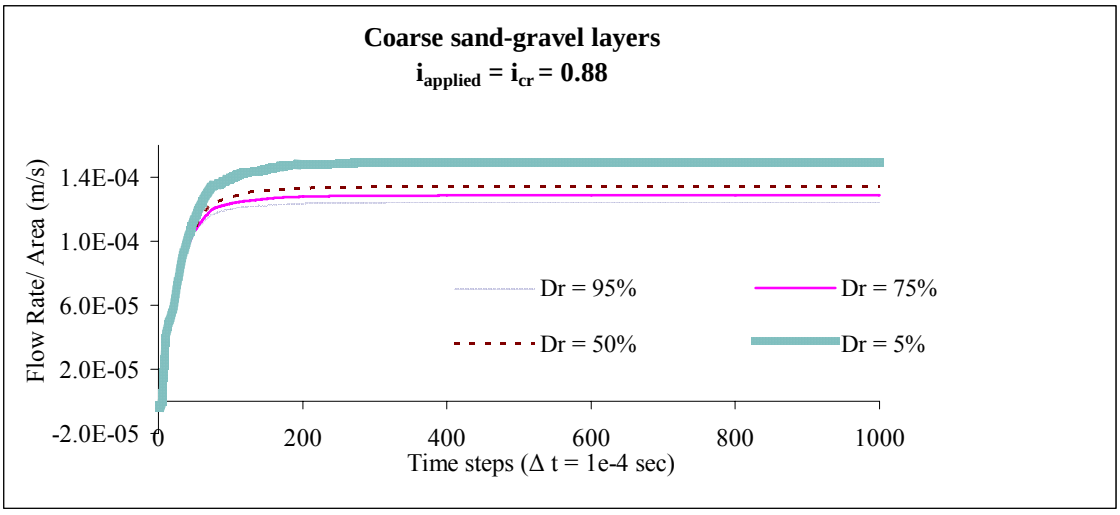

Figure 30a: Plot of Flow Rate through Coarse Sand-Gravel Layers Vs Time Steps with Different Levels of Compaction (For Pressure Differential of 23 kPa)

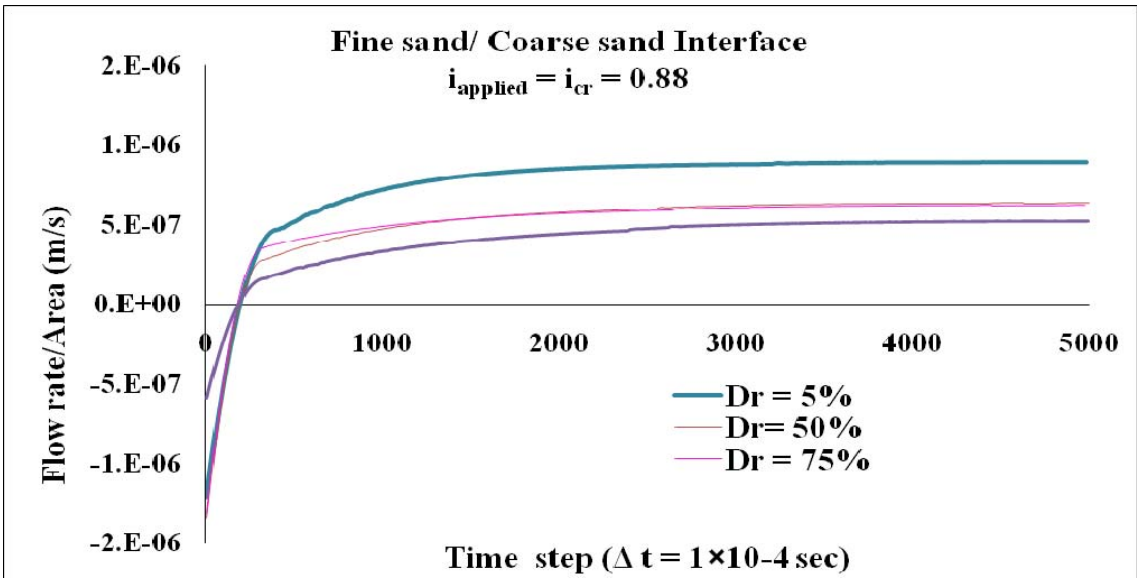

Figure 30b: Plot of Flow Rate through Fine Sand-Coarse Sand Layers Vs Time Steps with Different Levels of Compaction (For Pressure Differential of 23 kPa)

Determination of the localized maximum hydraulic gradients and their locations would be helpful in the design of pavements. Figure 31a was produced to depict the highest value of i_{max}/i_{cr} anywhere within the coarse sand-gravel layer system. During initial time steps, the high i_{max}/i_{cr} appears close to the bottom boundary where a high water pressure of 23 kPa is applied suddenly to initiate flow. This is natural, because in reality, sudden application of high pressure creates instability at the point of application. With time, the magnitude of i_{max}/i_{cr} reduces and the high i_{max}/i_{cr} gradually moves closer to the interface (Figure 31). As illustrated in Figure 31a, when the steady state is reached the spatial maximum hydraulic gradient is nearly equal to the average hydraulic gradient applied across the pavement layers i.e. the critical hydraulic gradient. Moreover, the overall (temporal) maximum hydraulic gradient that occurs after the initial condition effects on

bottom boundary is seen close to the interface during transient condition, varying slightly with the compaction level. From Figure 31b, it can be seen that the impact of compaction on the maximum hydraulic gradient is only marginal even under transient conditions.

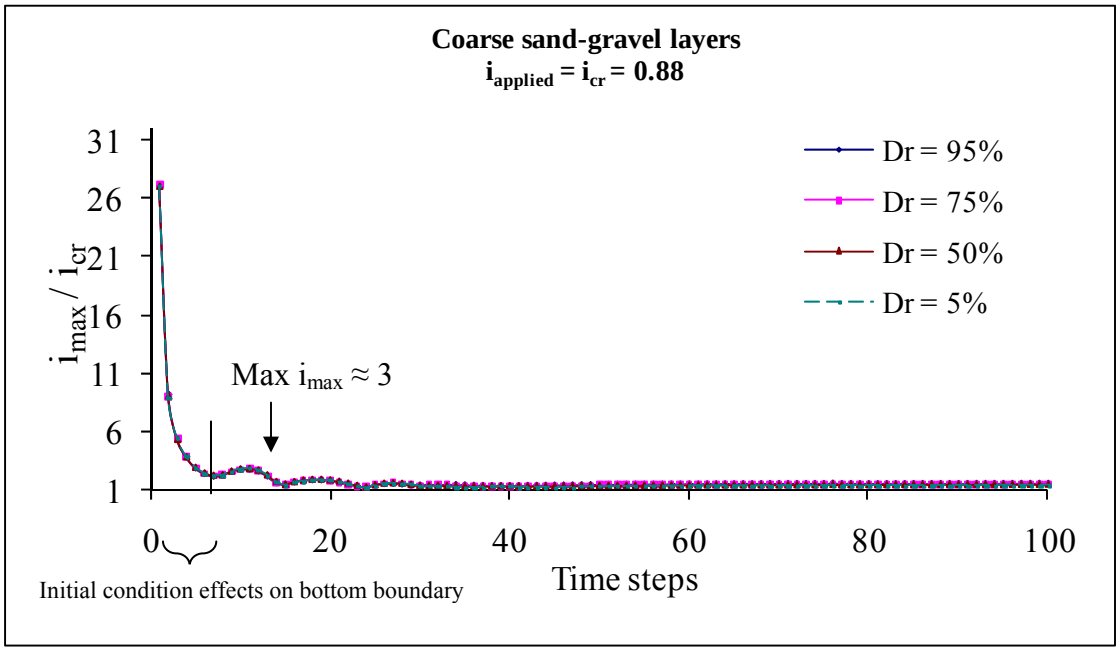

Figure 31a: Plot of Maximum Hydraulic Gradient within the Coarse Sand-Gravel Layers Vs Time Steps for Different Levels of Compaction (For Pressure Differential of 23 kPa)

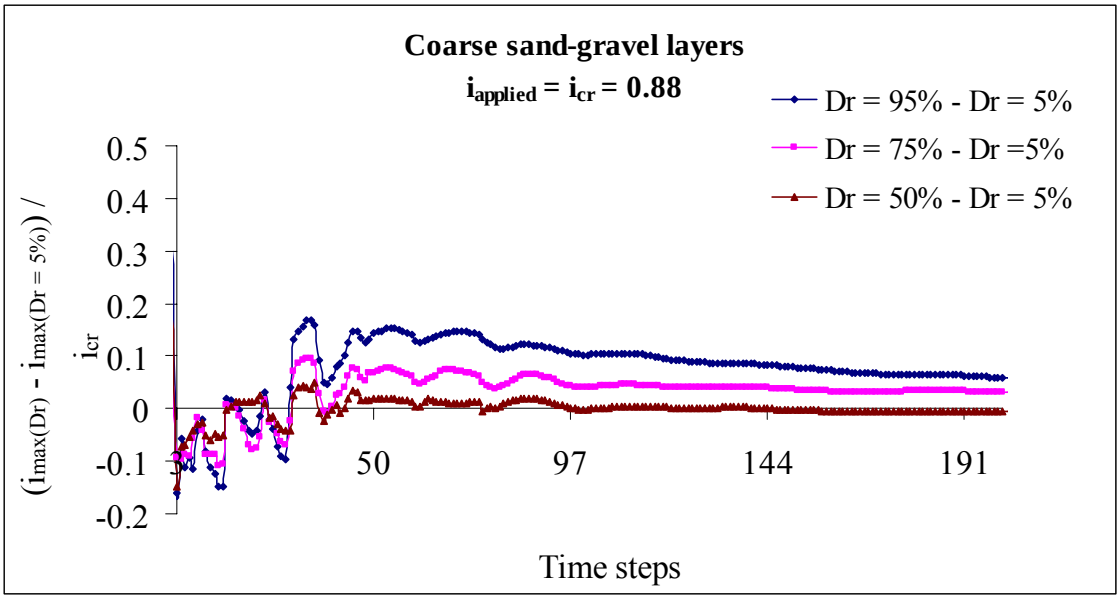

Figure 31b: Plot of Difference in Maximum Hydraulic Gradients Within The Coarse Sand-Gravel Layers Vs Time Steps for Different Levels of Compaction (For Pressure Differential of 23 kPa)

Figure 32 shows that at the steady state the maximum spatial hydraulic gradients occur at the interface. First, the localized hydraulic gradient is computed at each grid from the water pressures, velocities and its elevation using Eqn 34. At any depth in the pavement system, the average localized hydraulic gradient is determined by averaging the localized hydraulic gradient of the individual grid elements in each row along the pavement width. Figure 32 shows that the localized hydraulic gradients also clearly exceed the values predicted by the conventional analysis (Darcy's law).

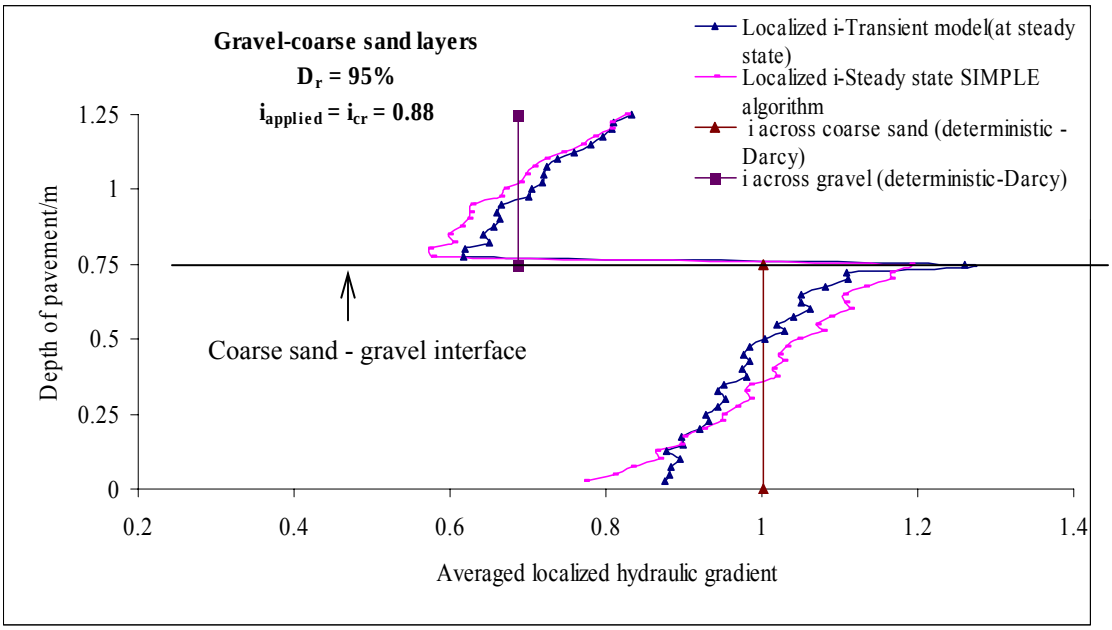

Figure 32: Comparison of Hydraulic Gradients Obtained Using Continuum and Particulate Approaches (Steady State)

As illustrated in Figure 33, when the soil is not uniformly compacted, some localized porosities would be high. In this study, in order to clearly visualize the local effects, the coarse sand/gravel interface is assembled with a local region poorly compacted (D_r = 5%) compared to other regions (D_r = 95%).

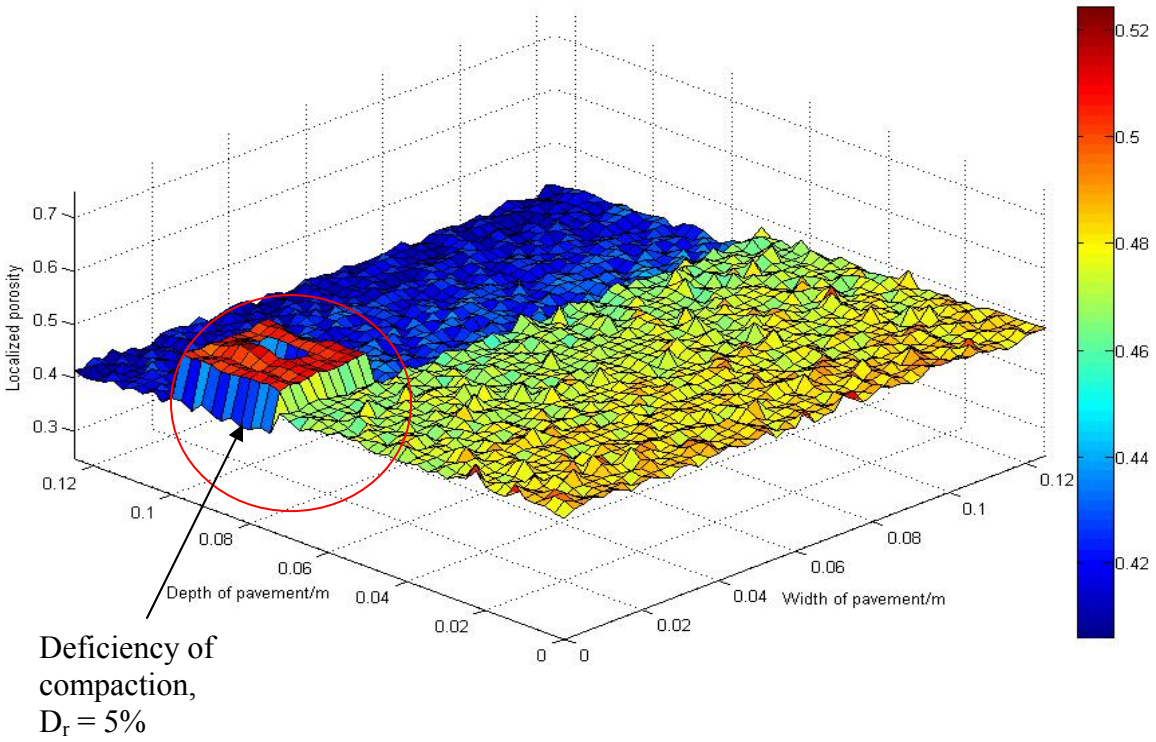

Figure 33: Porosity Distribution for Coarse Sand-Gravel Interface with Non-Uniform Compaction (Circled Area is Packed with D_r of 5% and the Remaining Area is Packed with D_r of 95%)

Figure 34 shows the impact of the localized weak zone on the flow pattern. As illustrated in Figure 35, fluid pressure varies linearly within each layer and shows a sudden change at the interface due to differences in grain size and porosity. On the other hand, a deficiency of compaction makes the fluid pressure distribution non-linear which affects the localized flow quantities. That is, an abrupt pressure change between two adjacent grid elements leads to undesirable higher localized hydraulic gradients as seen in Figure 36. An advantage of this model is that by making the size of the grid elements as small as possible, the desired localized effects can be observed more effectively.

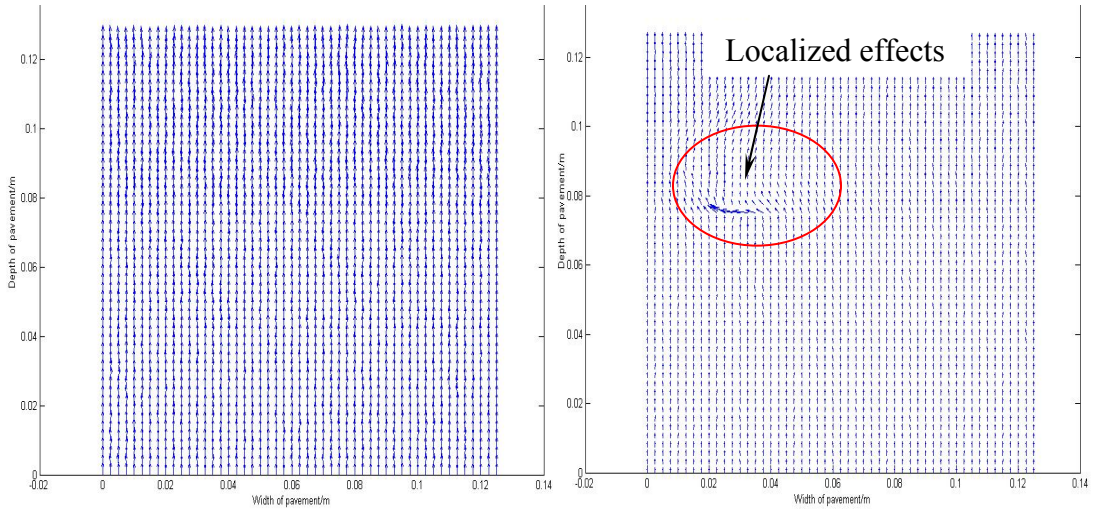

(a) **(b)**

Figure 34: Velocity Vector Plots: (a) Uniformly Compacted Soil Media (D_r = 95%) (b) Deficiency of Compaction in Local Area

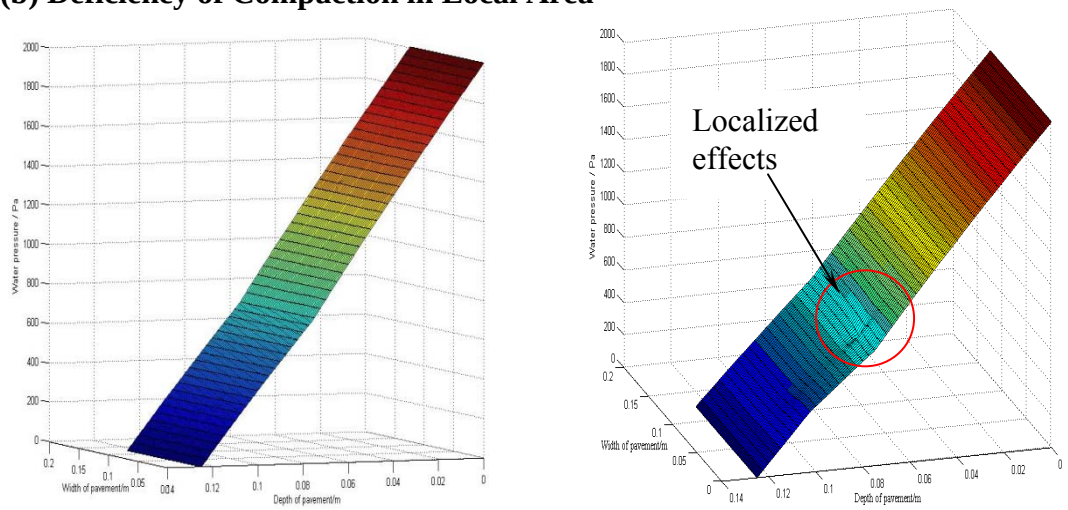

(a) **(b)**

Figure 35: Plot of Fluid Pressure Distribution across the Coarse Sand-Gravel Interface: (a) Uniformly Compacted Coarse Sand-Gravel Interface ((D_r = 95%) (b) Deficiency of Compaction in Local Area

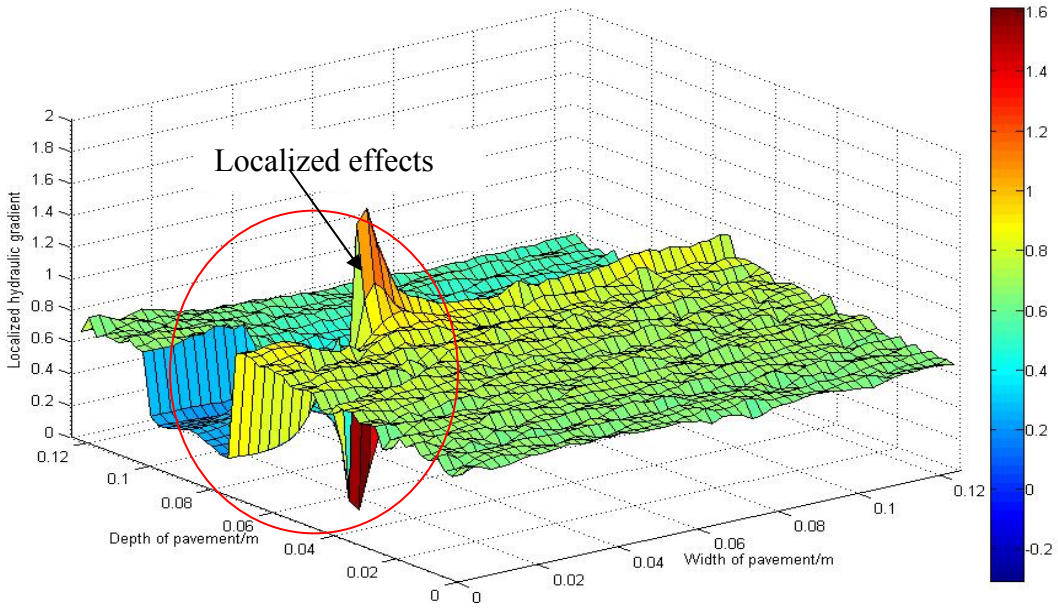

Figure 36: Plot of Localized Hydraulic Gradients for Coarse Sand-Gravel Interface with Weak Region

3.7 Limitations of the Model

In this simplified particulate model, the fluid phase is partially coupled with the solid phase only in terms of the volumetric compatibility. Therefore, the intricate dynamics of individual soil particle interactions with water, which would not impact the flow characteristics significantly, are not taken into account. Also, the soil particles are assumed to be perfect spheres neglecting the angularity and roughness. One realizes that the angularity of soil particles could widen the ranges of both the maximum and minimum void ratio and hence that of the natural void ratio. Because of the probability of having relatively larger changes in void ratio of adjacent grid elements due to angularity, excessive localized hydraulic gradients of larger magnitude could result. This issue could be addressed partly, by incorporating the compression indices (Eqn 43) modified for subrounded, subangular and angular particles as detailed in [18]. Furthermore, in this

model, the three dimensional porosities obtained from particle packing are coupled with the flow constrained in the third direction due to the assumed two dimensional nature of the pavement system. The above 2D assumption seems to be reasonable because the predicted hydraulic conductivities do not deviate much from those determined using widely used empirical equations. To compute the change in porosity in the transient continuity equation, the water pressure difference during the previous time step [(N-1) $\longrightarrow$ N] was used in Eqn 16 to make the numerical scheme explicit. When the time step is adequately small, this limitation would not affect the solution since the variation in water pressure within small time duration can be considered linear and hence equal for all equal time steps.

3.8 Conclusions

In this study, water seepage in a couple of two-layer filter interface with different levels of compaction was analyzed using a soil particulate model with Navier Stokes flow principles. The particulate effects of soil with different levels of compaction were conveniently incorporated in the model using a random packing technique, while the flow of water within the particulate assembly was modeled by the Navier Stokes equations. Compaction effects were incorporated in the model using the concept of relative density. Two separate two-layer interfaces, i.e. coarse sand/gravel and fine sand/coarse sand were assembled using particle size distributions that satisfied the conventional filter design criteria. Then, a pressure differential that corresponded to the critical hydraulic gradient was applied across the layer interface. The relative density certainly impacts the flow rate

but has an insignificant effect on the localized hydraulic gradients. Furthermore, the localized hydraulic gradients determined using the particulate approach differed widely from their average values across the entire layer highlighting the importance of considering localized effects in formulating more applicable design criteria. The preliminary results obtained from this model illustrate the advantage of the particulate approach in predicting the critical conditions for erosion, piping and clogging, especially in transient flow conditions, well before the filter fails to function. Extended and more extensive research in this direction is expected to provide deeper insight into more accurate filter design criteria.

CHAPTER FOUR

TRANSIENT SEEPAGE MODEL FOR PARTLY SATURATED AND SATURATED SOILS USING THE PARTICULATE APPROACH

4.1 Introduction

Functionality of earthen structures such as dams, levees, retention ponds and pavements is determined by one dominant factor; the nature of interaction of soil particles with water flow. Hence accurate analysis of water seepage through soils is essential to achieve more economic designs of such structures. The majority of currently available design criteria are formulated based on either empiricism or the analysis of steady state laminar flow through saturated soil continua. However, very often, field observations are also used to refine or calibrate the design criteria. In the conventional models, the dynamic flow of water through soil pores is commonly idealized using the Darcy's law. Experimental studies show that Darcy's law would not be applicable to model transient conditions and high fluid velocities that develop under excessive hydraulic gradients and unsaturated soils [1]. It is also known that it is the transient flow caused by abrupt fluctuations in groundwater conditions plays a more crucial role in determining the durability of pavement structures. Furthermore, hydraulic infrastructures like retention ponds almost always operate under transient flow conditions. Hence, one has to replace the conventional method of analysis based on a steady state continuum to an alternative

approach with a discrete soil skeleton with the ability to incorporate transient effects which includes pre-saturation flow that generally precede the eventual steady state flow. In this study, the author develops a finite-difference model that uses the Soil-Water Characteristic Curves concepts [19] and the Navier Stoke equations for analyzing transient fluid flow through partly saturated and saturated soils. Then, the model is applied to two specific problems:

1) Confined flow occurring in a partly saturated pavement layer during sudden rise of the groundwater table and
2) Transient seepage from retention pond into surrounding granular soil medium.

In the first case, the results show how saturation achieves following the water porosity Vs water pressure trend defined by SWCC. In the second case, the model is able to predict the gradual reduction in the water level of the retention pond including the location of the free-surface.

4.2 Existing Particulate Models

In the conventional seepage models, the flow of water through saturated soil pores is idealized using the Darcy's law based on a continuum approach. In the above approach, a single representative value of hydraulic conductivity determined from field tests or laboratory tests is used to model the entire soil domain. Alternatively, if seepage through soils is analyzed using the particulate approach then one can certainly account for the spatial variation of hydraulic conductivity more accurately by incorporating drag forces acting between soil particles and water in the Navier Stokes equations. Moreover, when

using the particulate approach, the effects of intricate particle dynamics on the water flow can also be considered whenever needed. However, modeling of seepage through particulate media by considering soil-water interaction is relatively new to computational geomechanics. The discrete element method (DEM) does provide an effective tool to model granular soils in particular based on micro mechanical idealizations. El Shamy et al. [4] presented a computational micro-mechanical model for coupled analysis of pore water flow and deformation of saturated granular assemblies. Shimizu's [6] particle-fluid coupling scheme with a mixed Lagrangian-Eulerian approach which enables simulation of coupling problems with large Reynolds numbers is implemented in PFC 2D and PFC 3D released by Itasca Consulting Group, Inc. [7]. The models used by El Shamy et al. and Shimizu are both based on the work by Anderson and Jackson [8] and Tsuji et al. [9]. Anderson and Jackson [8] modeled pore fluid motion through saturated soil mass using averaged Navier Stokes equations. Tsuji et al. [9] simulated the process of particle mixing of a two-dimensional gas-fluidized bed using averaged Navier Stokes equations for comparison with experiments. For all the above cited studies, granular assemblies are modeled using the discrete element model developed by Cundall and Strack [10] and the averaged Navier Stokes equations are discretized using a finite volume technique on a staggered grid [11].

4.3 Flow in Partly Saturated Soils

Although partly saturated subsurface soils are common in most building sites, the concepts of partly saturated soil mechanics are rarely introduced in geotechnical designs.

Furthermore, most geotechnical engineering problems are dealt with assuming positive pore water pressures when suction can occur even in saturated soils. The solutions of many practical problems involving partly saturated soils require an understanding of the hydraulics, mechanics and interfacial physics of partially saturated soils [20]. Slope stability analysis that also incorporates unsaturated soil mechanics would provide more accurate results in most cases. However, water flow in partly saturated soils is, in general, complicated and difficult to describe quantitatively, since it often entails changes in the state and content of soil water.

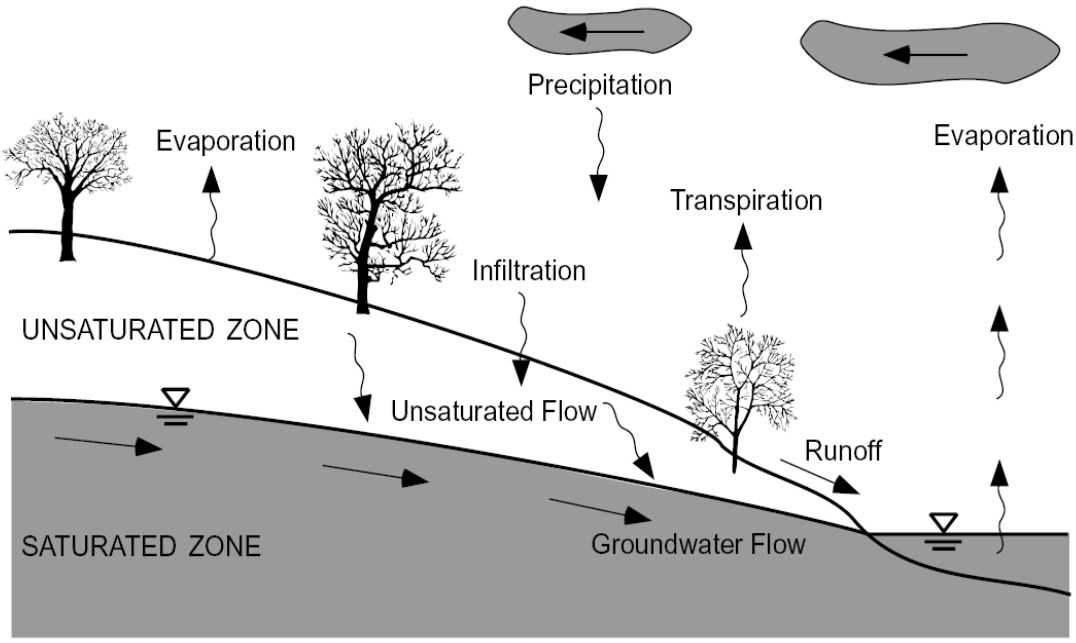

Figure 37: Schematic Diagram to Show the Movement Cycle of Water from Atmosphere to the Groundwater Table [20]

Figure 37 is the schematic representation of the water movement cycle between the atmosphere to the groundwater table. Below the water table, soil is generally saturated with positive pore-water pressures. Immediately above the water table is the capillary

fringe where the degree of saturation approaches 100 percent with negative pore water pressures (suction). In partly saturated soils, the two phases of air and water coexist in the inter-connected pore channels. In order to analyze seepage through saturated-unsaturated soils under transient conditions, Fredlund and Morgenstern [21] proposed Eqn 45a using the constitutive equations relating the volumetric strain in a soil due to total stress and pore water pressure changes.

$$\frac{\partial}{\partial x}\left(k_x \frac{\partial h}{\partial x}\right)+\frac{\partial}{\partial y}\left(k_y \frac{\partial h}{\partial y}\right) = -m_1^w \frac{\partial(\sigma - u_a)}{\partial t}+m_2^w \frac{\partial(u_w - u_a)}{\partial t} \tag{45a}$$

$$\sigma = \frac{1}{3}(\sigma_x + \sigma_y + \sigma_z). \tag{45b}$$

Where, h - total hydraulic head ,σ – mean normal stress ,u_a – pore-air pressure, u_w – pore-water pressure, $(u_a - u_w)$ – matric suction, k_x and k_y - x and y directional hydraulic conductivities, m_1^w and m_2^w are the corresponding partial compressibilities due to $(\sigma - u_a)$ and $(u_w - u_a)$ respectively.

Darcy's law is also applicable to flow through partly saturated soils with the use of variable hydraulic conductivities with respect to suction as shown later in Section 3.2. In saturated soils, any minor changes in the hydraulic conductivity due to changes in porosity are neglected whereas in unsaturated soils, hydraulic conductivity is significantly affected by combined changes in the void ratio and the degree of saturation (or water content) of the soil.

From a geotechnical engineering point of view, it is the flow in the water phase of the unsaturated zone that is of practical interest. Therefore, the flow through unsaturated soils can be simplified assuming that the air phase is continuous throughout the soil matrix

with a pressure equal to that of the atmosphere. Using the "single- phase" flow approach which is accurate enough for many practical purposes, an unsaturated flow model was developed by Lam et al. [22]. If no external loads are applied on the soil mass during water flow ($\frac{\partial \sigma}{\partial t} = 0$) and if the air phase is continuous and open to the atmosphere (u_a = 0), Eqn 45a can be simplified to Eqn 45c.

$$\frac{\partial}{\partial x}\left(k_x \frac{\partial h}{\partial x}\right)+\frac{\partial}{\partial y}\left(k_y \frac{\partial h}{\partial y}\right) = m_2^w \frac{\partial u_w}{\partial t} \quad (45c)$$

Ng and Shi [3] also used Eqn 48c to numerically investigate the stability of unsaturated soil slopes subjected to transient seepage. In Ng and Shi's [3] work, a finite element model was used to investigate the influence of various rainfall events and initial ground water conditions during transient seepage. However, slope stability was analyzed without considering the *localized zones* of high pressure build-up and high hydraulic gradients within the slope.

4.4 Overview of the New Model

The model presented in this paper first uses a newly-developed packing algorithm to randomly pack a three dimensional discrete soil skeleton resembling a natural soil deposit that exists at a given relative density or particle size distribution. Then the model is used to determine the water flow behavior in a particulate saturated – partly saturated soil medium. The seepage of water through the particulate medium is modeled using the Navier Stokes (NS) equations which are discretized using the finite difference method (FDM) [13]. The new model is capable of predicting both transient and steady state flow

effects under both saturated and partly saturated conditions. First, the model is applied to simulate flow in a single layer of granular soil resulting from of a sudden surge of groundwater. Second, the model is applied to simulate flow around a retention pond built in granular soil. The comprehensive analytical procedure and the computer code developed for its implementation are illustrated in Figure 38. The analytical procedure consists of two primary tasks such as the random assembly of the particulate medium (granular soil) and the solution of the fluid flow governing equations. The flow chart also includes the section, equation and figure numbers corresponding to each stage.

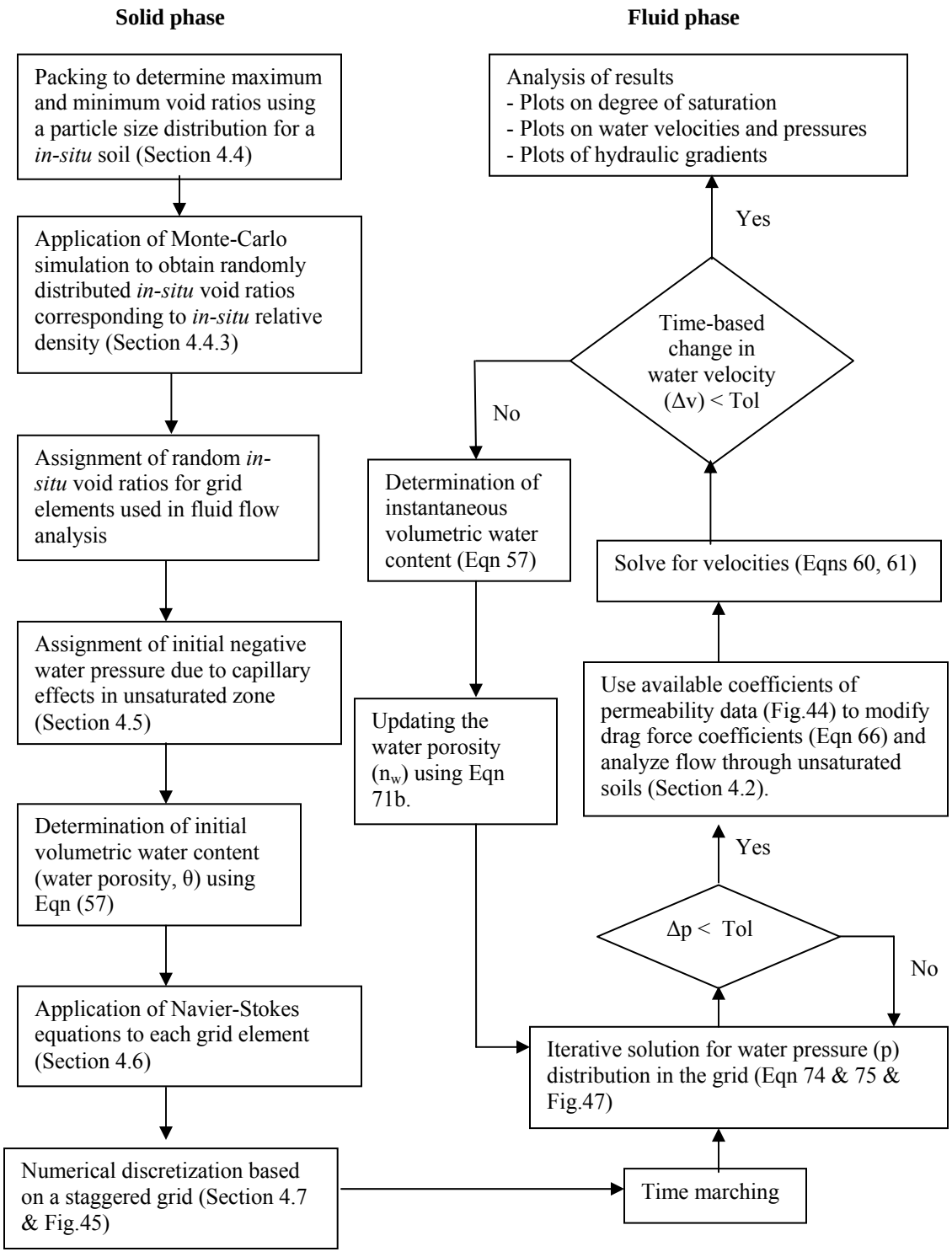

Figure 38: Flow Chart Illustrating the Analytical Model for Flow through Unsaturated Soils

4.5 Modeling of Soil Structure (3D Random Packing of Soil Particles)

Fine sand represented by the Particle Size Distribution (PSD) curve in Figure 39 is used in this study.

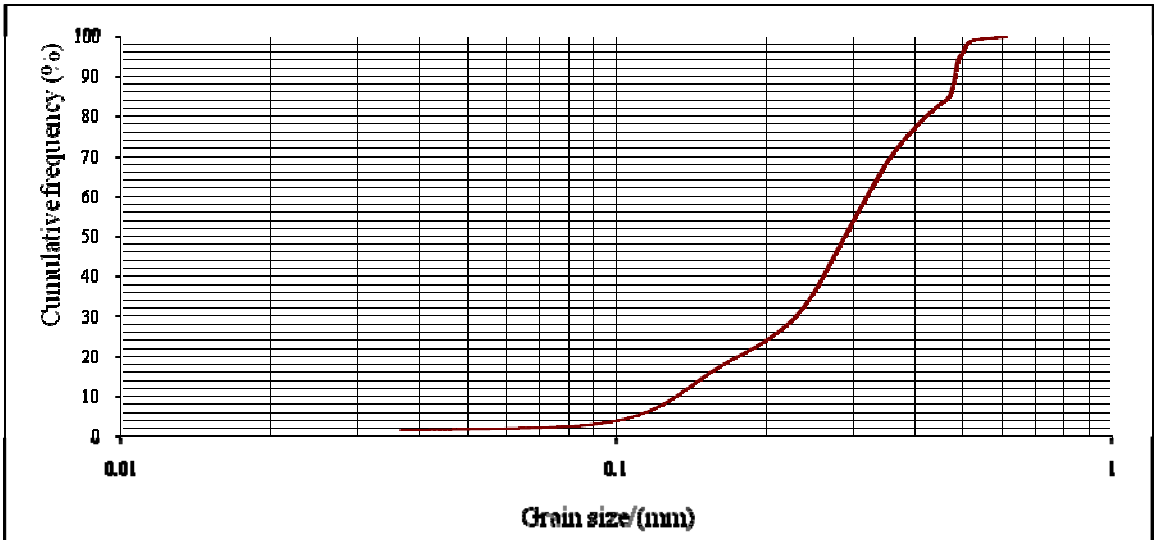

Figure 39: Particle Size Distribution for Fine Sand

4.5.1 Simulation of Maximum and Minimum Void Ratios Using PSD

In this model the soil particles are assumed to be of spherical shape. To determine the maximum and minimum void ratios (e_{max} and e_{min}) corresponding to fine sand in Figure 39, a customized random packing algorithm was developed. Using this algorithm, 3 mm × 3 mm × 3 mm cubes (Figure 40a) were packed using soil particles picked from the PSD in Figure 39. It must be noted that the PSD in Figure 43 is in fact the cumulative probability distribution of the fine sand particles. Therefore, by using an adequately large array of random numbers from a uniform distribution ranging from 0 and 100 (the y axis range in Figure 39), one can select the corresponding array of particle diameters that

conforms to the selected PSD, from the x axis. This technique, known as the Monte-Carlo simulation [14] is used to select the array of packing diameters for each cube (Figure 40a). It is noted that the resulting maximum and minimum void ratio distributions change in each packing trial since the order of diameters used for packing is changed randomly. An adequate number of particles must be within the cube to determine the representative e_{max} and e_{min} for the fine sand.

4.5.2 Implementation of the Packing Procedure

In order to obtain the loosest state of fine sand (e_{max}) within the cubes described above, different sizes of soil particles inscribed in boxes are packed as indicated in Figure 40a using a MATLAB code developed by the authors. The side length of each box is the same as the diameter of the inscribed soil particle. Based on the minimum particle diameter of fine sand (0.04 mm), the side length of each cube is divided into a finite number of sub-divisions (Figure 40a). Then, the packing algorithm tracks the total number of sub-divisions occupied by each incoming box, i.e. each packed soil particle, as packing proceeds based on the Monte-Carlo simulation corresponding to a given PSD (Figure 39). Finally, the automated algorithm fills all sub-divisions until it finds that not a single sub-division is available within the considered cube for further packing of soil particles from the given PSD. As packing of each cube approaches completion, the void ratio reaches a constant value of 0.9098 which can be identified as the maximum void ratio for simple cubical packing [15].

On the other hand, in order to obtain the minimum void ratio (densest packing), the maximum number of spheres smaller than the inscribing sphere in each box is also packed into the unoccupied space at the corners of each box (Figure 40c and 40d) before that box is placed in the cube (Figure 40b). 50 such cubes (trials) were packed randomly using the Monte-Carlo simulation. Since the minimum void ratio obtained in each trial would be different depending on how the unoccupied space in each box filled, it can be considered as random variable. The range derived for e_{min} as shown in Table 5 agrees with the typical values in [15].

Table 5: Soil Characteristics

Soil type	Fine sand
Sizes of particle (mm) (Figure 39)	0.04 – 0.62
D_{15} (mm) (Figure 39)	0.16
D_{50} (mm) (Figure 39)	0.29
D_{85} (mm) (Figure 39)	0.49
e_{max} (Packing)	0.9098
e_{min} (Packing)	0.54 – 0.79
Mean of e_{min}	0.48
Standard deviation of e_{min}	0.0037

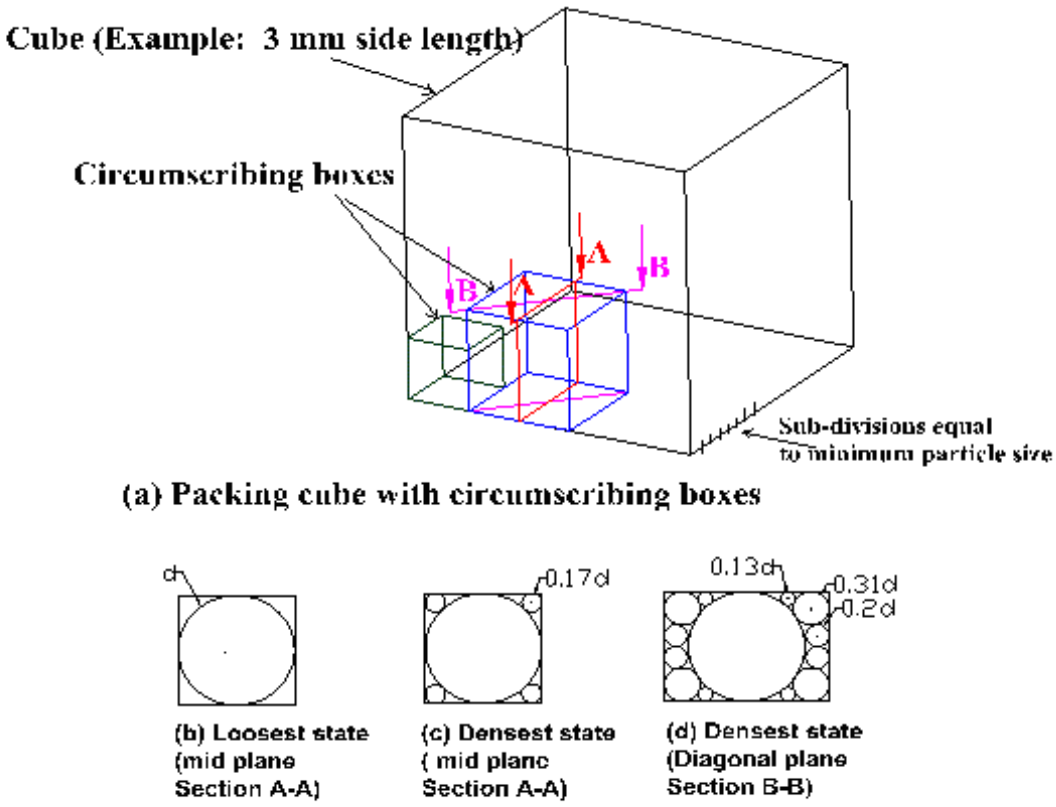

Figure 40: Packing Procedure

4.5.3 Determination of the Natural Void Ratio Distribution

The property of relative density is helpful in quantifying the level of compaction of coarse-grained soils. The relative density of a coarse-grained soil expresses the ratio of the reduction in the voids in the current state, to the maximum possible reduction in the voids (Eqn 2). The *in-situ* void ratio distribution (e) corresponding to a given relative density (D_r) is obtained using the previously obtained e_{max} and e_{min} (Eqns 46 or 47).

$$D_r = \frac{e_{max} - e}{e_{max} - e_{min}} \tag{46}$$

or

$$e = D_r\ e_{\min} + e_{\max}\ (1 - D_r) \tag{47}$$

Where, e_{max} is the void ratio of fine sand in its loosest state (= 0.9098). e_{min} is the randomly distributed void ratio of fine sand in its densest state. e is the randomly distributed void ratio of sand in its natural state in the field.

For a relative density of 50%, Eqn 51 reduces to

$$e = 0.5\ e_{\min} + 0.45 \tag{48}$$

The mean ($\bar{e}$) and the standard deviation (S_e) of natural void ratios are determined from Eqns 49 and 50

$$\bar{e} = D_r\ \overline{e_{\min}} + 0.9098\,(1 - D_r) \tag{49}$$

$$S_e = D_r\ S_{e\min} \tag{50}$$

Where, $\overline{e_{\min}}$ (Eqn 51a) and $S_{e\,min}$ (Eqn 51b) are the mean and standard deviation of the minimum void ratio (Table 5) obtained from the packing procedure described in Section 4.4.

$$\overline{e_{\min}} = \frac{1}{50}\sum_{i}^{50}(e_{\min})_i \tag{51a}$$

$$S_{e\min} = \sqrt{\frac{1}{50}\sum_{i}^{50}\left((e_{\min})_i - \overline{e_{\min}}\right)^2} \tag{51b}$$

Knowing the mean and standard deviation of the natural void ratio (Eqns 49 and 50) and assuming a normally distributed probability density function for the natural void ratio (e), its cumulative distribution (Figure 41) is obtained using Eqn 52.

$$e = \bar{e} + S_e\ Z^* \tag{52a}$$

Cumulative frequency, $\Psi\left(Z^*\right) = P\left(Z \langle Z^*\right)$ (52b)

Where, Z^* is the standard normal variate corresponding to a cumulative probability of $\Psi\left(Z^*\right)$ in the standard normal distribution (Z). The cumulative distribution of natural void ratios corresponding to a D_r of 50% is shown in Figure 41.

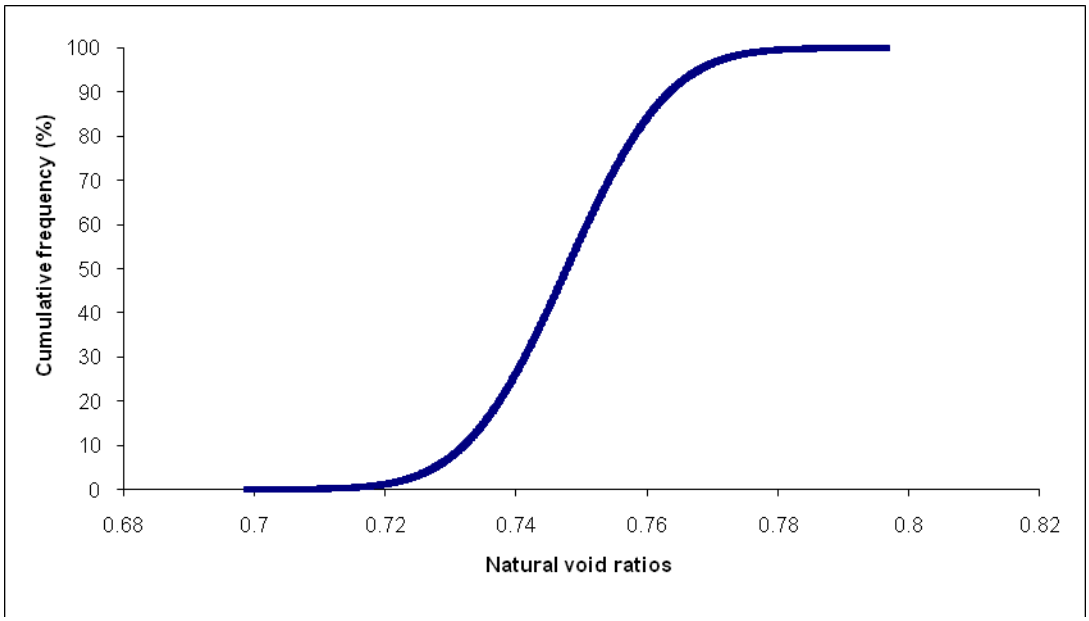

Figure 41: Cumulative Distribution for Natural Void Ratios for the Fine Sand with D_r = 50%

Then, once more the Monte-Carlo simulation can be used to pick an array of natural void ratios for fine sand using Figure 39. Since the NS equations are written in terms of porosities (Section 4.6), the spatial probability distribution of natural void ratios is first converted to porosities using Eqn 53.

$$n = \frac{e}{1+e} \quad (53)$$

The spatial distributions of natural void ratios (porosities) so obtained assumed to be representative of the fine sand will be used in the seepage analysis model presented in Section 4.6.

4.6 Modeling of Fluid Flow in Partially Saturated Soils

When the developed model is applied to a partially saturated granular soil layer, the initial water pressures within the saturated and unsaturated zones are assumed to be due to hydrostatic pressure and the capillary suction effects respectively, as shown in Figure 42.

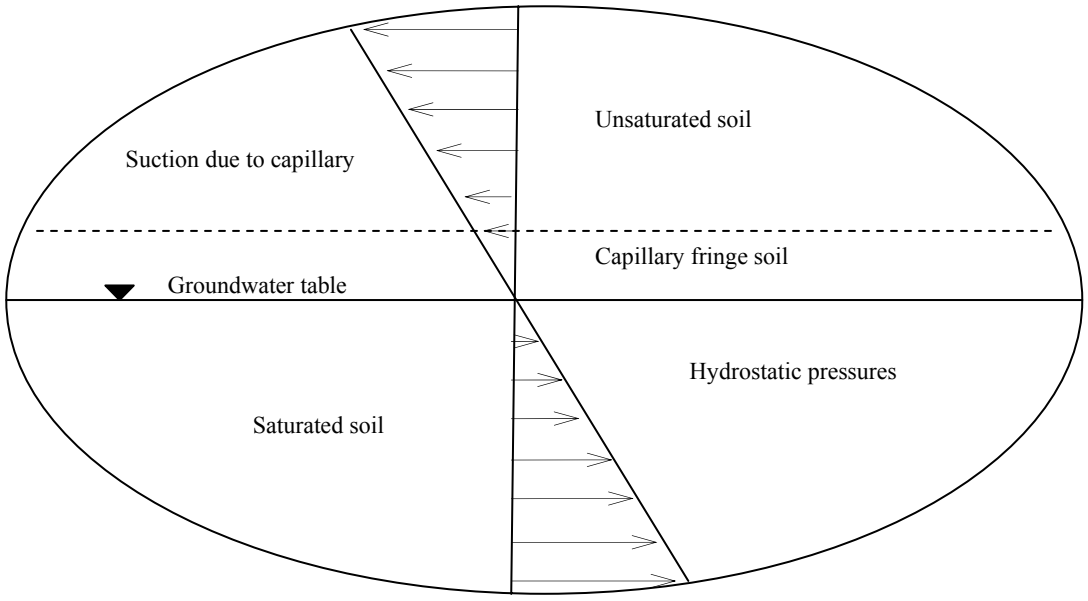

Figure 42: Initialization of Water Pressure in the Saturated and Unsaturated Zones

4.6.1 Soil Water Characteristic Curve/Water Moisture Retention Curve

The Soil Water Characteristic Curve (SWCC) [17] depicts the relationship between soil water content (θ) and soil water pressure potential (suction, Ψ). The soil parameters defining a typical Soil Water Characteristic Curve are shown in Figure 43a while the Soil Water Characteristic Curves for different particle size distributions are presented in Figure 43b. From Figure 43b, it is seen that sands and gravels lose water quite readily upon suction induced drainage while loams and clays lose much less water upon drainage. There are a number of empirical equations proposed to best-fit the Soil Water Characteristic Curves [19] using the soil parameters shown in Figure 43a. In this model, Eqn 54a –Eqn 54c are used to determine the volumetric water content (θ) for a particular suction (Ψ).

Volumetric water content, $\theta = \frac{V_w}{V}$ (54a)

Where, V is the total volume of a soil sample and V_w is the volume of water in that sample.

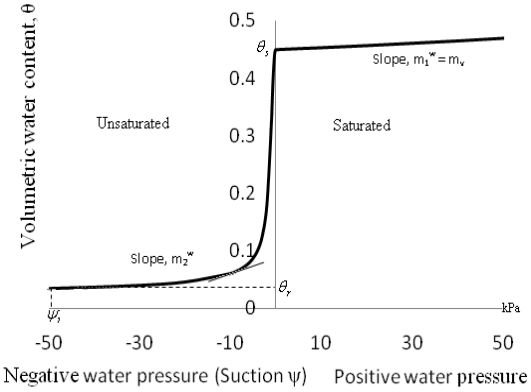

Figure 43a: Typical Soil Water Characteristic Curve and m_2^w for a Saturated -Unsaturated Soil [10]

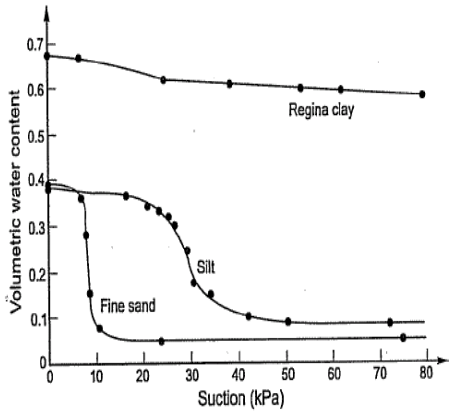

Figure 43b: Soil Water Characteristic Curve for Specific Soil Types [23]

$$\theta(\psi, a, n, m) = C(\psi)\frac{\theta_s}{\left\{\ln\left[e + \left(\frac{\psi}{a}\right)^n\right]\right\}^m} \tag{54b}$$

Where, C(Ψ) is a correction function defined as:

$$C(\psi) = \frac{-\ln\left(1 + \psi/\psi_r\right)}{\ln\left[1 + \left(10^6/\psi_r\right)\right]} + 1 \tag{54c}$$

Where, e = 2.71828; Ψ_r is the suction corresponding to the residual water content, θ_r. θ_s is the (saturated) volumetric water content at zero pressure and a, m, and n are fitting parameters. In this model, θ_s in each grid element is set to the porosity of that element obtained from initial packing (Section 4.4). In the particulate approach, although the θ_s varies with the spatial distribution of porosity, the average θ_s corresponding to 50% of degree of compaction is used in this study for simplicity. The parameters for Eqn 54b – Eqn 54c relevant to the fine sand modeled in the current study are shown in Table 6.

Table 6: Parameters Used to Define the SWCC for Sand [23]

ψ_r	50 kPa
Average θ_s	0.45
a	1.948 kPa
m	2.708
n	1.084

In Section 4.6, θ will also used as the water porosity in formulating the continuity equation and Navier Stokes equations for partly saturated soils. Furthermore, using fundamental soil mechanics, the degree of saturation can be shown that

$$S = \frac{\theta}{n} \tag{55}$$

Where, S- degree of saturation, n – total porosity of the soil.

4.6.2 Determination of the Unsaturated Permeability Function

The hydraulic conductivity is commonly referred to as the coefficient of permeability in geotechnical engineering. In unsaturated soils, the coefficient of permeability is primarily determined by the pore-size distribution and the degree of saturation. The permeability functions for unsaturated soils are used to represent the relationship between the coefficient of permeability and soil suction. Figure 44 illustrates the variation of the coefficient of permeability with suction for different types of soils. There are several empirical equations and statistical models used to determine the permeability functions [19]. One such approach uses the Soil Water Characteristic Curve (Figure 43a) to predict the permeability function [19].

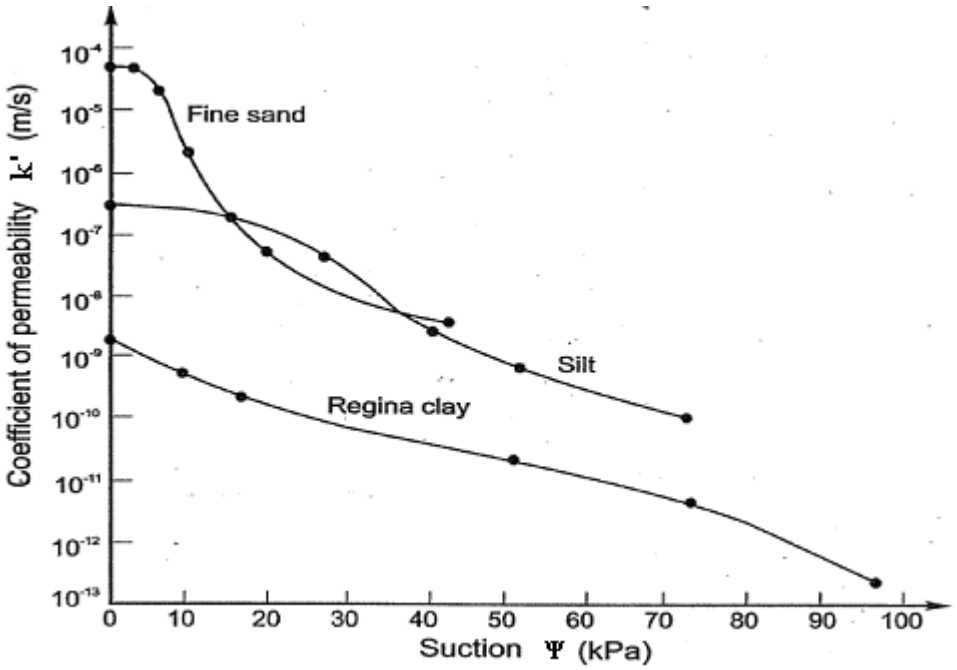

Figure 44: Unsaturated Permeability Function for Selected Soil Types [23]

The flow model presented in this paper does not directly involve the use of the coefficient of permeability. Alternatively, in this model the authors use an appropriate plot from Figure 44 to modify the drag forces in the Navier Stokes equations to account for the variation of the permeability of unsaturated soils with suction.

4.7 Development of the Analytical Model

4.7.1 Navier Stokes Equations

Since the flow model presented in this paper is two-dimensional, the three dimensional porosities obtained from particle packing are coupled with two dimensional water flow. In this study, it is also assumed that the water paths through the pore channels are

continuous for partly saturated soils near saturation. Hence, Navier Stokes equations can be written as follows in a generalized form in terms of the water porosity, θ (= Sn) expressed by Eqn 56:

Water mass Conservation (Continuity Equation):

$$\frac{\partial(Sn)}{\partial t} + \frac{\partial(Snu)}{\partial x} + \frac{\partial(Snv)}{\partial y} = 0 \tag{56}$$

Momentum Conservation (Momentum Equations):

X direction:

$$\frac{\partial(Snu)}{\partial t} + \frac{\partial(Snu^2)}{\partial x} + \frac{\partial(Snuv)}{\partial y} = -\frac{Sn}{\rho}\frac{\partial p}{\partial x} + \frac{D_x}{\rho} + \frac{\mu}{\rho}\left(\frac{\partial^2(Snu)}{\partial x^2} + \frac{\partial^2 Snu}{\partial y^2}\right) \tag{57}$$

Y direction:

$$\frac{\partial(Snv)}{\partial t} + \frac{\partial(Snuv)}{\partial x} + \frac{\partial(Snv^2)}{\partial y} = -\frac{Sn}{\rho}\frac{\partial p}{\partial y} + \frac{D_y}{\rho} + \frac{\mu}{\rho}\left(\frac{\partial^2(Snv)}{\partial x^2} + \frac{\partial^2(Snv)}{\partial y^2}\right) + Sn\,g_y \tag{58}$$

Where, n and S – porosity and degree of saturation at the location (x, y) at time t respectively, u, v – fluid velocities in the x and y directions respectively, ρ – fluid density (1000 Kg/m^3), p – fluid pressure, μ - fluid viscosity (10^{-3} Pa.s), g_y - gravitational force per unit mass in the y direction (9.81m/s^2). The following conditions are assumed in the analysis:

1) Under saturated conditions: S = 1 and n varies due to the compressibility of the soil skeleton as described in Section 4.4.
2) Under unsaturated conditions: n is constant and S increases as suction decreases.

4.7.2 Modification of Drag Force for Water Flow through Unsaturated Soils

The authors developed a modified expression for the drag force in unsaturated soils based on the variation of the hydraulic conductivity of unsaturated soils. Averaged water-particle interactions (drag forces) can be quantified using the semi-empirical relationship provided by the standard Ergun equation [6]. Eqn 59 shows the drag force modified by the authors for application to unsaturated soils.

$$D_x = -\left(150 \frac{\mu (1 - S_n)^2}{(S_n)^2 \overline{d_p^2}} u + 1.75 \frac{(1 - S_n)}{(S_n)^2 \overline{d_p}} \rho u^2 \right) f \tag{59}$$

Where, D_x – averaged water-particle interaction force per unit volume of soil, $\overline{d_p}$ - averaged particle diameter. f is the correction factor to account for the space occupied by air that does not introduce a significant drag force. A similar expression for D_y is used for y directional averaged water-particle interactions.

For fully saturated soils, S = 1.0 and f = 1.0 with no air.

Assuming that the flow through soil pores to be primarily laminar flow with low velocities, the non-linear term contributing to the drag force can be neglected resulting in the simplified form of Eqn 6 for unsaturated soils as follows:

$$(D_x)_{US} = -\left(150 \, f \, \frac{\mu (1 - S_n)^2}{(S_n)^2 \overline{d_p^2}} u \right) \tag{60}$$

Similarly, the drag force under saturated conditions for the same porosity and flow can be written as

$$\left(D_x\right)_S = -\left(150 \ \frac{\mu\left(1-n\right)^2}{n^2 \overline{\overline{d_p^2}}} \ u \ \right) \tag{61}$$

Drag forces cause resistance to water flow and hence they can be considered as being inversely proportional to the coefficient of hydraulic conductivity (K) as,

$$\frac{\left(D_x\right)_{US}}{\left(D_x\right)_S} = \frac{K_S}{K_{US}} = f \tag{62}$$

From Eqns 60 and 61, $f = \frac{K_S}{K_{US}} \frac{S^2\left(1-n\right)^2}{\left(1-Sn\right)^2}$ (63)

Where, K_S and K_{US} are the hydraulic conductivities of saturated and unsaturated soils respectively.

4.8 Numerical Solution Technique

A finite-difference scheme is used to discretize the Eqns 56, 57 and 58. This scheme is based on forward difference in time and porosity, and central difference in space with a two-dimensional staggered mesh arrangement [11, 13]. Eqn 64a expresses the x directional momentum equation in the numerical form for the sequential time steps of N and N+1 referring to the notation in Figure 45.

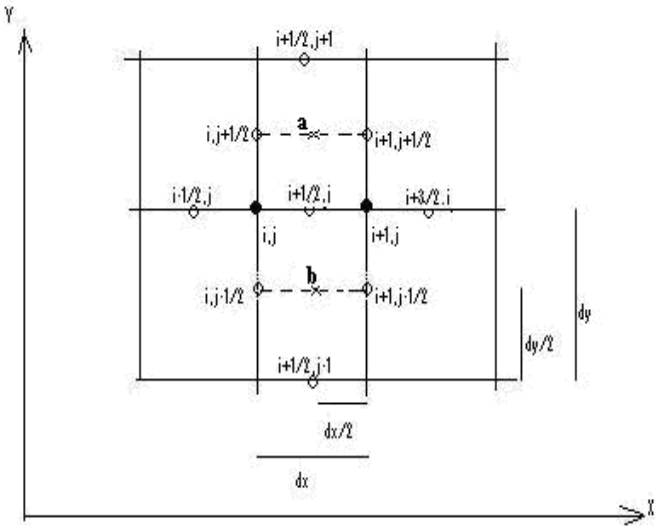

Figure 45: Computational Grid for the X-Momentum Equation

$$\frac{(Sn)_{i+1/2,j}\,u^{N+1}_{i+1/2,j} - (Sn)_{i+1/2,j}\,u^{N}_{i+1/2,j}}{\Delta t} + \frac{(Sn)_{i+3/2,j}\,u^{2}_{i+3/2,j} - (Sn)_{i-1/2,j}\,u^{2}_{i-1/2,j}}{2\Delta x} +$$

$$\frac{(Sn)_{i,j+1}\,u_{i+1/2,j+1}\,\overline{v}_{i+1/2,j+1/2} - (Sn)_{i,j-1}\,u_{i+1/2,j-1}\,\overline{\overline{v}}_{i+1/2,j-1/2}}{2\Delta y} =$$

$$-\frac{(Sn)_{i,j}}{\rho}\left(\frac{p_{i+1,j} - p_{i,j}}{\Delta x}\right) - \left(150 f \frac{\mu\left(1-(Sn)_{i,j}\right)^2}{\rho (Sn)^2_{i,j}\,\overline{d^2_{p_{i,j}}}}\,u_{i-1/2,j}\right)$$

$$+ \frac{\mu}{\rho}\left[\begin{array}{l} \dfrac{(Sn)_{i+1,j}\,u_{i+3/2,j} + (Sn)_{i-1,j}\,u_{i-1/2,j} - 2\,(Sn)_{i,j}\,u_{i+1/2,j}}{(\Delta x)^2} + \\ \dfrac{(Sn)_{i,j+1}\,u_{i+1/2,j+1} + (Sn)_{i,j-1}\,u_{i+1/2,j-1} - 2\,(Sn)_{i,j}\,u_{i+1/2,j}}{(\Delta y)^2} \end{array}\right] \qquad (64a)$$

Where,

$$\overline{v}_{i+1/2,j+1/2} = 1/2\left(v_{i,j+1/2} + v_{i+1,j+1/2}\right) \qquad (64b)$$

$$\overline{\overline{v}}_{i+1/2,j-1/2} = 1/2\left(v_{i,j-1/2} + v_{i+1,j-1/2}\right) \tag{64c}$$

Within the staggered grid, some velocities need to be interpolated as shown in Eqns 64b and 67c.

In a concise form, Eqn 64a can be re-written as

$$(Sn)_{i+1/2,j}\, u^{N+1}_{i+1/2,j} = (Sn)_{i+1/2,j}\, u^{N}_{i+1/2,j} + A^{N}_{i+1/2,j}(\Delta t) + \overline{A}^{\,N}_{i+1/2,j}(\Delta t)\left(\frac{p^{N}_{i+1,j} - p^{N}_{i,j}}{\Delta x}\right) + \overline{\overline{A}}^{\,N}_{i+1/2}(\Delta t) \tag{64d}$$

Where,

$$A_{i+1/2,j} = -\frac{(Sn)_{i+3/2,j}\, u^{2}_{i+3/2,j} - (Sn)_{i-1/2,j}\, u^{2}_{i-1/2,j}}{2\Delta x} + \frac{(Sn)_{i,j+1}\, u_{i+1/2,j+1}\, \overline{v}_{i+1/2,j+1/2} - (Sn)_{i,j-1}\, u_{i+1/2,j-1}\, \overline{\overline{v}}_{i+1/2,j-1/2}}{2\Delta y} \tag{64e}$$

$$\overline{A}_{i+1/2,j} = -\frac{(Sn)_{i+1/2,j}}{\rho} \tag{64f}$$

and

$$\overline{\overline{A}}_{i+1/2,j} = -\left(150\, f\, \frac{\mu(1-(Sn)_{i,j})^2}{\rho (Sn)^2_{i,j}\, \overline{d^2_{p_{i,j}}}}\, u_{i+1/2,j}\right) +$$

$$\frac{\mu}{\rho}\left[\frac{(Sn)_{i+1,j}\, u_{i+3/2,j} + (Sn)_{i-1,j}\, u_{i-1/2,j} - 2(Sn)_{i,j}\, u_{i+1/2,j}}{(\Delta x)^2} + \frac{(Sn)_{i,j+1} u_{i+1/2,j+1} + (Sn)_{i,j-1} u_{i+1/2,j-1} - 2(Sn)_{i,j}\, u_{i+1/2,j}}{(\Delta y)^2}\right] \tag{64g}$$

The numerical form of the y directional momentum equation can be written similarly based on Eqn 58 as Eqn 65.

$$(\mathrm{Sn})_{i,j+1/2}\, v^{N+1}_{i,j+1/2} = (\mathrm{Sn})_{i,j+1/2}\, v^{N}_{i,j+1/2} + B^{N}_{i,j+1/2}(\Delta t) + \bar{B}^{N}_{i,j+1/2}(\Delta t)\left(\frac{p^{N}_{i,j+1} - p^{N}_{i,j}}{\Delta y}\right) + \bar{\bar{B}}^{N}_{i,j+1/2}(\Delta t) + (\mathrm{Sn})_{i,j+1/2}\, g_y(\Delta t) \tag{65}$$

The discretized continuity equation of water is given by Eqn 66. In computing the change in porosity in the transient continuity equation, the numerical scheme is made explicit by using porosity during the previous time step (N-1) in Eqn 66.

$$\left[\frac{(\mathrm{Sn})_{i+1/2,j}\, u^{N+1}_{i+1/2,j} - (\mathrm{Sn})_{i-1/2,j}\, u^{N+1}_{i-1/2,j}}{\Delta x} + \frac{(\mathrm{Sn})_{i,j+1/2}\, v^{N+1}_{i,j+1/2} - (\mathrm{Sn})_{i,j-1/2}\, v^{N+1}_{i,j-1/2}}{\Delta y}\right] = \frac{\Delta(Sn)}{\Delta t} = -\frac{(Sn)^{N}_{i,j} - (Sn)^{N-1}_{i,j}}{\Delta t} \tag{66}$$

Finally, using either Eqn 67a or Eqn 67b, the change in water porosity ($\Delta \mathrm{Sn}$) during a time step, Δt, can be determined and used in the discretized continuity equation (Eqn 66).

In the saturated zone ($p > 0$ and $S = 1$), the change in porosity is determined using Eqn 67a.

$$\frac{\Delta(n)}{\Delta t} = -\left[\frac{0.4343\, C_c (1 - n_{i,j})^2 \left[p^{N}_{i,j} - p^{N-1}_{i,j}\right]}{\sigma^{N}_{i,j} - p^{N}_{i,j}}\right]\frac{1}{\Delta t} \tag{67a}$$

Where, C_c - equivalent compression index of the soil, σ- total vertical stress in soil. Meanwhile, in the partly saturated zone ($p < 0$ and $S < 1$), the Soil-Water Characteristic Curve is used to determine the change in water porosity using Eqn 67b.

$$\frac{\Delta(Sn)}{\Delta t} = -\left(m_2^w\right)_{i,j} \frac{\left[p_{i,j}^{N} - p_{i,j}^{N-1}\right]}{\Delta t} \qquad (67b)$$

The slope of the Soil Water Characteristic Curve for fine sand, m_2^w, at a particular suction is obtained by curve-fitting the corresponding SWCC assumed for fine sand (Figure 46) in this study.

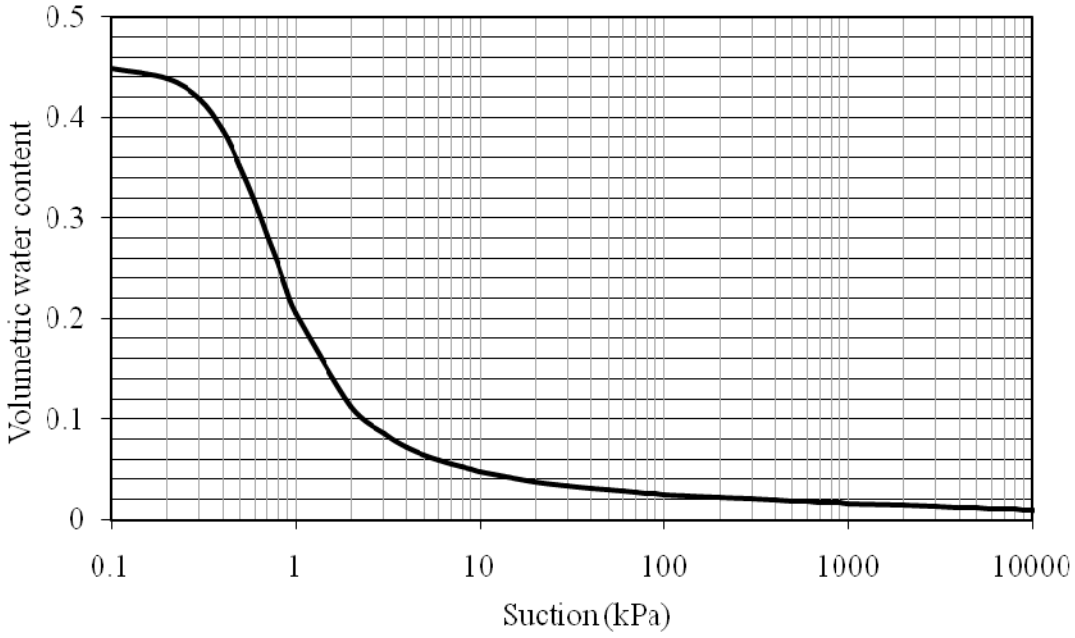

Figure 46: Soil Water Characteristic Curve for Fine Sand

Now, Eqn 64 and Eqn 65 can be written for two adjacent control volumes as shown in Eqn 68 and Eqn 69.

$$(\mathrm{Sn})_{i-1/2,j}\, u_{i-1/2,j}^{N+1} = (\mathrm{Sn})_{i-1/2,j}\, u_{i+1/2,j}^{N} + A_{i-1/2,j}^{N}(\Delta t) + \overline{A}_{i-1/2,j}^{N}(\Delta t)\left(\frac{p_{i,j}^{N} - p_{i-1,j}^{N}}{\Delta x}\right) + \overline{\overline{A}}_{i-1/2}^{N}(\Delta t) \qquad (68)$$

$$(\mathrm{Sn})_{i,j-1/2}\, v^{N+1}_{i,j-1/2} = (\mathrm{Sn})_{i,j-1/2}\, v^{N}_{i,j-1/2} + B^{N}_{i,j-1/2}(\Delta t) + \bar{B}^{N}_{i,j-1/2}(\Delta t)\left(\frac{p^{N}_{i,j} - p^{N}_{i,j-1}}{\Delta y}\right) +$$

$$\bar{\bar{B}}^{N}_{i,j-1/2}(\Delta t) + (\mathrm{Sn})_{i,j-1/2}\, g_y(\Delta t) \tag{69}$$

By substituting the Eqns 64, 65, 68, 69, 67a and 67b into Eqn 66 and rearranging the terms results in Eqn 70 and Eqn 71 for saturated zone and partly saturated zone respectively.

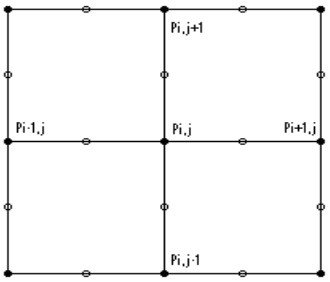

Figure 47: Neighborhood Points Used in the Iterative Procedure

For the saturated zone:

$$a_{i,j}\, p_{i,j} + b_{i,j}\, p_{i+1,j} + c_{i,j} p_{i-1,j} + d_{i,j}\, p_{i,j+1} + e_{i,j}\, p_{i,j-1} + T_{i,j} = 0 \tag{70a}$$

Where,

$$a_{i,j} = \left[\left(\frac{n_{i+1/2,j} + n_{i-1/2,j}}{\Delta x^2}\right) + \left(\frac{n_{i,j+1/2} + n_{i,j-1/2}}{\Delta y^2}\right)\right]\frac{\Delta t^2}{\rho} - 0.4343\, C_c \frac{(1 - n_{i,j})^2}{\sigma_{i,j} - p^{N}_{i.j}} \tag{70b}$$

$$b_{i,j} = -\left(\frac{n_{i+1/2,j}}{\Delta x^2}\right)\frac{\Delta t^2}{\rho} \tag{70c}$$

$$c_{i,j} = -\left(\frac{n_{i-1/2,j}}{\Delta x^2}\right)\frac{\Delta t^2}{\rho} \tag{70d}$$

$$d_{i,j} = -\left(\frac{n_{i,j+1/2}}{\Delta y^2}\right)\frac{\Delta t^2}{\rho} \tag{70e}$$

$$e_{i,j} = -\left(\frac{n_{i,j-1/2}}{\Delta y^2}\right)\frac{\Delta t^2}{\rho} \tag{70f}$$

and

$$T_{i,j} = \left(A^N_{i+1/2,j} - A^N_{i-1/2,j}\right)\frac{\Delta t^2}{\Delta x} + \left(\overline{\overline{A}}^N_{i+1/2,j} - \overline{\overline{A}}^N_{i-1/2,j}\right)\frac{\Delta t^2}{\Delta x} + \left(B^N_{i,j+1/2} - B^N_{i,j-1/2}\right)\frac{\Delta t^2}{\Delta y}$$
$$+ \left(\overline{\overline{B}}^N_{i,j+1/2} - \overline{\overline{B}}^N_{i,j-1/2}\right)\frac{\Delta t^2}{\Delta y} + \frac{\left(n_{i+1/2.j} \times u^N_{i+1/2,j} - n_{i-1/2.j} \times u^N_{i-1/2,j}\right)}{\Delta x}\Delta t +$$
$$\frac{\left(n_{i.j+1/2} \times v^N_{i,j+1/2} - n_{i.j-1/2} \times v^N_{i,j-1/2}\right)}{\Delta y}\Delta t + \frac{0.4343\, C_c\left(1-n_{i,j}\right)^2}{\sigma_{i,j} - p^N_{i,j}}\, p^{N-1}_{i,j}$$
$$+ \left(n_{i,j+1/2} - n_{i,j-1/2}\right) g_y \frac{\Delta t^2}{\Delta y} \tag{70g}$$

For the partly saturated zone:

$$a'_{i,j}\, p_{i,j} + b'_{i,j}\, p_{i+1,j} + c'_{i,j}\, p_{i-1,j} + d'_{i,j}\, p_{i,j+1} + e'_{i,j}\, p_{i,j-1} + T'_{i,j} = 0 \tag{71a}$$

Where,

$$a'_{i,j} = \left[\left(\frac{(Sn)_{i+1/2,j} + (Sn)_{i-1/2,j}}{\Delta x^2}\right) + \left(\frac{(Sn)_{i,j+1/2} + (Sn)_{i,j-1/2}}{\Delta y^2}\right)\right]\frac{\Delta t^2}{\rho} - \left(m_2^w\right)_{i,j} \tag{71b}$$

$$b'_{i,j} = -\left(\frac{(Sn)_{i+1/2,j}}{\Delta x^2} \right) \frac{\Delta t^2}{\rho} \tag{71c}$$

$$c'_{i,j} = -\left(\frac{(Sn)_{i-1/2,j}}{\Delta x^2} \right) \frac{\Delta t^2}{\rho} \tag{71d}$$

$$d'_{i,j} = -\left(\frac{(Sn)_{i,j+1/2}}{\Delta y^2} \right) \frac{\Delta t^2}{\rho} \tag{71e}$$

$$e'_{i,j} = -\left(\frac{(Sn)_{i,j-1/2}}{\Delta y^2} \right) \frac{\Delta t^2}{\rho} \tag{71f}$$

and

$$T'_{i,j} = \left(A^N_{i+1/2,j} - A^N_{i-1/2,j} \right) \frac{\Delta t^2}{\Delta x} + \left(\overline{\overline{A}}^{=N}_{i+1/2,j} - \overline{\overline{A}}^{=N}_{i-1/2,j} \right) \frac{\Delta t^2}{\Delta x} + \left(B^N_{i,j+1/2} - B^N_{i,j-1/2} \right) \frac{\Delta t^2}{\Delta y} +$$
$$\left(\overline{\overline{B}}^{=N}_{i,j+1/2} - \overline{\overline{B}}^{=N}_{i,j-1/2} \right) \frac{\Delta t^2}{\Delta y} + \frac{\left((Sn)_{i+1/2,j} \times u^N_{i+1/2,j} - (Sn)_{i-1/2,j} \times u^N_{i-1/2,j} \right)}{\Delta x} \Delta t +$$
$$\frac{\left((Sn)_{i,j+1/2} \times v^N_{i,j+1/2} - (Sn)_{i,j-1/2} \times v^N_{i,j-1/2} \right)}{\Delta y} \Delta t + \left((m_2^w)_{i,j} \right) p^{N-1}_{i,j} + \left((Sn)_{i,j+1/2} - (Sn)_{i,j-1/2} \right) g_y \frac{\Delta t^2}{\Delta y} \tag{71g}$$

4.9 Numerical Application of the Model

4.9.1 Modeling Confined Flow through a Partly Saturated Fine Sand Layer (Case I)

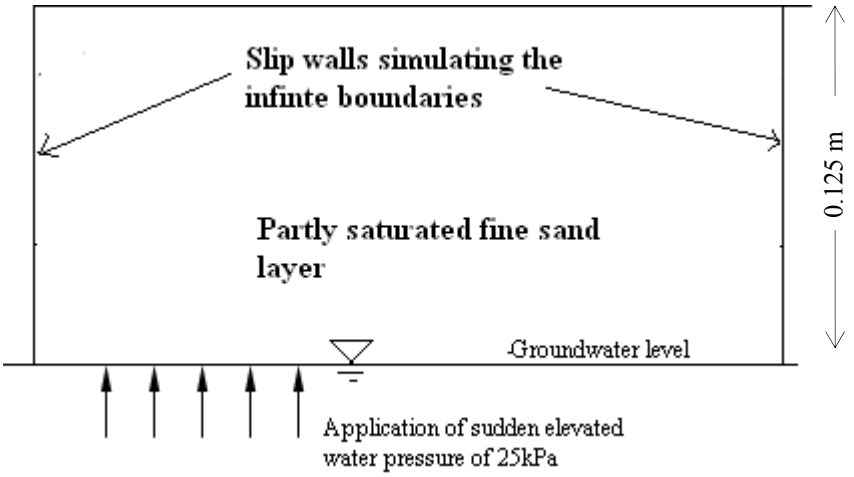

Figure 48: Illustration of the Flow through the Unsaturated Fine Sand Layer

The fine sand layer (Figure 48) was divided into a 50 × 50 grid for the finite difference analysis. One fluid cell, known herein as a grid element, was selected to be 2.5 mm × 2.5 mm × 1m. A unit width has been selected in the third direction assuming two dimensional water flow. First, natural porosities (void ratios) were assigned to each grid element based on the spatial probability distribution of natural void ratios determined from packing (Section 4.4). Within each grid element, the fluid-particle interaction is quantified considering the averaged particle diameter which is defined as the arithmetic mean of the diameters of all the particles in that grid.

4.9.2 Boundary Conditions

The boundary conditions appropriate for the water flow through the single soil layer are specified in the computer code as indicated in Figure 49.

1) At the inflow boundary, the pressure and velocities are specified.
2) At the outflow boundary, the pressure is specified and velocity components are allowed to float.
3) At the vertical walls, the slip conditions are maintained. Thus, the velocity component, u, normal to the walls is set to zero.

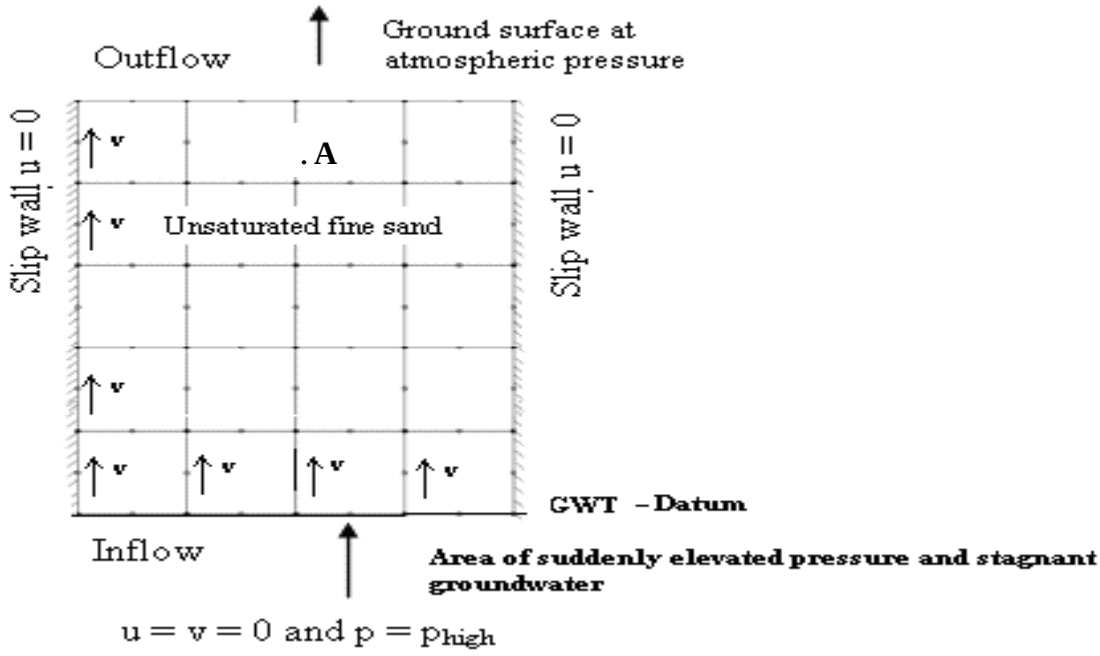

Figure 49: Boundary Conditions Incorporated in the Flow through Saturated - Unsaturated Soil Layer

4.9.3 Results

Upon the application of the elevated water pressure that causes a sudden hydraulic gradient across the pavement layer in Figure 50, the variation of water porosity (volumetric water content) with water pressure is illustrated in Figure 50. Figure 50 also shows that suction within the soil mass is gradually converted to a positive pressure under the application of elevated pressure at the bottom of the soil layer. The corresponding variations of degree of saturation are shown in Figure 51.

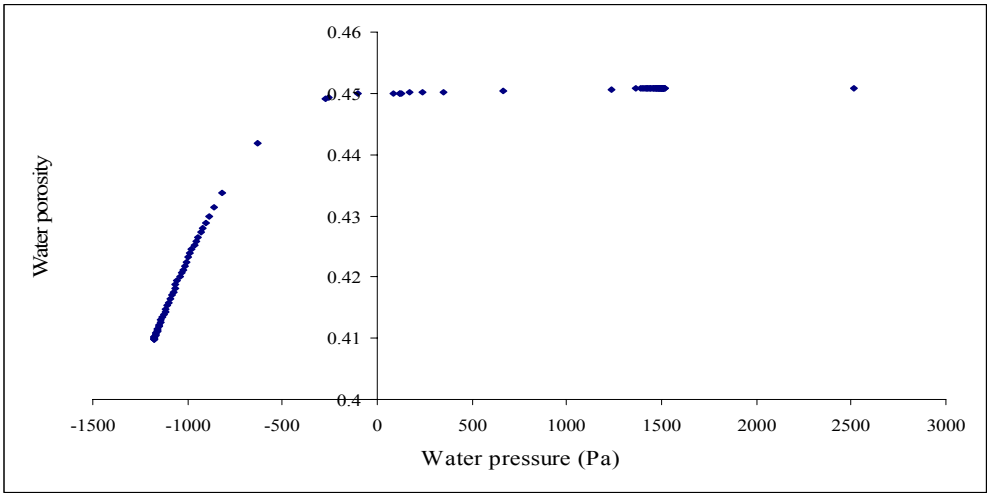

Figure 50: The Variation of Water Porosity with Water Pressure at a Point within the Unsaturated Zone (At Point A in Figure 49)

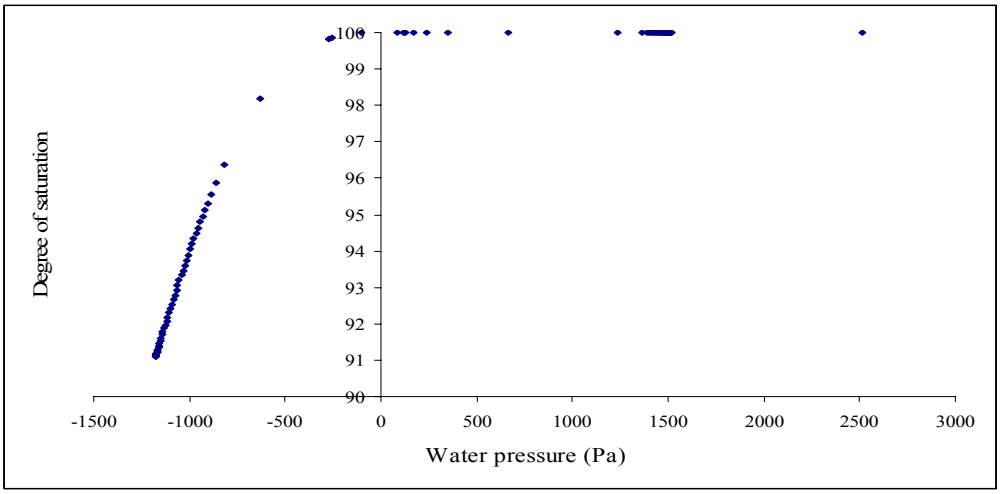

Figure 51: The Variation of the Degree of Saturation with Water Pressure (At Point A in Figure 49)

Figures 52a -52c show how the partly saturated zone gradually becomes fully saturated due to the upward water seepage. From Figure 53, it is seen that it takes approximately 50 time steps (5×10^{-3} seconds) for complete saturation of the layer and 80 time steps (8×10^{-3} seconds) to reach the steady state flow through the fully saturated zone.

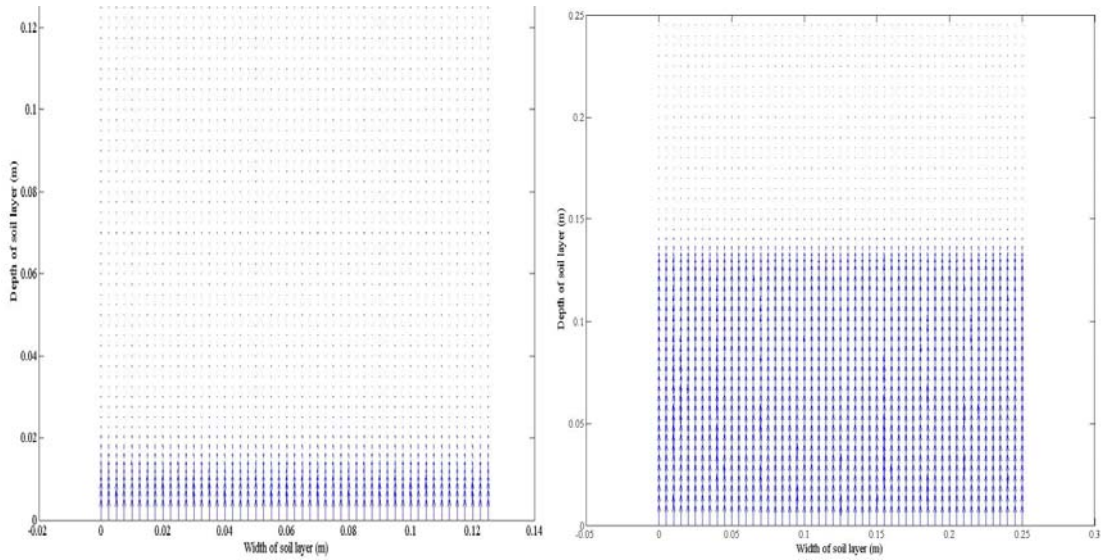

(a) t = 1

(b) t = 25

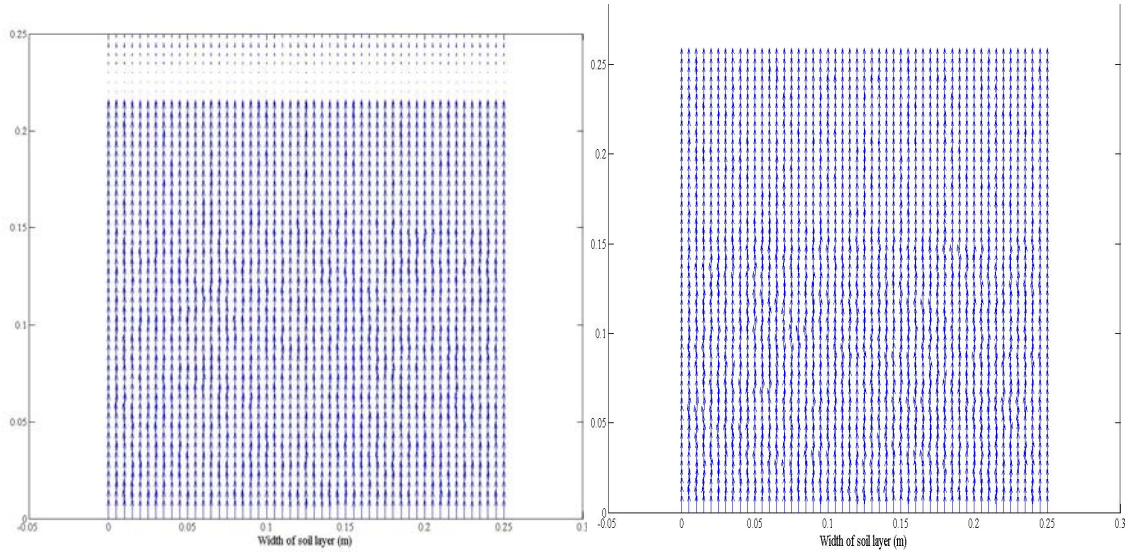

(c) t = 50

(d) t = 100

Figure 52: Velocity Vector Plots for Flow through Saturated and Partly-Saturated Soil Layer

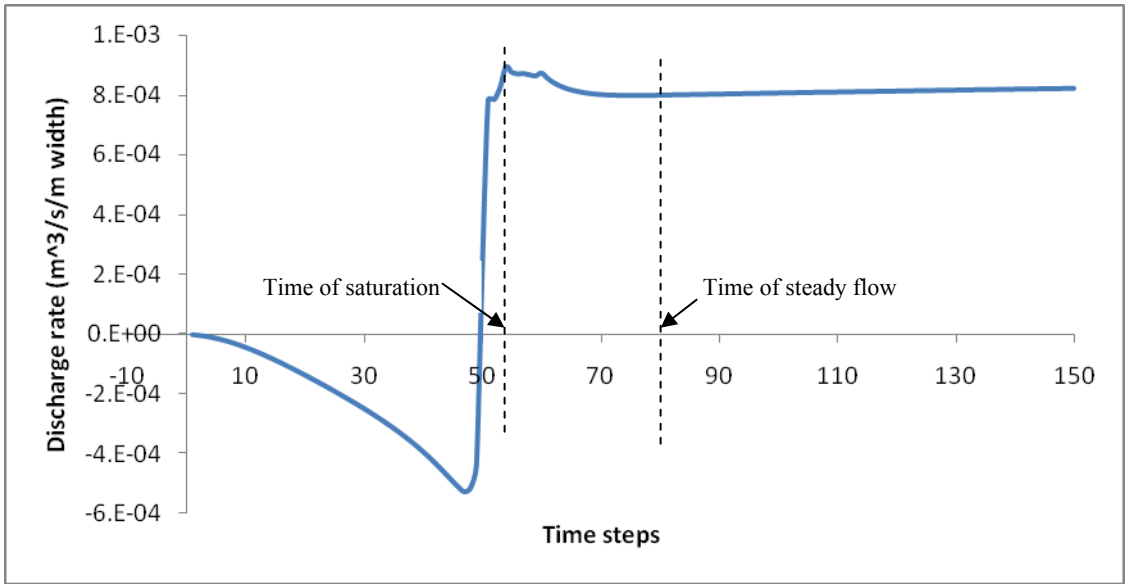

Figure 53: Variation of Discharge Flow Rate with Time Step

4.10 Conclusions

The results show that

1) The partly saturated zone having capillary pressures (suction) gradually becomes fully saturated due to seepage caused by an elevated water pressure at the bottom of the fine sand layer.
2) It takes the fine sand layer almost 80 time steps (8×10^{-3} seconds) to become fully saturated.
3) The water porosity Vs suction plot and the degree of saturation Vs suction plot show good agreement with the corresponding characteristics plots for fine sand.

Based on the above it can be concluded that model is applicable to partly saturated soils as well.

CHAPTER FIVE

MODELING UNCONFINED FLOW AROUND A RETENTION POND

5.1 Introduction

Retention ponds are man-made or natural depressions into which stormwater runoff is directed for temporary storage [Figure 54] with the expectation of disposal by infiltration into a shallow groundwater aquifer. They are often created near areas of development and in many instances required with new development of buildings, parking lots, roads, etc by the permitting agencies. Retention ponds are developed primarily to serve two functions such as limit flooding and the removal of pollutants.

Figure 54: Typical Retention Pond

5.2 Existing Design of Retention Pond

The required size of a retention pond depends on the rate of inflow to the pond and the total quantity of flow as well as the rate of infiltration during a storm event, given the antecedent conditions of the receiving aquifer. In order to avoid the overflow or flooding, the retention volume recovery time should be adequate to completely dissipate the retained stormwater from the pond after the design storm event. The retention volume recovery time is defined as the time it takes to infiltrate the retention volume. This depends on subsurface soil conditions and the input due to surface runoff.

In the conventional models that are used to design retention ponds, the soil skeleton is treated as a continuum and the dynamic flow of water through soil pores is commonly idealized using the Darcy's law. MODFLOW [24] is a U.S. Geological Survey's modular finite-difference saturated flow model, which is currently the most widely used numerical model in the U.S. Geological Survey (USGS) for analyzing groundwater flow problems. The above program is used by hydrogeologists to simulate the flow of groundwater through aquifers. In MODFLOW, a groundwater flow equation derived from Darcy's law is solved using the finite-difference approximation. The partial differential equation of groundwater flow used in MODFLOW is

$$\frac{\partial}{\partial x}\left(K_x \frac{\partial h}{\partial x}\right) + \frac{\partial}{\partial y}\left(K_y \frac{\partial h}{\partial y}\right) + \frac{\partial}{\partial z}\left(K_z \frac{\partial h}{\partial z}\right) + W = S_s \frac{\partial h}{\partial t} \quad (72)$$

Where, K_x, K_y and K_z are values of hydraulic conductivity along x, y and z coordinate axes respectively; h is the hydraulic head; W is a volumetric flux per unit volume representing sources and/or sinks of water (W < zero for flow out of the groundwater

system and W > zero for flow in) and S_s is the specific storage of the soil. Eqn 72, when combined with boundary and initial conditions, describes transient three-dimensional groundwater flow in a heterogeneous and anisotropic medium.

MODRET (Computer **MOD**EL to Design **RET**ENTION Ponds) is an interactive computer program that can be used to calculate the unsaturated and saturated infiltration losses from stormwater retention ponds into unconfined aquifers using a modified version of MODFLOW. MODRET was originally developed in 1990 as a complement to a research and development project for South West Florida Water Management District (SWFWMD). The Infiltration Module of the MODRET program uses a modified Green and Ampt infiltration equation [25] to calculate the unsaturated infiltration and a modified USGS's model [24] to calculate the saturated infiltration. The Green and Ampt infiltration equation [25] was originally presented as an empirical description for unsaturated infiltration analysis; later, its empirical constants were theoretically investigated [26]. For all above analysis, the coefficients of hydraulic conductivities determined from the field tests or laboratory experiments are used in determining the infiltration losses through retention ponds. But, instead of using the a single value of coefficient of hydraulic conductivity for entire flow domain on a continuum basis, the current particulate model uses spatially localized coefficients of hydraulic conductivities in terms of drag forces between solid particles and pore fluid which are instantaneously determined from the average particle diameters and the localized porosities.

5.3 Modeling of Soil Structure (3D Random Packing of Soil Particles)

The particle size distribution curve shown in Figure 55 was selected to model the retention pond. The soil particles are assumed to be of spherical shape and to determine the natural void ratio for coarse sand shown in Figure 55, a customized random packing algorithm was developed. In the case of coarse sand, 16 mm × 16 mm × 16 mm cubes were packed. It must be noted that the PSD in Figure 55 is cumulative probability distribution of particle size for coarse sand. Therefore, by using an adequately large array of random numbers from a uniform distribution between 0 and 100 (the y axis range in Figure 55), one can select the corresponding array of particle diameters that conforms to a selected PSD, from the x axis. This technique, known as the Monte-Carlo simulation [14] is used to select the array of packing diameters for each cube. It is noted that the resulting natural void ratio distribution change in each packing trial since the order of diameters used for packing is changed randomly. The detailed packing procedure can be found in [27]. A thousand of such cubes were randomly packed in order to model the half of the retention pond defined by mesh of 100 by 150. The asymmetry of the retention pond caused by the nature of random packing is neglected in this study.

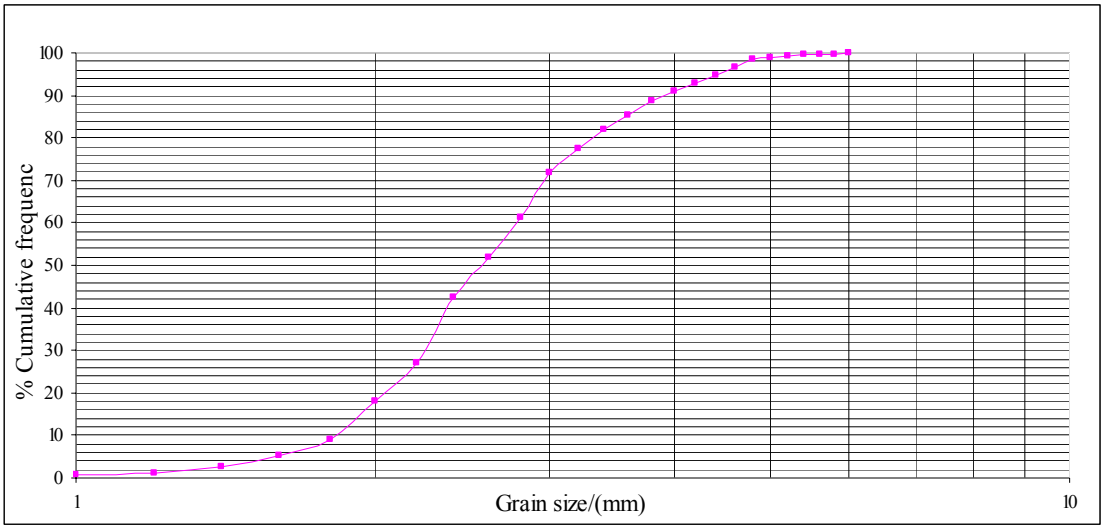

Figure 55: Particle Size Distributions for Coarse Sand

5.4 Numerical Procedure for Determination of the Free-Surface

Determination of the free-surface is required in the analysis of unconfined seepage problems such as flow through earthen dams and retention ponds. One commonly used approach to determine the free-surface is the graphical approach based on Dupuit's theory [1]. In addition, there are numerical techniques proposed by various researchers in the literature [28 – 32]. In this study, a modified technique resembling the extended pressure (EP) method first proposed by Brezis et al. [33] is employed with Navier Stokes equations in order to determine the free-surface for flow around a retention pond.

The dry zone and wet zone around the retention pond are defined using the fundamentals of streamlines, i.e., the locus of the path of flow of an individual particle of water and continuity of flow quantity through a cross section. Along any flow line, the path of

water passing through point P(x_1, y_1) can be expressed (Figure 56) in mathematical form as

$$\frac{dy}{dx} = \frac{v_1}{u_1} \tag{73}$$

Hence knowing one point, P(x_1, y_1) on the free-surface, the next point, Q (x_2, y_2) along the free-surface can be obtained using Eqn 74.

$$(x_2 - x_1) = \left(\frac{u_1}{v_1}\right)_P (y_2 - y_1) \tag{74a}$$

$$x_2 = x_1 + \left(\frac{u_1}{v_1}\right)_P \Delta y \tag{74b}$$

In generalized form,

$$x_{j+1} = x_j + \left(\frac{u_1}{v_1}\right)_j \Delta y \tag{74c}$$

Once, the extreme boundary point, Q, is determined along the free-surface, the dry zone is identified using a Heaviside step function in Section 5.5.

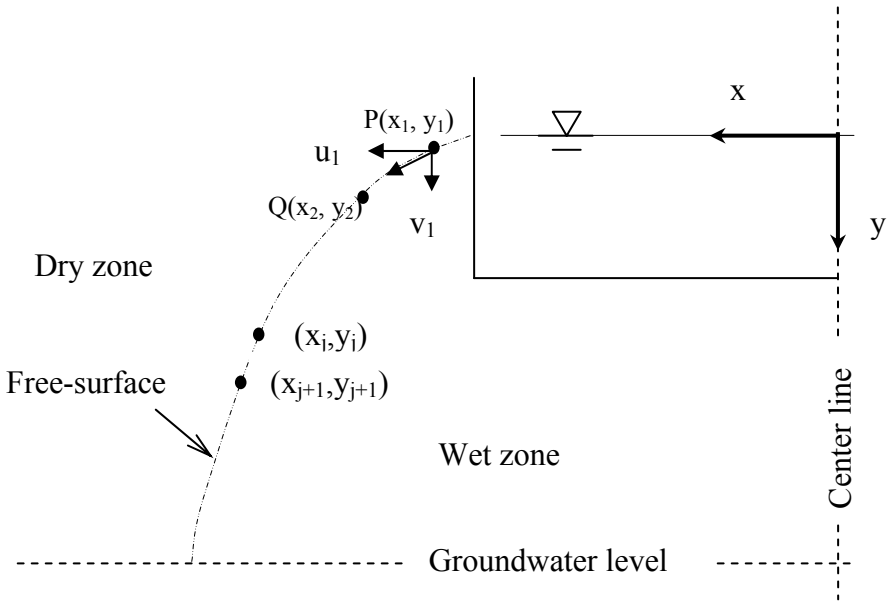

Figure 56: Determination of Dry and Wet Zones around the Retention Pond

5.4.1 Navier Stokes Equations

In the current formulation, water seepage is analyzed using Navier Stokes equations written in terms of water pressures and velocities. Hence, the authors use a Heaviside step function with water pressures and velocities in order to identify the dry and wet zones in conjunction with Navier Stokes equations. For this work, the Heaviside-step function (Eqn 75) is expressed in terms of the coordinates of the extreme boundary point on the free-surface at any horizontal level (x_j) as follows:

$$H(x) = \begin{cases} 0 & \text{, if } x \geq x_j \\ 1 & \text{, if } x < x_j \end{cases} \qquad (75)$$

To achieve this objective, Navier Stokes equations are written incorporating the Heaviside step function as follows:

Mass Conservation (Continuity Equation):

$$\frac{\partial(nHu)}{\partial x}+\frac{\partial(nHv)}{\partial y} = -\frac{\partial n}{\partial t} \tag{76}$$

Momentum Conservation (Momentum Equations):

X direction:

$$\frac{\partial(nHu)}{\partial t}+\frac{\partial(nHu^2)}{\partial x}+\frac{\partial(nHuv)}{\partial y}-\frac{\mu}{\rho}\left(\frac{\partial^2 nHu}{\partial x^2}+\frac{\partial^2 nHu}{\partial y^2}\right)-\frac{HD_x}{\rho}=-\frac{Hn}{\rho}\frac{\partial p}{\partial x} \tag{77}$$

Y direction:

$$\frac{\partial(nHv)}{\partial t}+\frac{\partial(nHuv)}{\partial x}+\frac{\partial(nHv^2)}{\partial y}-\frac{\mu}{\rho}\left(\frac{\partial^2 nHv}{\partial x^2}+\frac{\partial^2 nHv}{\partial y^2}\right)-\frac{HD_y}{\rho}=-\frac{Hn}{\rho}\frac{\partial p}{\partial y}+ng_y \tag{78}$$

It is seen that Eqns 76 – 78 are inactivated in the dry zone ($i \geq i^*$). This can be assured by using the Heaviside-step function in Eqns 75. Now, Eqns 76-78 can be applied both in the wet and dry zones.

5.4.2 Boundary Conditions

The boundary conditions appropriate for the actual water flow around the retention pond are specified in the computer code as indicated in Figure 57.

1) Hydrostatic pressure distribution ($h\gamma_w$) is specified along the retention pond walls based on the water level in the pond (h).
2) Along the walls of the retention pond, non-slip velocity boundary conditions are specified as shown in Figure 57.

3) At the exterior vertical wall boundaries within the two-phase media, the slip conditions are maintained. Thus, the velocity component, u, normal to the walls is set to zero.

4) At the groundwater table, water pressure is set to zero; water velocities allow floating.

5) As an initial condition, the completely filled retention pond is considered.

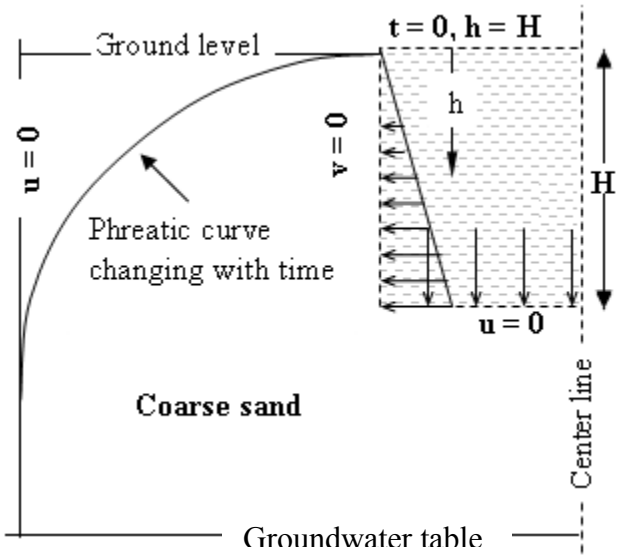

Figure 57: Boundary and Initial Conditions Incorporated in the Flow around the Retention Pond

5.5 Determination of Free-Surface from Dupuit's Theory

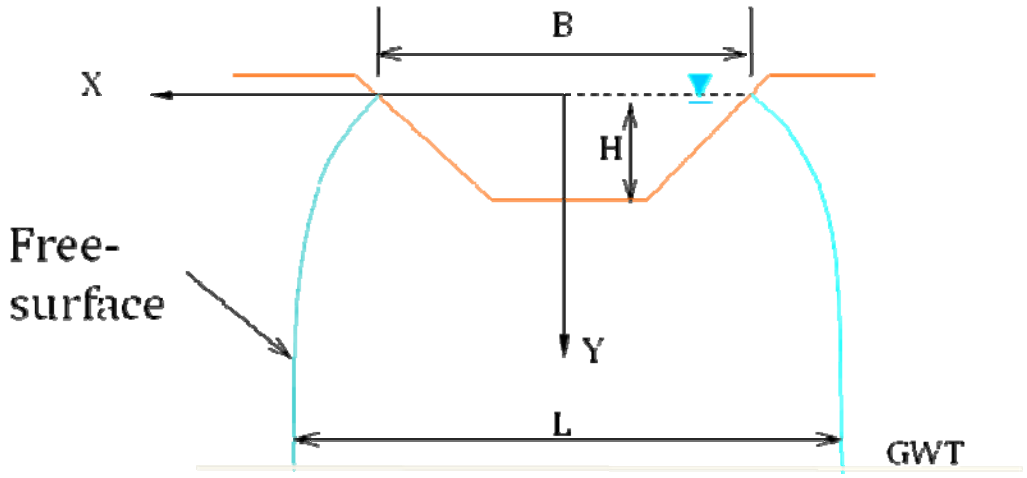

Figure 58: Analytical Method to Determine the Free-Surface

Using the configuration of the retention pond irrespective of soil properties, the free-surface is analytically determined using Eqn 79.

$$\pm x = \left(\frac{B-L}{2}\right) e^{-\pi y/L} + \frac{L}{2} \tag{79a}$$

$$L = B + 2H \tag{79b}$$

5.6 Results on Free-Surface

The free-surfaces around the retention pond obtained using the numerical procedure and Dupuit's theory are compared as shown in Figure 58. There are discrepancies which can be due to the fact that the Dupuit's theory does not take into account the hydraulic conductivities around the retention pond whereas the numerical procedure incorporates

the localized variations of hydraulic conductivities. Therefore, the free-surface determined from the numerical method is more accurate than that of Dupuit's theory. Moreover, it is seen from Figure 59, that the influence zone covered by the free-surface is getting wider as time increases.

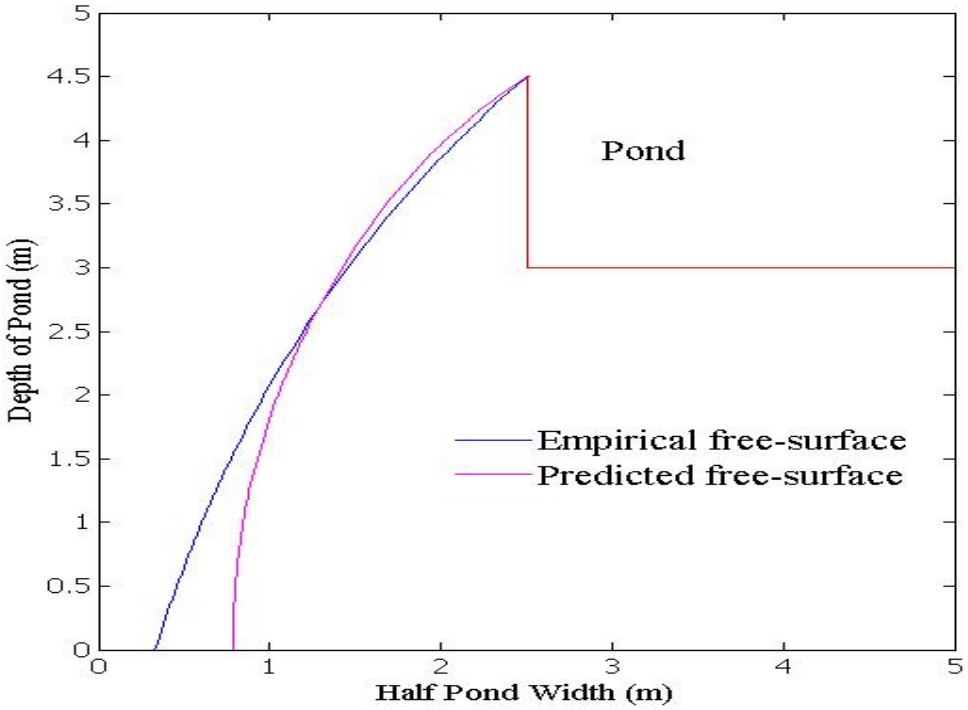

Figure 59: Comparison of Free-Surface around the Retention Pond

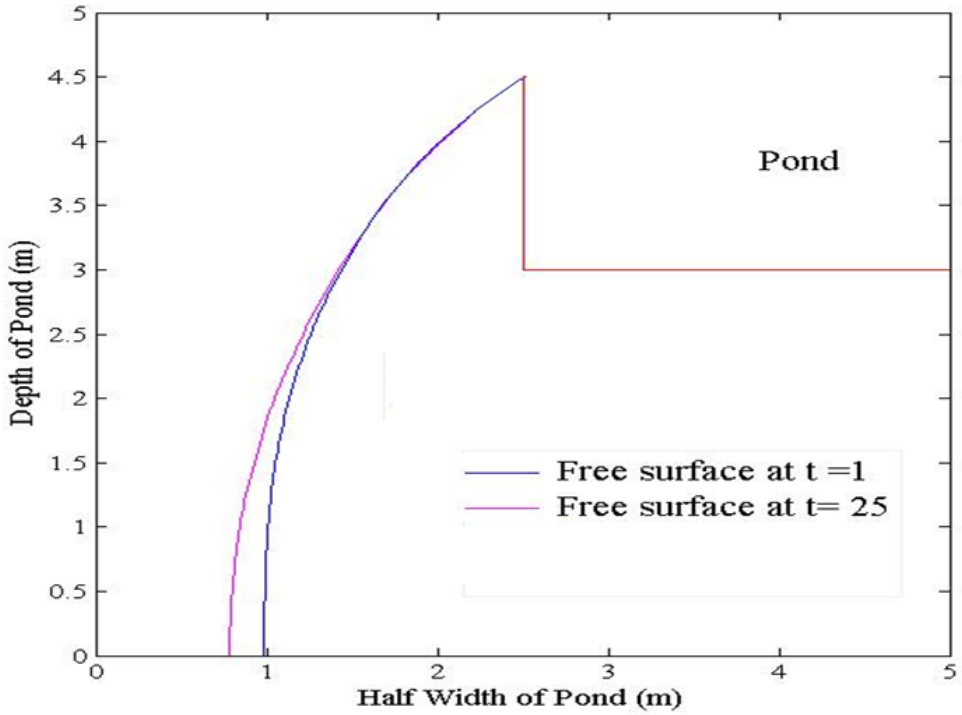

Figure 60: Location of Free-Surface around the Retention Pond with Time

5.7 Prediction of Recovery Time

Recovery time is defined as a length of time required for the design treatment volume in a pond to subside to the normal level or bottom of the pond. Three-dimensional Finite Difference Groundwater Flow Model (MODFLOW) developed by U.S. Geological Survey [24] for saturated groundwater flow modeling is used to compare the recovery time predicted using the model developed in this study. A schematic of an unconfined aquifer is shown in Figure 60 with the notations used in the equations. The aquifer is assumed to be homogeneous and isotropic, and it is underlain by an impervious horizontal layer.

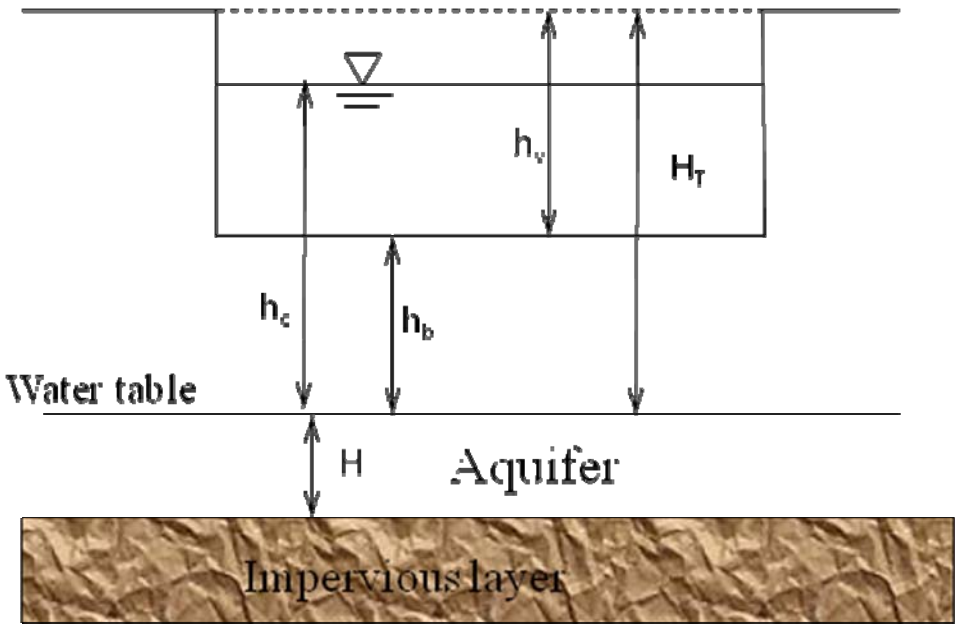

Figure 61: Saturated Infiltration Analysis using MODFLOW

Dimensionless parameters, F_x and F_y are defined in terms of

1) Hydraulic parameters of the aquifer
2) Recharge rate and duration,
3) The physical configuration of the pond and the desired time period.

$$F_x = \left(\frac{W^2}{4 K_H D t} \right)^{1/2} \tag{80a}$$

$$F_y = \frac{h_c}{H_T} \tag{80b}$$

$$H_T = h_b + h_v \tag{80c}$$

Where, h_c - Height of water level in the retention pond above the initial groundwater table, h_b - Height of the pond bottom above the groundwater table, h_v - Maximum height

of water level in pond, W - Average width of the pond, K_H - Average horizontal hydraulic conductivity of the aquifer, D - Average saturated thickness of the aquifer (= H + h_c/2), H - Initial saturated thickness of aquifer, f - Effective porosity and t - Recovery time.

A family of dimensionless curves similar to Figure 63 is plotted by USGS for different effective porosity of soil. According to Eqn 80, the estimated recovery time for the selected pond is 4.7 days whereas the numerical model predicts that of 4 days from the Figure 62.

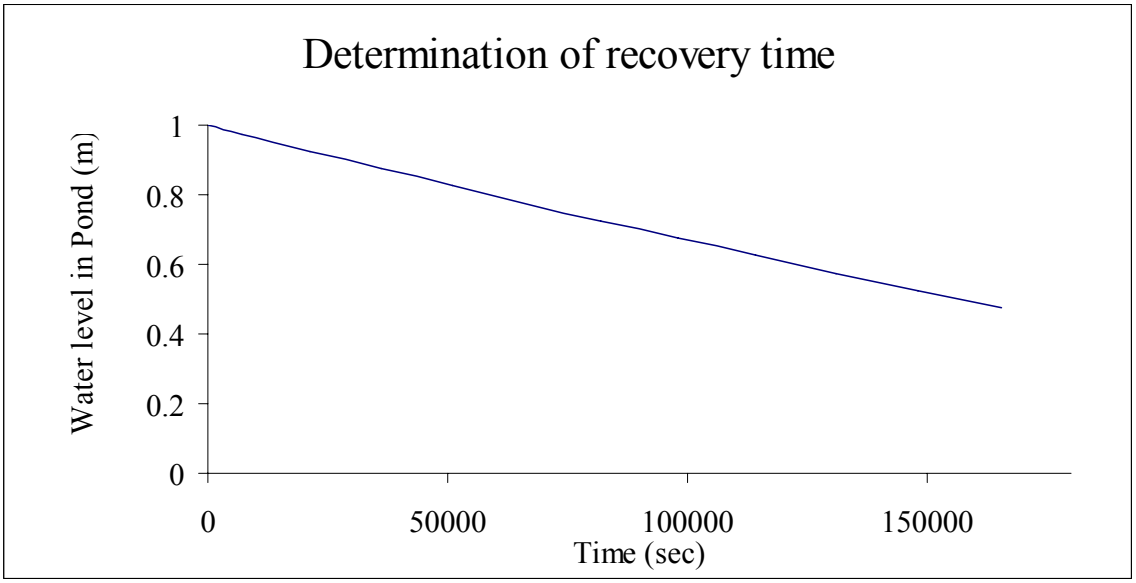

Figure 62: Prediction of Recovery Time from Numerical Model

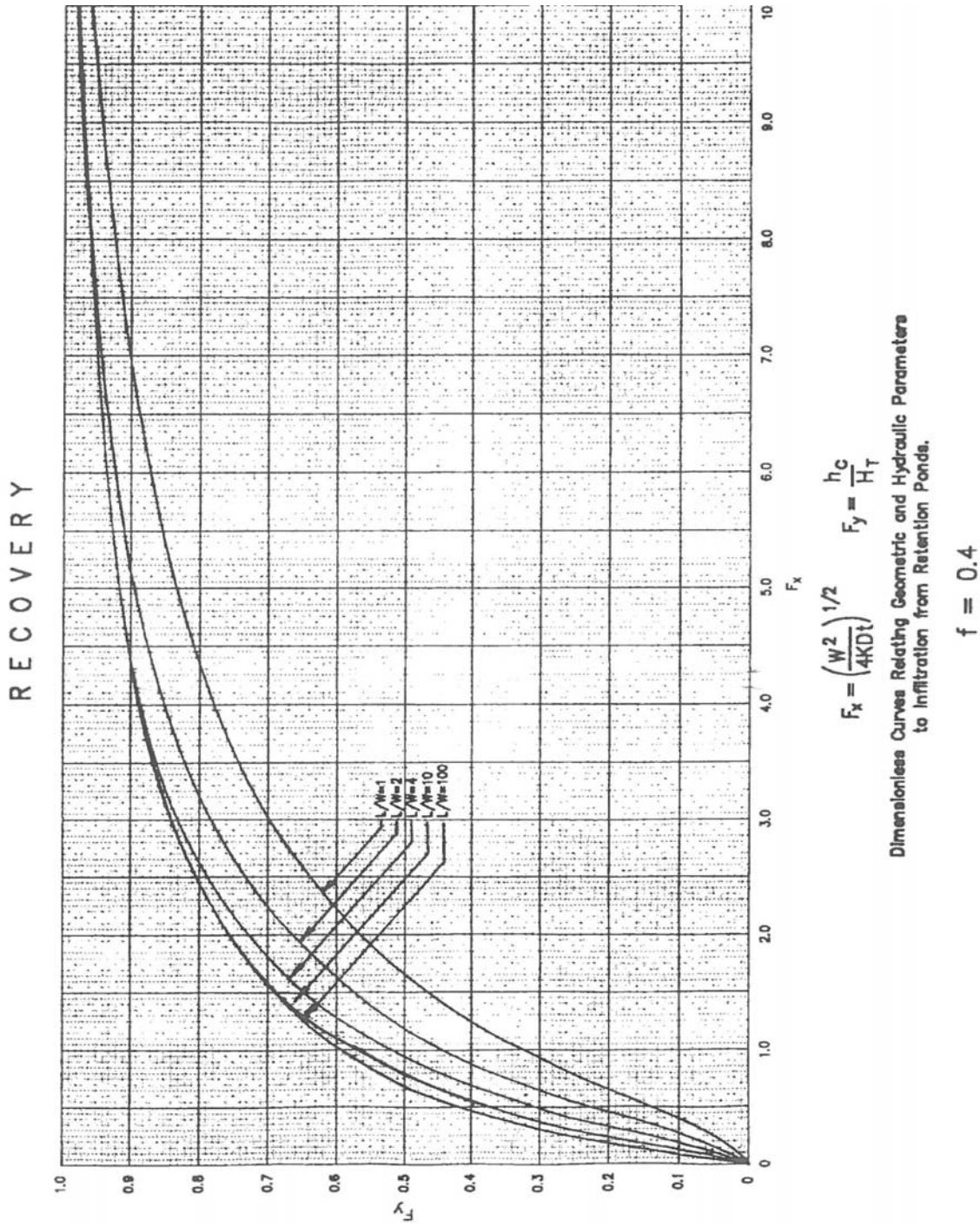

Figure 63: Sample Plot to Determine Recovery Time from MODFLOW

5.8 Conclusions

The application of the model developed in the first phase of the study has been extended to predict the recovery time for the retention pond including the location of the free-surface. The recovery time obtained from the developed model agrees with that of the MODFLOW analysis. Furthermore, the free-surface around the retention determined from the numerical model shows good agreement with that predicted by the Dupuit's theory.

REFERENCES

1. Harr ME. Groundwater and seepage. Dover publications: New York, 1991.

2. Fredlund DG. Second symposium and short course on unsaturated soils and environmental Geotechnics. University of Saskatchewan, Canada, 2003.

3. Ng CWW. and Shi Q. A Numerical Investigation of the Stability of unsaturated soil slopes subjected to transient seepage. Computers and Geotechnics 1998; 22(1):1-18.

4. El Shamy U, Zeghal M, Shephard M, Dobry R, Fish J, and Abdoun T. Discrete element simulations of water flow through granular soils. 15th ASCE Engineering Mechanics Conference, 2002.

5. El Shamy U., and Zeghal M. Coupled Continuum-Discrete model for saturated granular soils, Journal of Engineering Mechanics, April 2005.

6. Shimizu Y. Fluid coupling in PFC2D and PFC 3D, Manual, Itasca Consulting Group, Numerical Modeling in Micromechanics via Particle Methods, 2004.

7. Itasca. *Particle Flow Code, PFC3D, release 3.0*. Itasca Consulting Group, Inc., Minneapolis, Minnesota, 2003.

8. Anderson TB and Jackson R. A Fluid Mechanical Description of Fluidized Beds, Industrial Engineering Chemical Fundamentals, 1967; 6(4): 527-539.

9. Tsuji Y., Kawaguchi T., and Tanaka T., Discrete particles simulation of 2-dimensional fluidized bed. Powder Technology, 1993; 77: 79-87.

10. Cundall PA and Strack ODL. A Discrete Numerical Model for Granular Assemblies, Geotechnique 1979; 1: 47-65.

11. Patankar S. Numerical Heat Transfer and Fluid Flow: Taylor and Francis, London. 1980.

12. Engineer Manual No. 1110-2-1901, Department of the Army, U.S. Army Corps of Engineers, Washington, DC, April, 1993.

13. Anderson J. Computational Fluid Dynamics- the Basics with applications, McGraw Hill, Inc. 1995.

14. Harr ME. Mechanics of Particulate Media. A Probabilistic Approach: New York, McGraw Hill, 1977.

15. Bowles JE. Physical and Geotechnical Properties of Soils, McGraw Hill, Inc.1984.

16. Das BM. Principles of Geotechnical Engineering: Brooks/Cole Thomson learning, sixth edition, 2006.

17. Jeyisanker, K. and Gunaratne, M, Analysis of Steady State Water Seepage in a Particulate Pavement System**,** under review by Transportation Research Board, 2008.

18. Pestana JM, Whittle AJ. and Salvati LA. Evaluation of a constitutive model for clays and sands: Part 1 – Sand behavior, International Journal for Numerical and Analytical Methods in Geomechanics 2002; 26:1097-1121.

19. Fredlund DG, and Xing A., Equations for the Soil-Water Characteristic Curve. Canadian Geotechnical Journal, 31; 3:521-532.

20. Lu.N, Likos WJ, Unsaturated Soil Mechanics, Wiley Publishers, May, 2004.

21. Fredlund DG., and Morgenstern NR., Stress State Variables for Unsaturated Soils, Journal of the Geotechnical Engineering Division, American Society of Civil Engineers, 103;GT5: 447-466.

22. Lam.L, Fredlund, DG., and Barbour.SL., Transient Seepage Model for Saturated-Unsaturated Soil Systems: A Geotechnical Engineering Approach, Canadian Geotechnical Journal, 1987; 24: 565-580.

23. Clifton AW, Barbour SL, and Wilson GW. The Emergence of Unsaturated Soil Mechanics, Fredlund Volume, NRC Research Press, Ottawa, 1999.

24. Harbaugh, A.W., and M.G. McDonald. 1996. *User's documentation update to the U.S. Geological Survey modular finite-difference* U.S. Geological Survey Open-File Report 96-485, 56p.

25. Green, W. H., and Ampt, G. A. “Studies on soil physics. 1. The flow of air and water through soils.” J. Agric. Sci., 1911, 4(1), 1–24.

26. Bouwer, H., Infiltration of Water into Non-uniform soil, Journal of the Irrigation and Drainage Division, ASCE, 1969, No. IR4, 451-462.

27. Jeyisanker, K. and Gunaratne, M. Analysis of Water Seepage in a Pavement System Using the Particulate Approach, accepted for the publication, Computers and Geotechnics, 2008.

28. Taylor RL, Brown CB, Darcy flow solutions with a free surface, Journal of Hydraulic Division, ASCE, 1967; 93: 25-33.

29. Bardet J.-P, Tobita T, A Practical Method for Solving Free-Surface Seepage Problems. Computers and Geotechnics, 2002; 29; 451-475.

30. Desai CS, Li GC A residual flow procedure and application for free surface flow in porous media. Advanced Water Resources 1983; 6; 27-35.

31. Alt HW, Numerical Solution of Steady State Porous Flow Free Boundary Problems. Numerical Mathematics 1980; 31: 73-98.

32. Kikuchi N. An Analysis of the variational Inequalities of Seepage Flow by Finite-Element Methods. Quartitative Applied Mathematics 1977; 35: 149-163.

33. Brezis H, Kinderlehrer D, Stampacchia G, Sur une nouvelle formulation du probleme de l'ecoulement a travers une digue, Serie A. paris: C.R.Academie des Sciences; 1978.

ABOUT THE AUTHOR

Kalyani Jeyisanker received her B.Sc. (Eng), with honors, in Civil Engineering from University of Peradeniya, Sri Lanka in 2001. She earned her Master's degree in Mechanical Engineering from Texas Tech University in 2004 and enrolled in PhD program in 2005 at University of South Florida. While pursuing the PhD, Ms. Jeyisanker actively participated in numerous research projects. She also coauthored two journal papers and two conference papers.